Modelling of acoustic viscothermal losses using the Boundary Element Method: From method to optimization

Andersen, Peter Risby

Publication date:
2018

Document Version
Publisher's PDF, also known as Version of record

Modelling of acoustic viscothermal losses using the Boundary Element Method

From method to optimization

PhD Thesis

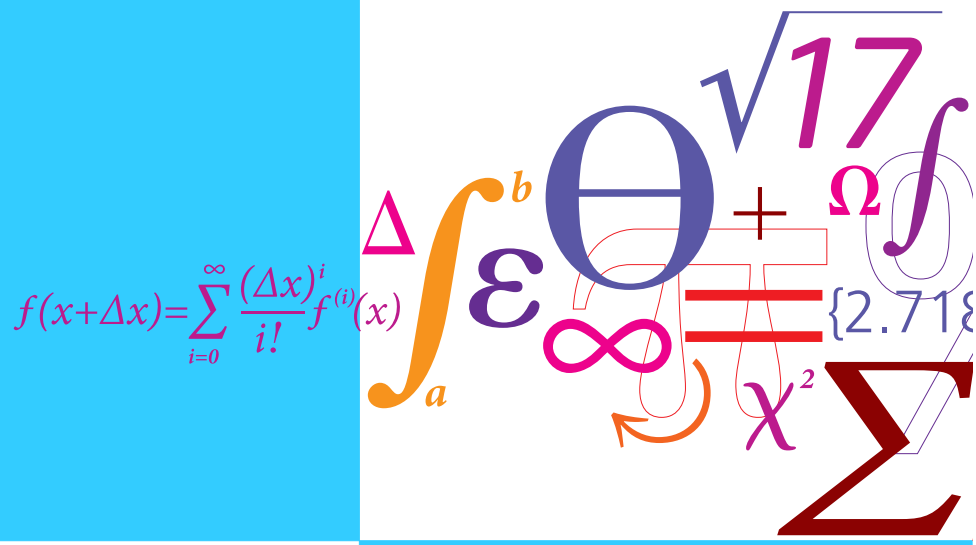

Peter Risby Andersen
Centre for Acoustic-Mechanical
Micro Systems (CAMM)
Acoustic Technology
October 2018

DTU Electrical Engineering
Department of Electrical Engineering

This thesis was submitted to the Technical University of Denmark as partial fulfillment of the requirements for the degree of Doctor of Philosophy (PhD). The studies was financed by the Centre for Acoustic-Mechanical Micro Systems (CAMM), and completed between October 1 2015 and September 30 2018 at the Department of Electrical Engineering and the Acoustic Technology group under the supervision of Associate Professor Vicente Cutanda Henríquez and Associate Professor Niels Aage.

Title

Modelling of acoustic viscothermal losses using the Boundary Element Method: From method to optimization

Author

Peter Risby Andersen

Supervisors

Assoc. Prof. Vicente Cutanda Henríquez
Assoc. Prof. Niels Aage

Acoustic Technology
Department of Electrical Engineering
Technical University of Denmark
Kgs. Lyngby, Denmark

Abstract

A range of acoustic engineering problems require the inclusion of viscous and thermal dissipation to be modelled accurately. The dissipative effects are especially relevant when the geometric dimensions of the acoustic domain become small which is the case in acoustic transducers and hearing aids. Computer-based numerical tools such as the Finite Element Method can be used to model and investigate the performance of acoustic devices without expensive prototyping. Directly including acoustic dissipation into the Finite Element Method comes at a significant computational cost, sometimes making simulations on modest hardware problematic. An interesting alternative to the Finite Element Method, is the Boundary Element Method that is capable of including dissipation and at the same time avoid so-called boundary layer meshing. However, a potential shortcoming of the existing boundary element implementation is its use of tangential derivative finite difference coupling terms, that may lead to undesirable inaccuracies.

This work presents two new coupling strategies that avoid the use of finite difference by either using boundary element itself or the shape functions to estimate the tangential derivatives. Numerical experiments demonstrate increased stability and error reduction when using the new coupling strategies.

Furthermore, based on the improved viscothermal Boundary Element Method, a gradient-based shape optimization technique is developed. The shape optimization technique is used to optimize the absorption coefficient of two-dimensional quarter-wave and Helmholtz resonators located at an impedance tube termination. Shape optimization results show that high absorption coefficients are only obtained when viscous and thermal dissipation is modelled accurately. The shape optimization technique has the future potential of improving the design of acoustic devices which require the inclusion of viscous and thermal dissipation.

Resumé

En række ingeniørmæssige akustiske problemstillinger kræver præcis modellering af viskose og termiske tab. Tabseffekterne er specielt relevante når de geometriske dimensioner af det akustiske domæne bliver små, hvilket ofte er tilfældet i akustiske transducere og høreapparater. Computerbaserede numeriske beregningsværktøjer, såsom finite element metoden, kan bruges til a modellere og undersøge kvaliteten af et akustiskapparat uden brugen af bekostelige prototyper. At inkludere de akustiske tab i finite element metoden gør beregningsarbejdet betydeligt tungere, hvilket kan gøre det svært at realisere simuleringer med normal computerhardware. Boundary element metoden udgør et interessant alternativ til finite element metoden. Med denne er det muligt at inkludere tab og på samme tid undgå såkaldt grænselagsdiskretisering. Implementeringen af boundary element metoden gør på den anden side brug af tangentielle afledte koblingstermer beregnet med finit difference, hvilket kan føre til en uønsket beregningsunøjagtighed.

Dette ph.d. arbejde, præsenterer to nye koblingsstrategier som undgår brugen af finite difference, ved enten at bruge boundary element metoden eller shape funktioner til at estimere de tangentielle afledte. Med numeriske eksperimenter bliver det vist at de to nye koblingsstrategier giver øget stabilitet og kan minimere beregningsfejl.

Desuden bliver en gradientbaseret formoptimeringsteknik udviklet der er baseret på den forbedrede boundary element metode. Formoptimeringsteknikken er demonstreret ved at optimere absorptionskoefficienten af henholdsvis kvartbølge- og helmholtzresonatorer der er placeret i enden af et impedansrør. Formoptimeringsresultater viser at høje absorptionsværdier kan kun opnås når de viskose og termiske tab er modelleret præcist. Den udviklede formoptimeringsteknik har et fremtidigt potentiale til at forbedre designet af akustiske apparater der kræver tabsmodellering.

Acknowledgements

First of all, I am grateful for all the help and support that my supervisors Vicente and Niels have given me, even in the darkest hour. Our many discussions and their profound knowledge in the areas of numerical methods, viscothermal losses and optimization have made this project possible.

I would like to thank everyone from CAMM for the many helpful discussions, comments and suggestions given during our meetings. Also, a big thanks to the Acoustic Technology group and fellow PhD students for making a pleasant and joyful research environment.

During my stay in Munich at the Chair of Vibroacoustics of Vehicles and Machines, I had the pleasure of discussing Boundary Element Method with Steffen Marburg which greatly helped me progress with difficult parts of the work - for that I am grateful. I would also like to thank everyone at the chair for having me and discussing many different aspects of acoustics.

Furthermore, I would like to thank José Sánchez-Dehesa for supplying interesting study cases and measurements, but also the discussions on viscothermal losses and their impact on novel acoustic devices have been valuable.

Also a big thanks to Peter Møller Juhl who was the first to introduce me to the exciting world of Boundary Element Method.

Last, but not least, the biggest thanks to family, friends and Elisabeth for always being supportive and being there, no matter what.

Publications

The thesis is based on the following papers.

Paper A V. Cutanda Henríquez, P. Risby Andersen, J. Søndergaard Jensen, P. Møller Juhl and J. Sánchez-Desa, *A Numerical Model of an Acoustic Metamaterial using the Boundary Element Method Including Viscous and Thermal Losses*, Journal of Computational acoustics, (2016), doi.org/10.1142/S0218396X17500060

Paper B P. Risby Andersen, V. Cutanda Henríquez, N. Aage and J. Sánchez-Desa, *Visco-thermal effects on an acoustic cloak based on scattering cancellation*, Proceedings from the 6th conference on Noise and vibration emerging methods, 7-9 May (2018), Ibiza (Spain)

Paper C P. Risby Andersen, V. Cutanda Henríquez, N. Aage and S. Marburg *A two dimensional acoustic tangential derivative boundary element method including viscous and thermal losses*, Journal of Computational and Theoretical Acoustics, (2018), doi.org/10.1142/S2591728518500366

Paper D V. Cutanda Henríquez and P. Risby Andersen, *A three-dimensional acoustic Boundary Element Method formulation with viscous and thermal losses based on shape function derivatives*, Journal of Computational and Theoretical acoustics, (2018) , doi.org/10.1142/S2591728518500391

Paper E P. Risby Andersen, V. Cutanda Henríquez and N. Aage, *Shape optimization of microacoustic devices including viscous and thermal losses*, (2018)
(Submitted to the Journal of Sound and Vibration)

A conference publication written during the course of the PhD, but not included in the thesis:

Risby Andersen, P., Cutanda Henríquez, V., Aage, N. and Marburg, S., *Numerical Acoustic Models Including Viscous and Thermal losses: Review of Existing and New Methods*, DAGA, 6-9 March (2017), Kiel (Germany)

Contents

Chapter 1

Introduction

1.1 Motivation

The popularity of small electronic mobile devices, such as the smartphone, has created a need for acoustic transducers that maintain high performance when incorporated into confined spaces. In other acoustic devices, like hearing aids, the reduced device size is necessary to improve the usability for the end-user, yet at the same time achieve accurate reproduction of acoustic signals. Common for these acoustic device types is that their size is small, and that sound waves need to propagate in complicated narrow channels and chambers. To accurately model and estimate the propagation of sound in such scenarios will require appropriate modelling methods that include the effect of viscosity and thermal conduction. Viscosity and thermal conduction will in narrow passages act as a loss mechanism that attenuates and changes the phase of sound waves. Sometimes, the effect of losses is so significant that if neglected, results may become inaccurate [1, 2, 3, 4].

On the other hand, in many situations, sound waves are usually adequately modelled without directly accounting for viscous and thermal dissipation, and losses can typically be included using simple impedance conditions. If possible, it is often attractive to neglect, or model dissipation with simplified assumptions, since direct modelling and incorporation of the acoustic viscous and thermal effects into, e.g., numerical methods such as the Finite Element Method (FEM) or Boundary Element Method (BEM) comes at a significant computational cost. Additionally, it can be challenging to predict if the inclusion of viscous and thermal dissipation is necessary.

Besides the aforementioned mobile devices and hearing aids, it is well known that losses can significantly influence acoustic MEMS transducers [5, 6], condenser microphones [7, 8, 9], compression horn drivers [10, 11, 12] and the importance of losses can even be found in room acoustics, where the characterisation of micro-perforated

absorbers requires modelling of viscothermal effects [13, 14].

In recent years, acoustic metamaterials have been given much attention in the literature. Acoustic metamaterials are artificial structures created from scatters and resonators organised in periodic patterns [15]. If observed as a whole, metamaterials can show extraordinary properties, e.g. negative speed of sound and/or negative bulk modulus. The understanding of how viscous and thermal loss influences acoustic metamaterials is only sparsely studied in the literature, but examples have been appearing during this project [16, 17, 18, 19] and Paper A also studies the viscothermal effects on a metamaterial.

Computer-based numerical simulations tools, such as the FEM and the BEM, are valuable when investigating and improving the broad range of acoustic devices discussed so far. Simulations allow engineers and researchers to predict the physical behaviour of such sophisticated devices, which can reduce the need for costly prototyping or give a more profound understanding of an acoustic phenomenon. Interpretation of simulations are often difficult, and ideas on how to improve a specific device design can be even harder. In such cases, optimization based on numerical methods has proven to be a helpful tool in discovering new high performing acoustic designs and creating otherwise non-intuitive design choices [20, 21, 22].

However, the acoustic devices discussed so far require modelling of viscous and thermal losses. In the literature, numerical acoustic optimization methods applicable to more general acoustic problems that include accurate modelling of viscous and thermal losses are very scarce. To the best of this author's knowledge, only one example exists of such optimization. In a very recent publication, Christensen [23] showed the possibility of performing topology optimization using FEM by applying the so-called low reduced frequency formulation, making it possible to topology optimize the cross-section of tubes and slits.

1.2 Project goals

In this project, methods for improving the reliability and stability of an existing BEM implementation that incorporates viscous and thermal losses are sought. The current BEM implementations are subject to certain shortcomings that can lead to undesired inaccuracies in some situations.

Additionally, it is the desire to improve the understanding of how viscous and thermal

losses impact novel acoustic devices such as metamaterials, but also use these often complex acoustic devices to benchmark the viscothermal BEM.

Finally, it is the goal to develop a shape optimization technique that relies on the improved viscothermal BEM and is capable of including losses accurately. The shape optimization technique has the potential to advance the knowledge of how viscothemal losses affects acoustic optimization and improve the design of acoustic devices where losses are relevant.

1.3 Thesis structure

The thesis is organized as follows. In Chapter 2, the mathematical description of sound waves in a lossless fluid is introduced, and the fundamentals of the corresponding FEM and BEM are explained. Chapter 3 gives an overview of the state-of-the-art methods that incorporate viscous and thermal losses, with special attention to full FEM and BEM implementations. At the end of the chapter, two modelling examples from Paper A and Paper B, that investigate the effect of viscous and thermal losses on a metamaterial and an acoustic cloaking device, are summarised. Chapter 4 introduces Paper C and Paper D, where new ideas on how to improve the existing viscothermal BEM is given. Chapter 5 presents general acoustic shape optimization methods and discusses the viscothermal shape optimization technique developed in Paper E. Additionally, the Chapter also includes unpublished shape optimization results of an acoustic cloaking device. Finally, in Chapter 6, the included papers and the thesis are summarized with some general conclusions and suggestions for future research.

Chapter 2

Isentropic propagation of sound waves

2.1 The wave equation

The mathematical description of sound waves in an elastic medium can be deduced from the fundamental equations of fluid mechanics, i.e., the conservation of mass, energy and momentum equations. The equations describe the motion of a fluid including, e.g. non-linearities, viscosity and thermal conduction [1]. Direct evaluation of acoustic wave propagation from the fundamental equations is, in most cases, not feasible due to their complexity. Therefore, assumptions simplifying the general problem are desirable to make the computational effort reasonable.

In acoustics, the propagation of sound waves is usually based on the assumption that the fluctuations around the equilibrium are so small that linearity is a good approximation. Besides linearity, the thermodynamic process of sound waves can be approximated as adiabatic and reversible, i.e. an isentropic process - meaning that no acoustic energy is lost. As an addition, if air is approximated as an ideal gas, the result is the wave equation: [1]

$$\nabla^2 p(\mathbf{x},t) - \frac{1}{c_0^2}\frac{\partial p(\mathbf{x},t)}{\partial t} = 0 \tag{2.1}$$

where $p(\mathbf{x},t)$ is a pressure perturbation of the static pressure at the location $\mathbf{x}$ at time t and c_0 is the speed of sound in air.

It is convenient to solve the wave equation in the frequency domain, which can be accomplished by assuming a time-harmonic solution to Eq. (2.1), that is

$$p(\mathbf{x},t) = \Re\left\{p(\mathbf{x})e^{i\omega t}\right\} \tag{2.2}$$

where i is the imaginary unit. Substitution of Eq. (2.2) into Eq. (2.1) and omitting the time-dependency leads to

$$\nabla^2 p(\mathbf{x}) + k^2 p(\mathbf{x}) = 0 \tag{2.3}$$

which is commonly known as the Helmholtz equation. The wavenumber is $k = \frac{\omega}{c_0}$ where ω is the angular frequency. The included papers only consider time-harmonic solutions to the wave equation. For simplicity, we will in the following and in the included papers exclude the $\mathbf{x}$ dependency.

Modelling of isentropic acoustic wave problems, that extends beyond analytical solutions, can be accomplished with numerical methods. In this work, two methods are used, namely the FEM and the BEM.

2.2 Finite Element Method

The FEM is a numerical domain method, first introduced for structural stiffness and deflection analysis [24], and now widely used to approximately solve physical phenomena.

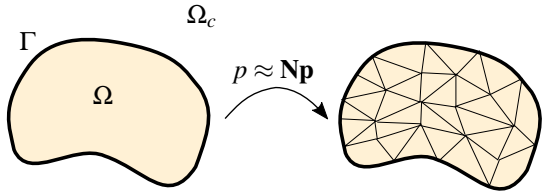

Figure 2.1: On the left, a two-dimensional illustration of the domain Ω. On the right, FEM discretization in terms of triangles. Here, Γ represents the boundary and Ω_c is the complementary domain.

To apply the FEM to the Helmholtz equation, Eq. (2.3) is multiplied with a test function ϕ and integration is carried out over the domain Ω (illustrated in Fig. 2.1). This yields the expression

$$\int_\Omega \phi \left[\Delta p + k^2 p\right] d\Omega = 0. \tag{2.4}$$

By Green's first identity the term containing the Laplace operator is transformed into a domain and a boundary integral, so that

$$-\int_\Omega \nabla\phi \cdot \nabla p \, d\Omega + \int_\Gamma \phi \left(\nabla p \cdot \mathbf{n}\right) d\Gamma + \int_\Omega k^2 \phi p \, d\Omega = 0. \tag{2.5}$$

Eq. (2.5) is the weak form of Eq. (2.3). Assuming that the pressure can be approximated by $p \approx \mathbf{Np}$, where $\mathbf{N}$ is the interpolation functions (or shape functions), and applying the Galerkin approach where the test function is assumed to be same as the interpolation functions. The resulting expression is the FEM description applicable for estimation of acoustic isentropic wave propagation,

$$-\int_{\Omega} \nabla \mathbf{N}^T \cdot \nabla \mathbf{N} d\Omega \mathbf{p} + \int_{\Gamma} \mathbf{N}^T (\nabla \mathbf{Np} \cdot \mathbf{n}) d\Gamma + \int_{\Omega} k^2 \mathbf{N}^T \mathbf{N} d\Omega \mathbf{p} = \mathbf{0} \tag{2.6}$$

where the terms, from the left to the right, are called the acoustic; stiffness, natural boundary condition and mass matrices, respectively. The matrices are real, sparse and symmetric. However, in the case of, e.g., damping, this might not always be true.

2.3 Boundary Element Method

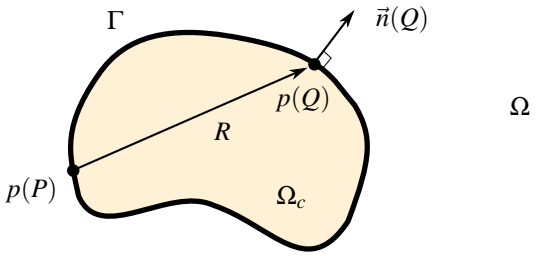

Figure 2.2: Illustration of the direct BEM by collocation.

The isentropic BEM takes its starting point at Eq. (2.4), where the test function is replaced by the fundamental solution $G(R)$. To remove the domain integrals, Green's first identity is applied twice, and, after some manipulation, we arrive at the Kirchoff-Helmholtz integral equation: [25, 26]

$$C(P)p(P) = \int_{\Gamma} \frac{\partial G(R)}{\partial n(Q))} p(Q) d\Gamma - \int_{\Gamma} G(R) \frac{\partial p(Q)}{\partial n(Q)} d\Gamma \tag{2.7}$$

where the first term on the right hand side is the double layer potential, and the second term on the right hand side is the single layer potential. In the presented work, only direct collocation BEM is considered. The process of collocation is illustrated in Fig. 2.2. Here, P is the collocation point, Q is an integration point on the generator and $R = |P - Q|$ is the distance between collocation point and integration point. Only the

most common form of collocation, where P is located at nodal points on the boundary element, is used. Additionally, $C(P)$ is the geometric depended integral free term, which is $\frac{1}{2}$ on a smooth boundary and 1 in the domain. In the case of collocation points at non-smooth boundaries, $C(P)$ is determined by following the procedure in Ref. [27]. The fundamental solution $G(R)$ is defined in two and three dimensions by

$$\textbf{2D:} \qquad G(R) = \frac{1}{2\pi} K_0(ikR) \tag{2.8}$$

$$\textbf{3D:} \qquad G(R) = \frac{e^{-ikR}}{2\pi R}. \tag{2.9}$$

In Eq. (2.8), K_0 is the modified Bessel function of the second kind of zero order. After discretization, i.e. assuming that $p \approx \mathbf{Np}$, the BEM system of equations is

$$\mathbf{Ap} - \mathbf{B}\frac{\partial \mathbf{p}}{\partial n} = \mathbf{0}. \tag{2.10}$$

The matrices in direct collocation BEM are complex, fully populated and non-symmetric. Other BEM exists where symmetry can be obtained [28]. Nevertheless, the simplest form of BEM is adopted in this project. A large part of the BEM simulations is performed using the OpenBEM [29] research code implemented in MATLAB® as the foundation, but also a faster two-dimensional compiled C++/MEX code has been developed. However, the faster compiled code is only used in Paper E.

2.3.1 Non-uniqueness

Non-uniqueness (sometimes denoted as irregular frequencies or spurious modes) is a purely mathematical problem arising in the direct BEM due to ill-conditioned matrices in exterior Neumann problems. It was first described in a paper by Schenck [30], where the author suggested the Combined Helmholtz Integral Equation Formulation (CHIEF) to overcome the problem. By selecting what is commonly known as CHIEF-points, an overdetermined system of equations can be created that is solved in the least square sense. The CHIEF-points are located in the complementary domain Ω_c (see Fig. 2.2) where the acoustic pressure is expected to be equal to zero. However, it is difficult to choose an appropriate number of CHIEF-points and their performance is location and frequency dependent. A strategy to overcome some of these implications is discussed in e.g Ref. [31].

Another more robust method to eliminate the problem of non-uniqueness is the Burton and Miller Method [32]. In this method, non-uniqueness is removed by creating

an additional boundary element equation derived from taking the normal derivative of Eq. (2.7). By combining the normal derivative equation with Eq. (2.7) as a linear combination using a complex coupling parameter, the system becomes free of irregular frequencies. The choice of coupling parameter was recently discussed in a publication by Marburg [33], where the author showed that a large part of the BEM community is utilizing an incorrect sign of the coupling parameter. Besides the coupling parameter, one of the implications of the Burton-Miller method is the requirement of a unique normal at the collocation point and the cumbersome evaluation of hypersingular integration kernels that appear in the normal derivative equation.

In this project, the non-uniqueness problem is encountered in Paper B, where it is solved by utilizing the CHIEF.

2.4 Boundary conditions

In the included papers, the boundary conditions encountered when solving the isentropic wave problems are pressure, normal velocity, normal impedance and unbounded conditions. The pressure condition is expressed as a superposition of an incident pressure p^I and the scattered pressure p^S, so the total pressure is

$$p = p^I + p^S \quad \text{on} \quad \Gamma. \tag{2.11}$$

The relation between the normal fluid velocity v_n and the normal pressure gradient is given by

$$\nabla p \cdot \vec{n} = \frac{\partial p}{\partial \vec{n}} = -i\omega\rho_0 v_n \quad \text{on} \quad \Gamma \tag{2.12}$$

where ρ_0 is the static density of the fluid. Normal impedance conditions can be included by

$$v_n - v_s = \frac{1}{Z_n} p \quad \text{on} \quad \Gamma \tag{2.13}$$

with v_s being the structural velocity and Z_n being the normal impedance. In the case of unbounded domains, the Sommerfeld radiation condition needs to be fulfilled, which is

$$\lim_{r\to\infty} r^{\frac{n-1}{2}} \left[\left(\frac{\partial p}{\partial r} + ikp \right) \right] = 0 \tag{2.14}$$

where r is the radial distance to a source and n is the spatial dimension. In the BEM the Sommerfeld radiation condition is implicitly fulfilled; this is however not the case in FEM. Historically, the implicit fulfillment of the Sommerfeld radiation condition is

one of the reasons why BEM has been a popular method in the field of acoustics and electromagnetics. In the FEM, some truncation of the domain is necessary. The simplest way to approximate unbounded domains with the FEM is to use an appropriate impedance boundary condition at the truncation. Unfortunately, in many cases this will lead to unwanted reflections. Other more elaborate methods exist, such as infinite elements [34, 35, 36] and perfectly matched layers (PML) [37, 38, 39]. In these methods, an artificial region surrounding the computational domain is created where the wave is more efficiently attenuated and reflections are limited.

In the papers A, B and D, isentropic FEM simulations are performed using COMSOL Multiphysics® [40] and unbounded domains are handled with PML.

Chapter 3

Viscothermal losses in acoustics and its modelling

In this PhD project, the goal has been to explore when the assumptions of isentropic wave propagation are insufficient, meaning that viscous and thermal losses cannot be neglected, but also to improve the reliability of an existing BEM implementation that incorporates such losses. Therefore, in this chapter, we will first introduce state-of-the-art modelling methods that can account for acoustic viscous and thermal dissipation. Special theoretical attention is given to the viscothermal BEM implementation since it is the foundation and starting point of the next chapter. Finally, at the end of this chapter, two modelling examples from Paper A and Paper B are introduced where the effects of viscous and thermal losses on a metamaterial and an acoustic cloaking device are investigated.

3.1 State-of-the-art

The interest in acoustic viscous and thermal losses dates back to at least Kirchhoff [41] and Rayleigh [42]. Kirchhoff studied the attenuation of sound waves in cylindrical tubes due to viscous and thermal effects, and showed that the full linearised Navier-Stokes equations, i.e. the linearised conservation of mass, energy and momentum, can be decoupled into independent acoustic, entropic and vortical modes that are only coupled through boundary conditions. The entropic mode is described in terms of thermal diffusion, and the vortical mode as momentum diffusion. Often, the entropic and vortical modes are called the thermal pressure and viscous velocity, respectively. A naming convention that is also adopted in the included papers. Additionally, the decoupling is referred to as the Kirchhoff decomposition or Kirchhoff's dispersion law. It is called the dispersion law because the decoupled modes have a corresponding wavenumber that is dependent on the angular frequency. The decomposition allowed Kirchhoff to analytically study the attenuation of sound waves in cylindrical tubes. Later, Rayleigh

revisited Kirchhoff's work and included propagation of sound in very narrow tubes. In this case, the entire cross-section of the tube can be considered a thermodynamic isothermal process which simplifies the problem, so only viscosity needs to be considered. In Rayleigh's revisit, sound propagation in two-dimensional slits is also discussed.

Zwikker and Kosten [43] proposed an approximate evaluation of Kirchhoff's original work, distinguishing between low (narrow tube) and high (wide tube) frequencies. Their approach was later named the low reduced frequency (LRF) method by Tijdeman [44]. In the publication by Tijdeman, a range of approximate methods proposed by several authors on the propagation of sound waves in cylindrical tubes are discussed; the finding is that the LRF approach is the best approximate solution over a broad range of frequencies. In the LRF method, it is assumed that the acoustic wavelength is much larger as compared to the cross-section of the tube, and that the sound pressure can be considered constant across the cross-section. With this, it is possible to split the equations into a cross-sectional and propagational direction whereby propagation in the tube can be described by a propagation constant. The propagation constant is a measure of how the amplitude and the phase changes in the propagation direction, making it possible to describe sound propagation in tubes as a purely one-dimensional problem. Several authors have later extended the LRF model beyond circular tubes to include arbitrary cross-sectional shapes relying on some numerical calculations [45, 46]. A very elaborate introduction to the LRF model can, for example, be found in Beltman's PhD thesis [47] and in the Refs. [48] and [49]. Beltman also shows the possibility of using the LRF model in combination with FEM [50]. While the LRF method is an efficient way to include viscothermal losses into FEM, it is limited to the study of waveguides and slits. Additionally, the LRF approach will fail to give accurate solutions in the case of higher order acoustic modes where the pressure cannot be considered constant.

The approximate methods treating sound propagation in simple tubes can also be extended into transmission line theory, where series impedances and shunt admittances can be extracted to account for attenuation and phase shifts [51, 52, 53]. With transmission line theory more complex acoustic systems containing several tubes and cavities can be studied [54].

The modelling approaches considered so far are somewhat limited in their application with requirements to the specific geometry. It is possible to treat more general problems using more elaborate numerical methods, such as the FEM and the BEM. FEM models that include viscothermal dissipation, and are suitable for simulations of arbitrary geometries, can either be full models that solve the full linearised Navier-Stokes

(FLNS) equations without any simplification or methods where additional approximate assumptions are made to the governing equations. Among the authors who have discussed full models are Malinen [55], Nijhof [56], Cheng [57], Joly [58] and Kampinga [59].

Malinen [55] uses a mixed formulation with an auxiliary unknown, the temperature and the velocity as the dependent variables. However, it turns out that the auxiliary unknown is just the density. In Malinen's formulation the equations are discretized using MINI elements. Nijhof's [56] implementation is very similar to that of Malinen, but uses the pressure as the unknown variable instead of density. In the publication by Nijhof, the two implementations are compared through convergence studies, showing very similar results. It should be noted that using the pressure as the dependent variable should be considered the more appropriate choice since the density will in fact form boundary layers, which is not the case for the pressure. Cheng [57] also uses a mixed formulation with displacement and pressure as dependent variables, but the formulation completely neglects thermal conduction. In Joly's work, the final system of equations only depends on velocity and temperature.

Kampinga [59] establishes a complex symmetric mixed formulation with temperature, pressure and velocity as the dependent variables. The complex symmetric formulation has several advantages over the previous implementations since solvers like PARDISO and SPOOLS can take advantage of complex symmetry. As a result, the computational time is faster, and the method yields reduced memory requirements. The publication by Kampinga includes convergence studies of several finite elements. From the convergence studies, it is shown that Crouzeix Raviat or Taylor Hood elements with velocity and temperature discretized by quadratic shape functions yields the best results. In general, the FLNS FEM publications considers mixed formulations to avoid so-called locking in the case of a nearly incompressible fluid; the same phenomenon is also encountered in elastodynamics. One of the drawbacks of the FLNS implementations is the increased system size due to the additional variables in the final system of equations. This adds to the computational time and memory requirement. Additionally, the FLNS FEM requires careful meshing of the boundary layers to accurately resolve viscous an thermal effects in the vicinity of the boundaries. Martins [60], for example, studies boundary layer meshing and its importance for the accuracy. An implementation of the FLNS can be found in COMSOL®. The COMSOL® implementation is very comparable to the implementation discussed here by Kampinga, with the depended variables being pressure, temperature and velocity.

The computational complexity of the FLNS FEM implementations often makes three-

dimensional simulations with modest hardware problematic. Therefore, several authors have investigated approximate methods which are still reliable but computationally cheaper. Here we will reproduce the classification of approximate methods given by Kampinga [4]. Numerical approximate acoustic viscothermal models can be categorized as boundary layer impedance (BLI) models, the aforementioned LRF models or the sequential linearised Navier-Stokes (SLNS) model.

In the BLI models, simplifying assumptions are used to create impedance-like conditions that account for the boundary layer effects. The requirement is that the geometric dimensions are larger as compared to the boundary layer thickness. Bossart [61] proposes an admittance-like condition solved in a three step procedure. First, an isentropic FEM or BEM pressure solution is calculated. The isentropic solution is then used to approximate a tangential wavenumber which is applied in a final FEM or BEM calculation. In the work by Schmidt [62] so-called Wentzell type boundary conditions are used to include viscous losses through the normal pressure derivative, which can be substituted directly into the weak from of the Helmholtz equation. In a very recent publication by Berggren [12], a similar Wentzell type boundary condition is derived that also includes thermal losses. The BLI models proposed by Schmidt and Berggren are interesting because they are of the same complexity as the regular isentropic Helmholtz problem and therefore very efficient and do not require meshing of boundary layers. On the other hand, one must be careful when using the method in very narrow regions where boundary layers can overlap.

The SLNS is an approximate FEM proposed by Kampinga [63, 4]. It is deduced from similar assumptions as the LRF model, but is not limited to simple tubes. In the SLNS method, two completely uncoupled viscous and thermal fields governed by inhomogeneous wave equations are solved. The viscous and thermal fields are then used as input to a homogeneous wave equation where the pressure is the only unknown variable. Several advantages can be identified in terms of computational speed and the ability to accurately handle narrow gaps with overlapping boundary layers. Computationally, each equation reassembles similar complexity as the isentropic wave equation. However, careful meshing of the boundary layers is necessary when computing the viscous and thermal fields.

Three authors have treated modelling of acoustic viscous and thermal losses using the BEM; namely Dokumaci [64, 65], Karra [66, 67], and Cutanda Henríquez [7, 68, 69, 70].

In the BEM formulation by Dokumaci [64] viscosity is included through a boundary

layer approximation, assuming that the viscous velocity can be approximated purely through its boundary tangential component. The approach was later extended to also include thermal losses [65]. Due to the way viscosity is included, the method can only be considered approximate.

Using a variational BEM formulation, Karra [67], includes losses. However, the formulation completely neglects viscous effects and only considers thermal losses which makes the development much easier. The approach is a direct application of the generalised version of Kirchhoff's original dispersion relation developed by Bruneau [71]. Bruneau's generalisation extents the dispersion relations to include both bulk viscosity and evanescent modes. Hereafter, the generalised approach by Bruneau is referred to as the Kirchhoff decomposition.

Cutanda Henríquez extended the idea of Karra using the Kirchhoff decomposition as a convenient starting point for a direct collocation BEM implementation. The Kirchhoff decomposition consists of two scalar wave equations describing the acoustic and thermal pressures, and a vector wave equation with the viscous velocity as the variable. Each of the equations can be discretized separately with BEM and coupled through boundary conditions. With Schur complement operations, it is possible to establish a system of equations relating the acoustic pressure to the boundary normal and tangential velocities. However, this requires the evaluation of coupling terms described by both first and second order surface tangential derivatives of the acoustic pressure. In early implementations, the coupling terms were develop individually for specific geometries [54], but the model was later generalised to handle arbitrary geometries, facilitating both axisymmetric and full three-dimensional simulations. Even though the implementation can handle more general geometries, the coupling methodology in the Refs. [68] and [70] uses finite difference. The use of finite difference is known to be subject to several shortcomings and is cumbersome to implement in three dimensions.

3.2 General assumptions

In the following as well as in the included papers, it is assumed that acoustic wave propagation in a viscous and thermally conductive fluid can be based on the assumptions of:

- Linearity and time-harmonic wave behaviour.
- The medium is considered uniform, at its equilibrium and without flow.

- The material properties are based on a Newtonian fluid, follow Fouriers law of heat conduction and the fluid (air) can be approximated as an ideal gas.
- The wavelength and the dimensions of the computational domain is larger than the molecular mean-free-path (approximately 10^{-7} m for air at ambient conditions).

3.3 Viscothermal FEM

In the papers A, B, C and E, COMSOL's FEM implementation of the time-harmonic FLNS is mainly used as a comparative tool to validate the viscothermal BEM simulations. The time-harmonic FLNS is given by the linearised conservation of mass, energy and momentum equations, which are

$$i\omega\rho + \rho_0 \nabla \cdot \vec{v} = 0 \tag{3.1}$$

$$i\omega\rho_0 C_p T - \lambda \Delta T - i\omega p = 0 \tag{3.2}$$

$$i\omega\rho_0 \vec{v} = -\nabla p + \left(\mu_B + \frac{4}{3}\mu\right)\nabla(\nabla \cdot \vec{v}) - \mu \nabla \times \nabla \times \vec{v} + \vec{f} \tag{3.3}$$

where the properties of the medium are characterised by the static density ρ_0, the specific heat at constant pressure Cp, the thermal conductivity λ, the shear viscosity μ and the bulk viscosity μ_B. It is possible to include volumetric body forces through the vector $\vec{f}$ (sometimes volumetric heat sources are also included into the energy equation, but they are in this case not used and simply ignored). Only Paper A makes use of the volumetric force term, where it is applied to artificially excite the waveguide in which the metamaterial is located. The volumetric force term is specific for the FEM simulations and is not used when discussing the implementation of the viscothermal BEM.

Besides pressure fluctuations, the FLNS also includes small fluctuations in temperature, density and velocity, given by the variables T, ρ and $\vec{v}$, respectively. To solve the Eqs. (3.1)-(3.3), it is necessary to eliminate one of the acoustic variables. This is accomplished by substitution of the linearised ideal gas law into Eq. (3.1) which eliminates the density, whereby only pressure, temperature and velocity are the depended variables.

The FLNS equations can be solved with the FEM by directly applying the Galerkin method as presented in Section 2.2. By multiplication of corresponding test functions, integration over the domain Ω and applying Green's formula to eliminate the second

order derivatives, the weak form of Eqs. (3.1)-(3.3) can be established (assuming that the density is eliminated from Eq. (3.1)). The weak form and the coupled system is not presented here, but can be found in e.g. Ref. [59].

3.3.1 Boundary conditions

Thermal conduction and viscosity are the two primary mechanisms responsible for losses in confined acoustic domains. Their effect is relevant in the vicinity of boundaries where thermal and viscous boundary layers form as a consequence of boundary conditions.

Temperature boundary condition

The heat capacity and thermal conductivity of the boundaries are usually much greater as compared to the fluid. Therefore, it is in most cases reasonable to consider the boundaries as isothermal, so that

$$T = 0 \quad \text{on} \quad \Gamma. \tag{3.4}$$

At the boundary, the acoustic temperature fluctuations are forced to zero, and as a result, an exchange of heat between the boundary and the fluid will occur. This creates a transition region in the proximity of the boundary where the temperature behaviour changes from isothermal into that of the bulk (the bulk is the region where wave propagation can be considered isentropic). The transition region is commonly known as a thermal boundary layer. Fig. 3.1 illustrates the process and the formation of thermal boundary layers.

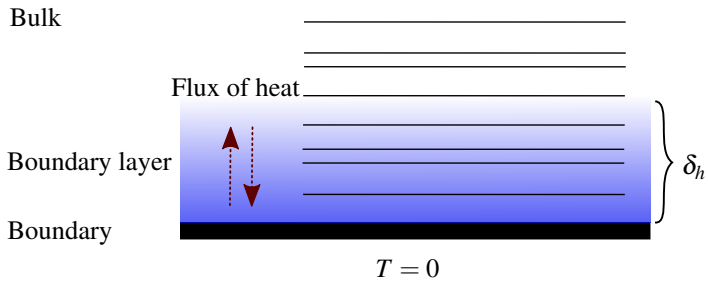

Figure 3.1: An illustration of the formation of a thermal boundary layer. An incoming plane wave has associated pressure changes, but also changes in temperature. Since the boundary has a higher heat capacity, the boundary temperature can be considered isothermal. Therefore, the temperature fluctuations of the incident wave are forced to zero at the boundary. This creates the thermal boundary layer where the behaviour changes from isothermal into that of the bulk. The thickness of the boundary layer is given by δ_h.

The thickness of the thermal boundary layer as a function of the frequency f is [1, p. 286]

$$\delta_h = \sqrt{\frac{2\lambda}{\rho_0 \omega C_p}} \overset{air}{\approx} 2.5 \frac{1}{\sqrt{f}} \text{mm} \tag{3.5}$$

which in the audible range, assuming the medium to be air, is approximately between 550 μm to 20 μm.

Velocity boundary condition

Frictional forces between the boundary and the fluid will restrict movement of the fluid. It is usually said that the fluid particles closest to the boundary tend to stick to the boundary, resulting in a no-slip boundary condition where

$$\vec{v} = \vec{v}_b \quad \text{on} \quad \Gamma, \tag{3.6}$$

with $\vec{v}_b$ being the the boundary velocity. In the case of a stationary boundary $\vec{v}_b = 0$. As the distance to the boundary increases, the frictional effect of the boundary will be reduced and the particle velocity gradually adopts the behaviour of the bulk. This transition region is denoted the viscous boundary layer. Fig. 3.2 illustrates the formation of viscous boundary layers.

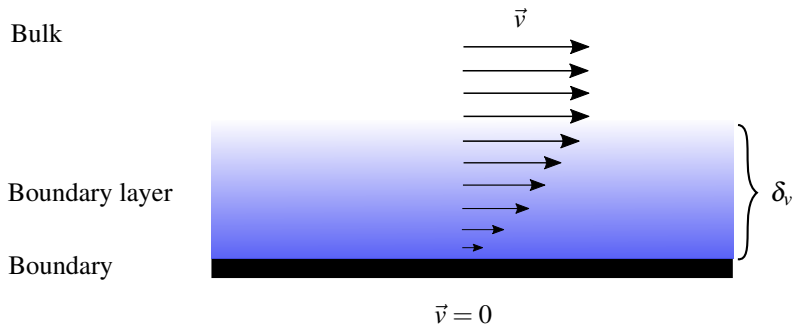

Figure 3.2: An illustration of the formation of viscous boundary layers. Due to frictional forces between the boundary and the fluid, the particles closest to the boundary will tend to stick to the boundary forming what is commonly known as a viscous boundary layer. The thickness of the boundary layer is given by δ_v

The thickness of viscous boundary layers as a function of the frequency f is [1, p. 286]

$$\delta_v = \sqrt{\frac{2\mu}{\rho_0 \omega}} \overset{air}{\approx} 2.1 \frac{1}{\sqrt{f}} \text{mm}. \tag{3.7}$$

In air, the thicknesses of the viscous and thermal boundary layers are very comparable, which yields a Prandtl number close to unity.

3.4 Viscothermal BEM

We will now review the BEM implementation including viscous and thermal losses as presented by Cutanda Henríquez in the Refs. [70] and [68]. For simplicity only two dimensions are considered as opposed to the axissymmetric and three-dimensional implementations found in the references. The starting point for the BEM implementation is the Kirchhoff decomposition of the FLNS equations. The Kirchhoff decomposition is a convenient starting point, since regular acoustic BEM can be deployed directly without modification. The Kirchhoff decomposition of the FLNS leads to the equations [71]

$$\Delta p_a + k_a^2 p_a = 0 \tag{3.8}$$

$$\Delta p_h + k_h^2 p_h = 0 \tag{3.9}$$

$$\Delta \vec{v}_v + k_v^2 \vec{v}_v = \vec{0} \tag{3.10}$$

where p_a is the acoustic pressure, p_h is the thermal pressure, $\vec{v}_v$ is the viscous velocity, k_a is the acoustic wavenumber, k_h is the thermal wavenumber and k_v is the viscous wavenumber. The wavenumbers are in this case complex and depended on the frequency and the physical properties of the fluid (see e.g Appendix A in Ref. [70] for their definition). While the Eqs. (3.8)-(3.10) are on the Helmholtz form, Eqs. (3.9) and (3.10) should rather be considered as diffusion-like equations, where the thermal pressure and the viscous velocity (entropic and vortical modes) only exist in the vicinity of the boundary.

As a consequence of the Kirchhoff decomposition, the total pressure is split into a superposition of the acoustic and the thermal pressure so that

$$p = p_a + p_h. \tag{3.11}$$

And in a similar way, the total velocity is split into

$$\vec{v} = \vec{v}_a + \vec{v}_h + \vec{v}_v \tag{3.12}$$

where $\vec{v}_a$ and $\vec{v}_h$ are the irrotional part of the velocity associated with p_a and p_h, respectively. The rotational part of the velocity is the viscous velocity. Therefore, the relations

$$\nabla \times (\vec{v}_a + \vec{v}_h) = 0 \quad \text{and} \quad \nabla \cdot \vec{v}_v = 0 \tag{3.13}$$

should be fulfilled. If each of the Eqs. (3.8)-(3.10) is discretized separately using regular collocation BEM as presented in Section 2.3, the result is

$$\mathbf{A}_a \mathbf{p}_a - \mathbf{B}_a \frac{\partial \mathbf{p}_a}{\partial \vec{n}} = \mathbf{0} \tag{3.14}$$

$$\mathbf{A}_h \mathbf{p}_h - \mathbf{B}_h \frac{\partial \mathbf{p}_h}{\partial \vec{n}} = \mathbf{0} \tag{3.15}$$

$$\mathbf{A}_v \mathbf{v}_{v,x} - \mathbf{B}_v \frac{\partial \mathbf{v}_{v,x}}{\partial \vec{n}} = \mathbf{0} \tag{3.16}$$

$$\mathbf{A}_v \mathbf{v}_{v,y} - \mathbf{B}_v \frac{\partial \mathbf{v}_{v,y}}{\partial \vec{n}} = \mathbf{0} \tag{3.17}$$

where Eq. (3.10) has been split into its Cartesian components, and the subscripts a, h and v indicates the acoustic, thermal and viscous matrices, respectively.

3.4.1 Boundary conditions

The next step is coupling of the discretized equations, i.e. Eqs (3.14) - (3.17), by assuming isothermal and no-slip boundary conditions. Due to the nature of the Kirchhoff

decomposition, the form of the boundary conditions is slightly different as presented in the FLNS FEM. In this case, the temperature is related to the acoustic and the thermal pressures through two complex constants, τ_a and τ_h, which are a function of frequency and the fluid properties. The expression for the isothermal boundary condition is

$$T = \tau_a p_a + \tau_h p_h = 0 \quad \text{on} \quad \Gamma. \tag{3.18}$$

In a similar way, the no-slip boundary condition can be described in terms of the acoustic pressure, the thermal pressure and the viscous velocity. The boundary velocity is

$$\vec{v_b} = \phi_a \nabla p_a + \phi_h \nabla p_h + \vec{v}_v \quad \text{on} \quad \Gamma \tag{3.19}$$

where ϕ_a and ϕ_h are complex constants. For the definition of τ_a, τ_h, ϕ_a and ϕ_h see e.g. Appendix A in Ref. [70]. To make the boundary conditions suitable for the BEM they are transformed into a local normal and tangential coordinate system, so

$$v_{b,n} = \phi_a \frac{\partial p_a}{\partial \vec{n}} + \phi_h \frac{\partial p_a}{\partial \vec{n}} + \vec{v}_{v,n} \quad \text{on} \quad \Gamma \tag{3.20}$$

and

$$v_{b,t} = \phi_a \frac{\partial p_a}{\partial \vec{t}} + \phi_h \frac{\partial p_a}{\partial \vec{t}} + \vec{v}_{v,t} \quad \text{on} \quad \Gamma \tag{3.21}$$

where the subscripts n and t denote the boundary normal and tangential component, respectively.

3.4.2 System of equations and coupling method

Through a lengthy Schur complement styled derivation, translating between Cartesian and local node-related boundary normal and tangential coordinates, fulfilling the boundary conditions and ensuring that $\nabla \cdot \vec{v}_v = 0$, it is possible to derive a system of equations relating the acoustic pressure to the boundary normal velocity $\vec{v}_{b,n}$ and the boundary tangential velocity $\vec{v}_{b,t}$. The resulting system of equations is expressed as [70]

$$\begin{aligned}
&\left[\phi_a \mathbf{B}_a^{-1}\mathbf{A}_a - \phi_h \mathbf{B}_h^{-1}\mathbf{A}_h \frac{\tau_a}{\tau_h} + \left(\phi_a - \frac{\tau_a}{\tau_h}\phi_h\right)\right. \\
&\times \left(\mathbf{N}_1 \circ \left(\mathbf{B}_v^{-1}\mathbf{A}_v\right)\right)^{-1} \\
&\left.\times \left(\mathbf{N}_2 \circ \left(\mathbf{B}_v^{-1}\mathbf{A}_v \mathbf{D}\mathbf{T}_1\right) + \mathbf{D}\mathbf{T}_2\right)\right] \mathbf{p}_a \\
&= \mathbf{v}_{b,n} + \left[\mathbf{N}_1 \circ \left(\mathbf{B}_v^{-1}\mathbf{A}_v\right)\right]^{-1} \times \left[\mathbf{N}_2 \circ \left(\mathbf{B}_v^{-1}\mathbf{A}_v\right) + \mathbf{D}\mathbf{T}_1\right] \mathbf{v}_{b,t}
\end{aligned} \tag{3.22}$$

where the $\circ$ operator is the so-called element-wise Hadamard product (see e.g. Appendix A in Paper C for some properties of the Hadamard product) and the matrices, $\mathbf{N}_1$ and $\mathbf{N}_2$, contain the boundary normal and tangential components at the discrete nodes. These matrices originate from a necessary translation between a Cartesian description of the viscous velocity into the local boundary normal and tangential vectors. The translation is carried out on the discrete nodes located on the generator. In fact, this procedure requires that the normal and tangential components are uniquely defined at all nodes. In other words, the boundary elements need to be C^1-continuous at collocation points. Unfortunately, this requirement is not fulfilled with regular continuous Lagrange elements. However, the implementation do use such elements. Therefore, it is necessary to calculate the normal and tangential vectors as an average when nodes are shared by multiple elements. This is a possible shortcoming of the implementation.

Another concern regarding the formulation and implementation is the matrices $\mathbf{DT}_1$ and $\mathbf{DT}_2$. These matrices contain first and second order tangential derivatives created with the use of centered finite difference schemes, and used to estimate tangential derivatives of the acoustic pressure. The use of finite difference is known to be prone to errors and its implementation is problematic when the boundaries are curved and the element size irregular. Additionally, the implementation into three-dimensions is even more cumbersome relying on Voronoi cells [68, 72, 73]. Nevertheless, the implementation as discussed here (and in other earlier versions) has been successfully applied to calculate and analyse complex viscothermal problems [7, 3, 54, 69] and is also used in Paper A and Paper B.

3.4.3 Narrow gap and low frequency breakdown

Besides the aforementioned concerns regarding the implementation and coupling method, one should be careful when performing BEM calculations containing narrow gaps. The use of the BEM in domains with narrow regions requires certain treatment, where the so-called narrow gap breakdown (or thin-shape breakdown) can lead to unwanted inaccuracies if integration is not treated correctly. The narrow gap breakdown problem is for example discussed by Martinez [74]. It is caused by the singular nature of the boundary element kernels. When boundaries are close in distance, the integration becomes nearly singular which makes regular gauss integration insufficient. To overcome the narrow gap breakdown, narrow passages encountered in the BEM implementation are treated with an adaptive recursive integration scheme [75] which is capable of treating the nearly singular integrals and accurately model narrow gaps.

Additionally, the BEM is subject to inaccuracies in low frequency interior problems due

to the absence of a quasi-static component [76, 77]. In certain viscothermal BEM problems, more specifically the condenser microphone simulations presented in Paper D, the low frequency problem is known to exist. However, it is not observed in the other test cases studied in this thesis.

3.5 Metamaterial (Paper A)

Paper A studies the influence of viscous and thermal losses on the acoustic metamaterial seen in Fig. 3.3. The particular metamaterial was originally presented and developed by Graciá-Salgado in Ref. [78]. Its design is based on unit cells containing both scatterers and quarter-wave resonators arranged in a periodic pattern. In Ref. [78], isentropic numerical and analytical experiments show that, at a certain frequency range, the unit cells experience the so-called double negative behaviour (negative effective bulk modulus and negative effective mass). As a consequence, it is possible to observe special wave propagation phenomena such as tunnelling through narrow channels, control of the radiation field, perfect transmission through sharp corners and power splitting. However, measurements of the unit cells placed in a waveguide do not show the expected properties. It is mentioned by the authors in Ref. [78] that the discrepancies are believed to be caused by viscous and thermal damping.

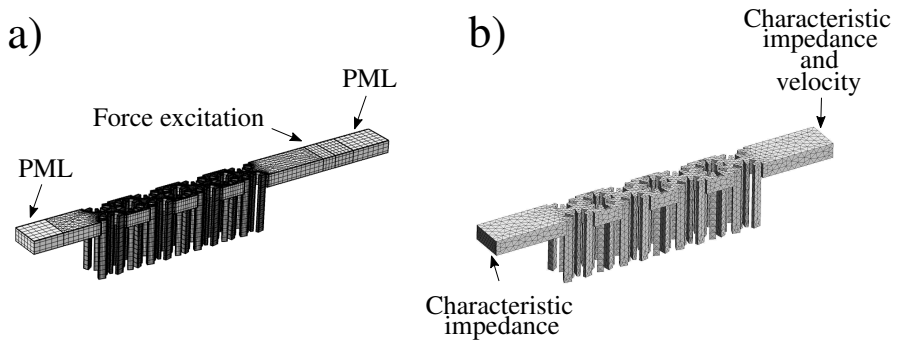

Figure 3.3: The geometry of the metamaterial studied in Paper A. Here, a) is the FEM mesh with corresponding boundary conditions and b) is the BEM mesh with corresponding boundary conditions.

With the help of viscothermal FEM and BEM simulations, Paper A investiges the trans-

mittance through the metamaterial. Fig. 3.3 shows the FEM and the BEM setup of the metamaterial including boundary conditions. Good agreement between lossy transmission simulations and measurements are found, confirming the hypothesis that losses are in fact preventing the metamaterial from working as intended.

3.6 Cloak based on scattering cancellation (Paper B)

Paper B investigates the effect of losses on an existing acoustic cloak presented by García-Chocano in Ref. [79]. Acoustic cloaks are devices that can effectively hide an object, so that sound waves in the neighbourhood of the object seem unaffected. In this case, the object is a large cylinder subject to an incoming plane propagating wave. In Ref. [79], a genetic optimization approach is used to locate 120 small cylinders around the large cylinder in such a way that scattering is minimized. As a result, incident plane waves near 3kHz are not disturbed by the object. In Ref. [79] some discrepancies between isentropic FEM simulations and measurements are observed; therefore, it has been of interest to investigate how much viscous and thermal losses influence this type of cloak.

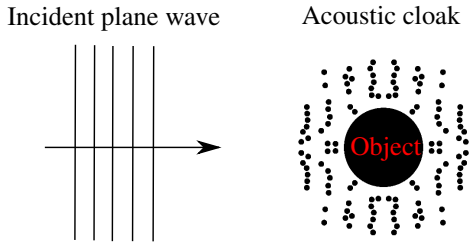

Figure 3.4: The geometry of the acoustic cloak studied in Paper B and the incident plane wave. By proper distribution of 120 small cylinders the large cylindrical object is effectively hidden and propagation of the plane wave appears unaffected.

The averaged visibility (a measure of how well the object is hidden) is used to validate the performance of the cloak. In general, it is shown that losses have very little impact on the average visibility, but some attenuating effects can be observed both due to the cloak but also due to the finite hight of the waveguide in which the cloak is placed. It is noted that discrepancies between simulations and measurements are mainly due to the experimental setup, where it is difficult to achieve an ideal plane wave.

3.7 Contribution

In Paper A, losses are proven to have a significant influence on the performance of the metamaterial. The performance degradation ultimately leads to a metamaterial without the desired properties. Apart from the investigation of losses, the metamaterial has served as a benchmark case to validate the three-dimensional viscothermal BEM implementation. The benchmark is challenging, and while there is good agreement between simulations and measurements, it is far from an exact match, and deviations between the FEM and BEM simulated transmittance are observed. However, it should be noted that the FEM and the BEM simulations uses different boundary conditions, which might lead to some of the observed differences.

On the contrary, Paper B shows that the performance of the cloak is not influenced by losses. However, this is not too surprising since the cloak does not contain narrow gaps and resonators.

The intention is that Paper A and Paper B can concribute to an increasing awareness of acoustic viscothermal losses in novel acoustic devices and establish some basic guidelines for when losses cannot be neglected.

Chapter 4

Improving the BEM implementation with losses

In the previous chapter, the BEM including viscothermal losses was presented, and potential shortcomings of the current implementation were identified. In this chapter, two new approaches are introduced which improve the previous implementation. In-depth theoretical development and validation of the proposed improvements are found in Paper C and Paper D. The focus of the papers is to find new solutions to the coupling of the discretized viscothermal BEM equations, and avoid the problematic finite difference coupling terms.

4.1 Tangential derivative BEM (Paper C)

Paper C presents a two-dimensional implementation of the viscothermal BEM, where the finite difference derivative matrices, $\mathbf{DT}_1$ and $\mathbf{DT}_2$, are removed and replaced by an additional set of tangential derivative boundary element equations used to estimate the derivatives of p_a, p_h, and $\vec{v}_v$. Tangential derivatives of these quantities are obtained by taking the tangential derivative of Eq. (2.7) at the collocation point, which leads to the boundary integral

$$C(P)\frac{\partial p(P)}{\partial \vec{t}(P)} = \int_\Gamma \frac{\partial^2 G(R)}{\partial \vec{t}(P)\partial \vec{n}(Q)} p(Q) d\Gamma(Q) - \int_\Gamma \frac{\partial G(R)}{\partial \vec{t}(P)} \frac{\partial p(Q)}{\partial \vec{n}(Q)} d\Gamma(Q) \tag{4.1}$$

where $\vec{t}$ is the tangential vector at the collocation point. Here, $\vec{t}$ should not be confused with time. The tangential vector and its location on the generator are sketched in Fig. 4.1. The tangential derivatives of the Greens functions are expressed as [80]

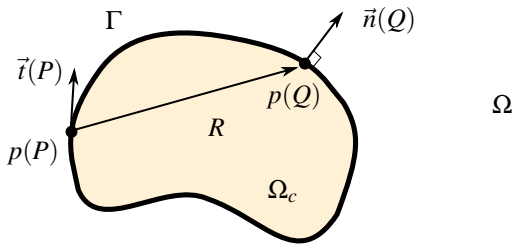

Figure 4.1: A sketch of the tangential derivative collocation BEM used to estimate tangential derivatives of boundary variables according to Eq. (4.1).

$$\frac{\partial G(R)}{\partial \vec{t}(P)} = \frac{ik}{2k} K_1(ikR) \frac{\partial R}{\partial \vec{t}} \tag{4.2}$$

$$\frac{\partial^2 G(R)}{\partial \vec{t}(P) \partial \vec{n}(Q)} = \frac{ik}{2\pi R} \left(K_1(ikR) \left(\vec{n} \cdot \vec{t} \right) - (2K_1(ikR) + ikRK_0(ikR)) \frac{\partial R}{\partial \vec{n}} \frac{\partial R}{\partial \vec{t}} \right), \tag{4.3}$$

if the domain is assumed to be two-dimensional. The second integral in Eq. (4.1) is of the Cauchy principal value (CPV) type. Usually, CPV integrals require careful treatment to be evaluated accurately. Yang [81], for example, proposes a substration-addition technique for their evaluation. However, in Paper C the integrals are evaluated using an adaptive integration scheme. Results show that this is a feasible procedure for their evaluation, but more appropriate kernel regularization techniques might yield better results. Based on Eq. (4.1), it is possible to establish a set of discretized equations relating p_a, p_h and $\vec{v}_v$ to their corresponding tangential derivatives:

$$\mathbf{C} \frac{\partial \mathbf{p}_a}{\partial \vec{t}} = \mathbf{A}_{a,t} \mathbf{p}_a - \mathbf{B}_{a,t} \frac{\partial \mathbf{p}_a}{\partial \vec{n}} \tag{4.4}$$

$$\mathbf{C} \frac{\partial \mathbf{p}_h}{\partial \vec{t}} = \mathbf{A}_{h,t} \mathbf{p}_h - \mathbf{B}_{h,t} \frac{\partial \mathbf{p}_h}{\partial \vec{n}} \tag{4.5}$$

$$\mathbf{C} \frac{\partial \mathbf{v}_{v,x}}{\partial \vec{t}} = \mathbf{A}_{v,t} \mathbf{v}_{v,x} - \mathbf{B}_{v,t} \frac{\partial \mathbf{v}_{v,x}}{\partial \vec{n}} \tag{4.6}$$

$$\mathbf{C} \frac{\partial \mathbf{v}_{v,y}}{\partial \vec{t}} = \mathbf{A}_{v,t} \mathbf{v}_{v,y} - \mathbf{B}_{v,t} \frac{\partial \mathbf{v}_{v,y}}{\partial \vec{n}} \tag{4.7}$$

where the subscript t denotes that the matrix is created by taking the tangential derivative of the integration kernel. Eqs. (4.4)-(4.7) can be used to fulfill the boundary conditions and ensure null-divergence of the viscous velocity, e.i. $\nabla \cdot \vec{v}_v = 0$.

4.1.1 System of equations

The derivation and resulting system of equations in Paper C has many similarities to the previous BEM formulation by Cutanda Henríquez. The system is derived through Schur complement operations, and it only considers acoustic pressure and boundary velocity variables as unknowns. A limitation of this type of formulation is that temperature boundary conditions are not easily accessible. In other words, boundaries are always assumed to be isothermal, which restricts the class of problems that the method is directly capable of solving. On the other hand, it should be possible to develop other configurations of the final system with access to the boundary temperature. Nevertheless, the system of equations as presented in Paper C is applicable to a broad range of acoustic problems where boundaries are assumed to be isothermal.

The main difference from the previous implementation is the way the BEM itself is used to estimate the tangential derivatives of p_a, p_h, $\vec{v}_v$. As a result, the new implementation completely avoids finite difference tangential derivatives, but also excludes the use of second-order tangential derivatives. It should be noted that the proposed implementation requires a full assembly of an additional set of matrices, making the method less efficient.

4.1.2 Unique normal and tangential vectors

Eq. (4.1) requires that the tangential vector is uniquely defined at the collocation point, meaning that the collocation point needs to be C^1-continuous. As previously discussed in Section 3.4.2, this requirement is not fulfilled with continuous Lagrange boundary elements. To make the vectors at the collocation point unique, Paper C utilizes discontinuous boundary elements. Discontinous boundary elements are elements that are not continuous at element interfaces, but allows for any order of continuity at the collocation point (depending on the element order). Additionally, they are known to be advantageous over continuous boundary elements [82]. More specifically, Paper C uses quadratic discontinuous boundary elements with the shape functions defined as [83]

$$N_1 = \frac{1}{2\eta^2}\xi\left(\xi - \eta\right) \tag{4.8}$$

$$N_2 = \frac{1}{\eta^2}\left(\eta - \xi\right)\left(\eta + \xi\right) \tag{4.9}$$

$$N_3 = \frac{1}{2\eta^2}\xi\left(\xi + \eta\right). \tag{4.10}$$

In Eqs. (4.8)-(4.10), the local coordinate ξ is defined on a reference element with $[-1 \leq \xi \leq 1]$ and $\eta = 1 - \alpha$, where α is a variable that determines the location of the nodes in the reference element. The use an equidistant distribution of nodes is suggested in Ref. [83], meaning that $\alpha = \frac{1}{3}$. Therefore, the equidistant distribution of the nodes is adopted in Paper C. When using discontinuous elements, the geometry is disctretized with regular quadratic continuous elements and only p_a, p_h and $\vec{v}_v$ are described through the discontinous shape functions.

Other examples exist of discretization methods that can achieve C^1-continuity at the collocation point, e.g cubic splines [84] or Overhauser elements [85, 86, 87]. However, such elements are cumbersome to implement in comparison to the discontinuous elements.

4.1.3 Evaluation of the formulation

In Paper C, the new tangential derivative BEM (TD-BEM) implementation is validated through two numerical test cases and compared with the previous finite difference implementation (FDD-BEM).

The first test case is a convergence study using an analytical description of an infinite oscillating cylinder in a viscous fluid as a reference [88]. In Fig. 4.2, the convergence study found in Paper C of the infinite oscillating cylinder is reproduced. Convergence is carried out at 25 Hz and 50 Hz.

The second test case studies wave propagation in a narrow slit. The narrow slit test case contains boundary layers that tend to fill the setup, making it more challenging. It also shows the robustness of the TD-BEM when the mesh is irregular. Here, viscothermal COMSOL FLNS FEM simulations are used for comparison.

4.2 Shape function derivatives (Paper D)

Paper D suggests a different approach to remove of the finite difference matrices. First, it should be noted that in this case the derivations are performed assuming three dimensions, so the tangential derivative is expressed through two surface tangential vectors. In Paper D, the tangential derivatives are estimated by using the shape functions directly. This is accomplished by a translation from the global (x,y,z) coordinate system into a local node-related coordinate system described by the normal and tangential vectors (n,t_1,t_2). In this way the tangential derivatives at specific nodes can be estimated

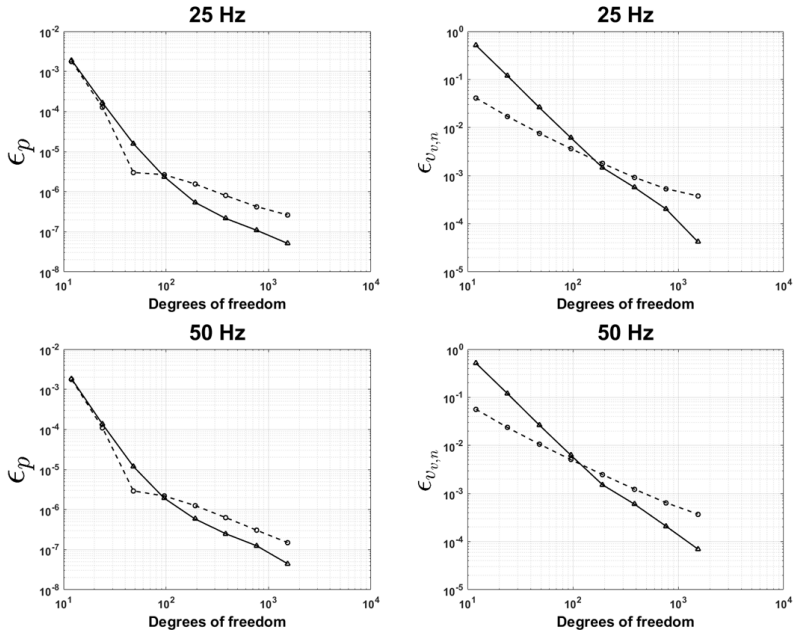

Figure 4.2: Convergence plots at 25 and 50 Hz of the BEM formulations with losses for the case of an infinite oscillating cylinder. Both pressure and normal viscous velocity error are plotted for TD-BEM (solid) and FDD-BEM (dashed).

from the shape functions. Regular continuous elements are used in the implementation, meaning that the tangential derivatives, the normal vector and the tangential vectors need to be calculated as an average at element interfaces. As a benefit, the derivation only requires evaluation of the tangential derivative of the acoustic pressure and the viscous velocity. The formulation is named the shape function derivative BEM (SFD-BEM).

4.2.1 System of equations

As previously, the system of equations is derived by Schur complement operations, but in this case the viscous velocity is included as a depended variable in the resulting

system of equations. The final form is given by

$$\mathbf{S}\begin{bmatrix}\mathbf{p}_a\\ \mathbf{v}_{v,x}\\ \mathbf{v}_{v,y}\\ \mathbf{v}_{v,z}\end{bmatrix} = \begin{bmatrix}\mathbf{v}_{b,n}\\ \mathbf{0}\\ \mathbf{v}_{b,t_1}\\ \mathbf{v}_{b,t_2}\end{bmatrix} \tag{4.11}$$

where the matrix $\mathbf{S}$ is a combination of the acoustic, thermal and viscous matrices. In Paper D, this system type is referred to as an expanded system. To isolate and study the effect of the expanded system, an alternative expanded version of the FDD-BEM is also investigated. It is denoted as the FDD2-BEM.

4.2.2 Evaluation of the formulation

In Paper D, the new formulation is evaluated through two test cases. In the first test case, an analytical solution of an oscillating sphere [89, p. 435] is used to compare the accuracy of SFD-BEM, FDD-BEM and FDD2-BEM. In the second test case, the response of a condenser microphone is calculated and the three different formulations are compared with existing measurements.

4.3 Contribution

In Paper C, the main contribution is the way that tangential derivative BEM is used to avoid the finite difference coupling terms in the existing two-dimensional viscothermal BEM. The paper also suggests the use of discontinuous boundary elements to remove the unnecessary averaging of the normal and tangential vectors at element interfaces, which is new for the viscothermal BEM but not for BEM in general. Through two test cases, it is demonstrated that the new implementation facilitates improved stability for irregular meshes and reduced errors at high mesh densities. However, convergence studies also reveal that low mesh densities might lead to larger errors in the viscous velocity computation. The low mesh density error and its impact on other computational examples will require more elaborate studies over what is presented in Paper C.

With a different approach, Paper D removes the finite difference matrices from the three-dimensional viscothermal BEM implementation, by utilising the shape functions to estimate the tangential derivatives of the acoustic pressure and viscous velocity. In comparison to the two-dimensional implementation, the calculation of the tangential pressure and viscous velocity derivatives with finite difference in three dimensions is very cumbersome. Paper D demonstrates that the shape function approach leads to

a significantly more accurate and stable solution. However, the implementation still relies on continuous Lagrange interpolated elements where the normal and tangential vectors are averaged at element interfaces. Discontinuous elements are proposed as a future improvement.

Chapter 5

Acoustic shape optimization including losses

Optimization relying on numerical methods has gained an increasing interest due to the possibility of improving the design, the performance or to find new solutions to problems in engineering. This has become achievable through the evolution of more powerful computers and the possibility of combining numerical computations with optimization algorithms.

Optimization can be categorized by either parameter, shape or topology optimization. Topology optimization in particular, has gained much attention during the last decade, in part due to its ability to find completely new and surprising designs, but also because additive manufacturing processes have made the realization of such complicated designs possible. However, from a viscothermal acoustic perspective, topology optimization has some disadvantages. The discretization in the entire design domain needs to resolve the boundary layers, thus making it very computationally demanding. As an alternative, the focus of the presented work is showing the applicability of the viscothermal BEM in combination with shape optimization, and use it to optimize viscothermal acoustic problems.

We will now continue with an introduction to general optimization methods and shape optimization. This is followed by a section summarizing Paper E. In Paper E, the viscothermal BEM is combined with shape optimization to optimize the absorption of an impedance termination. Additionally, some unpublished isentropic shape optimization results are shown utilizing the previous presented acoustic cloaking device as an example.

5.1 Optimization problem

When performing optimization, an adequate measure of the performance of the specific problem is necessary. In optimization, such measure is usually called an objective function. The objective function is used by the optimization algorithm to determine how a specific design variable needs to change to improve the design. In general, the way that a design change affects the objective function is described by the governing equations. In optimization, these equations are denoted as the state equations. In an acoustic context, the state equation would be the isentropic wave equation, or the FLNS equations if losses are to be considered.

A constrained shape optimization problem can be expressed as

$$\begin{aligned} \underset{\mathbf{v}}{\text{minimize:}} \quad & \phi(\mathbf{v}) \\ \text{subject to} \quad & F(\mathbf{v}) = 0 \\ & \mathbf{a}(\mathbf{v}) \leq 0 \\ & \mathbf{b}(\mathbf{v}) = 0 \end{aligned} \tag{5.1}$$

where $\phi(\mathbf{v})$ is the objective function, which depends on the design variables $\mathbf{v}$. In shape optimization, the vector $\mathbf{v}$ will determine the shape of the boundary and $F(\mathbf{v})$ is the state equation. Additionally, the optimization problem can be constrained by the equality constraint $\mathbf{b}(\mathbf{v})$ and the inequality constraint $\mathbf{a}(\mathbf{v})$.

5.2 Gradient-based optimization

Paper E performs shape optimization relying on an iterative gradient-based optimization approach. In gradient-based optimization, gradient information, and sometimes the Hessian of the objective function, is used to search for minima of the objective function. Usually, gradient-based optimization will lead to some local minimum, meaning that an optimal solution most often cannot be guaranteed. In most engineering situations, local minima are considered sufficient for improving and developing new designs. One of the simplest gradient-based optimization algorithms is the steepest decent. However, other more elaborate and efficient gradient-based optimization algorithms exist such as the Method of Moving Asymptotes, Sequential Linear and Quadratic Programming, Interior Point Methods and Quasi-Newton Methods. In the following shape optimization examples, the Sequential Quadratic Programming (SQP) method found in the MATLAB function *fmincon* is used [90]. For an introduction to the aforementioned methods consult, e.g. Ref. [91].

Besides gradient-based optimization, other optimization methods exist such as evolutionary and genetic algorithms. For engineering purposes, they are usually considered too inefficient, especially if the problem consists of a large amount of design variables [92]. Nevertheless, evolutionary and genetic algorithms have also been applied to acoustic shape optimization problems [93, 94, 95, 96].

5.3 Shape optimization and parametrization

Shape optimization and its application in engineering can be found in a vast variety of disciplines, ranging from fluid mechanics [97] to electromagnetics [98], as well as in acoustics [99].

In shape optimization, the choice of boundary parametrization is important, since it will restrict the possible shapes of the boundary and limit the design freedom. In Paper E, cubic splines are used to represent the boundary shape. Cubic splines were chosen because it is a simple way of achieving some boundary regularization. Additionally, it also allows for the calculation of the boundary curvature, which is used as a constraint. On the other hand, the boundary is not able to form sharp features like corners and edges. Similarly, the boundary could also be represented with polynomials or other types of splines. During this project, Bézier curves, for example, have also been tested and used.

Another more direct approach is to manipulate the position of the nodes in the mesh directly. This has some advantages in terms of the design freedom. However, it will require some sort of boundary regularization relying on, e.g. filtering techniques. Regularization is necessary to avoid large numerical errors that can occur if the nodes are distorted too much. Additionally, this approach will lead to more design variables compared to a parametrization utilizing splines or polynomials.

A survey including the parametrization approaches presented here and other methods are given in the work by Samareh [100].

5.4 Sensitivity analysis

Sensitivity analysis is the process of finding the gradients of the objective function with respect to the design variables. In other words, it is a measure of how the objective

function is influenced by a change in the boundary shape. The gradient information is then used by the optimization algorithm to minimize or maximize the objective function. This means that the gradients should be calculated as efficiently and accurately as possible to improve the overall optimization time. In the BEM, the sensitivity analysis is usually carried out working on the continuous equations using direct differentiation [101, 102, 103] or an adjoint method [104, 105, 106].

However, no existing literature contains examples of direct differentiation or adjoint methods for the estimation of sensitivities in the case of the viscothermal BEM. During the last part of this PhD project, a considerable amount of work has been put into the development of an adjoint method capable of calculating viscothermal BEM sensitives. Unfortunately, due to time limitations, no completely developed and tested formulation exists. Therefore, sensitivities in Paper E are obtained using the less efficient forward finite difference scheme

$$\frac{\partial \phi}{\partial v_i} = \frac{\phi(\mathbf{v} + \Delta v_i \cdot \mathbf{e}_i) - \phi(\mathbf{v})}{\Delta v_i}, \tag{5.2}$$

where v_i is a single design variable, $\mathbf{e}_i$ is a unit vector for the i-th variable and Δv_i is the step length. To achieve some additional optimization speed, the sensitivities are calculated in parallel using the *UseParallel* option in *fmincon*.

5.5 Sparse assembly

Additional computational speed of the viscothermal BEM simulations is achieved by a concept here called sparse assembly. The BEM matrices are by default fully populated and dense. However, in the assembly of the viscous and thermal matrices, most of the integrals do not contribute to the construction of the matrices. In fact, element integration only contributes to the viscous and thermal matrices when the distance to the collocation point is comparable with the boundary layer thickness. Therefore, as a criterion in the assembly routine of the matrices, integration is only carried out when the distance between the element and the collocation point is below twenty times the boundary layer thickness. Fig. 5.1 depicts the concept of sparse assembly where $\delta_{lim} = 20\delta_v$ is the threshold that determines if integration is to be carried out. Therefore, integration is only performed if $R < \delta_{lim}$ or when the collocation point is on the element. Sparse assembly makes the assembly of the viscous and thermal matrices about an order of magnitude faster.

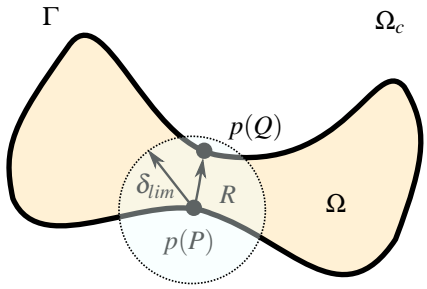

Figure 5.1: An illustration of the sparse assembly approach used in Paper E. To improve the assembly speed of the viscous and thermal matrices, integration is only carried out when $R < \delta_{lim}$. This avoids the calculation of integrals that do not contribute to the viscous and thermal matrices.

5.6 Constraints

In the shape optimization technique developed in Paper E, the goal is to increase the design freedom and the realizable shapes. This is achieved by allowing the xy-coordinates of the cubic spline control points to move freely. As a consequence, the boundaries can overlap and create non-physical designs. Since non-physical designs are not desirable, two sets of inequality constraints are used to only allow meaningful shapes. The first constraint limits the allowed curvature at the control points. The curvature constraint is defined by

$$\boldsymbol{\kappa}(\mathbf{v}) - \kappa_{max} \leq 0 \tag{5.3}$$

with $\boldsymbol{\kappa}(\mathbf{v})$ being a vector containing the curvature at each control point and κ_{max} being the maximum allowed curvature. The boundary curvature constraint for a single control point is depicted in Fig. 5.2a. Since the parametrization is based on cubic splines, the curvature at the i-th control point is obtained by

$$\kappa_j = \frac{|x'(t)y''(t) - y(t)'x(t)''|}{(x'(t)^2 + y'(t)^2)^{3/2}} \tag{5.4}$$

where x and y are the coordinates of the i-th control point as a function of the cubic spline parameter $t \in [0,1]$ and the primes denotes the derivative with respect to t.

The second inequality constraint is a combination of a distance and self-intersection

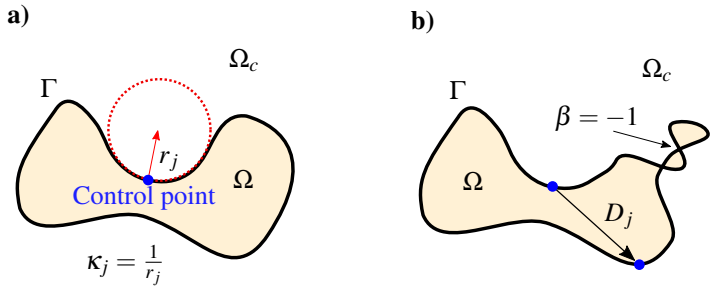

Figure 5.2: Illustration of the two types of constraints used in Paper E. Figure a) illustrates the curvature constraint where κ_j is the curvature at the j-th control point. Geometrically the curvature can be described from the red circle which is the best approximation of the curve at the control point. The curvature is defined as the inverse of the circle radius r_j. Figure b) shows the distance constraint where D_j is the distance between individual control points and β is a parameter that is -1 if the boundary self-intersects and 1 otherwise.

constraint, defined as

$$D_{min} - \beta \mathbf{D}(\mathbf{v}) \leq 0. \tag{5.5}$$

In Eq. (5.5), the vector $\mathbf{D}(\mathbf{v})$ contains the distances between all the control points and D_{min} specifies the minimum distance allowed. Additionally, the parameter β is equal to -1 if the boundary self-intersect and 1 if the design is meaningful and does not contain any overlapping boundaries. Fig. 5.2b shows the case where the design is non-physical and $\beta = -1$. Using the proposed constraints comes at a computational cost and requires calculation of the curvature, the distance between control points and the detection of boundary self-intersection at each iteration during optimization.

5.7 Shape optimization including losses (Paper E)

Paper E demonstrates the applicability of the viscothermal BEM in combination with shape optimization and investigates how acoustic losses can impact shape optimization. As an example, an impedance tube represented by a two-dimensional domain is used as a test case. At the termination of the impedance tube, either four quarter-wave or Helmholtz resonators are located. Fig. 5.3 depicts the initial parametrization of the two resonator types using cubic splines to represent their shape. The resonators are described symmetrically so only the upper boundary of a single resonator is parametrized. The shape of the resonators is controlled by changing the location of the control points illustrated by blue dots in Fig. 5.3. All resonators use the same parametrization, mean-

ing that the shape of the four resonators is the same. However, they are allowed to individually scale 10% in length as an additional design variable.

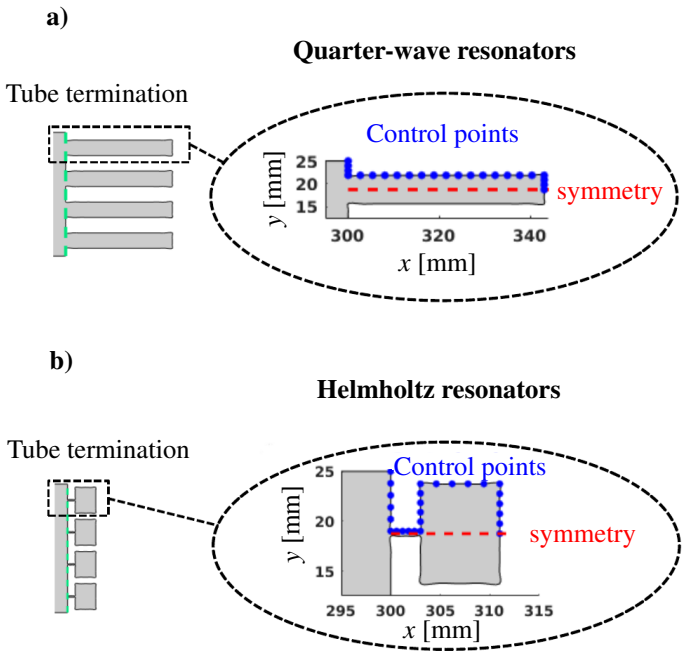

Figure 5.3: The initial parametrization of the impedance tube termination. The two resonator types used are a) quarter-wave resonators and b) Helmholtz resonators. At the left-hand side of a) and b), the full design is shown. The parametrization of a single resonator is magnified, showing the initial locations of the control points (blue dots) that determine the shape of the resonators. The control points define the cubic spline interpolation.

5.7.1 Optimization problem

The objective of the optimization problem in Paper E is to maximize the absorbing capabilities of the resonators by changing their shape. Thus, the objective function is defined as the absorption coefficient of the resonators located at the impedance termination. The absorption coefficient is estimated in Paper E using the transfer function method [107].

Two different objective functions are defined to compare and investigate the effect of losses. The first objective function is calculated using the viscothermal BEM and denoted ϕ_{VT}. The second objective function is called ϕ_{LL} and is obtained using lossless BEM. Designs can hereby be optimized based on either a lossy or lossless assumption. In general, the absorption coefficient will range from 0 to 1, corresponding to null or maximum absorption, respectively.

5.7.2 Summery of shape optimization results

Several numerical optimization experiments are performed to evaluate the influence of losses on the shape optimized quarter-wave and Helmholtz resonators. The optimization results and different studies are summarized in the following:

- The first study is a comparison of the quarter-wave resonators optimized at a single-frequency either with or without losses. The study includes an investigation of the absorption coefficient as a function of frequency for the optimized designs. Here it is interesting to note that lossless optimization results in ϕ_{LL} = 1, thus full absorption is achieved using a formulation without losses. The reason for this is a peculiar phenomenon in the BEM called numerical damping. Numerical damping acts as artificial losses, and is utilized by the optimizer to obtain a design that seemingly fully absorbs the sound wave. The discussed here designs are reproduced in Fig. 5.4. In the figure, it is observed that as soon as losses are introduced, the performance of the lossless design is degraded.

- A second study performs multi-frequency optimization of the quarter-wave resonators with the objective function defined as the sum of the absorption coefficients at 3 frequencies. As a result, it is possible to broaden the frequency range and still achieve high absorption.

- In a third study, shape optimization of the quarter-wave resonators is performed assuming that losses can be described through a bulk loss. This method is often employed in the literature [108]. Losses are introduced into the isentropic BEM through a complex wave number defined as $k_B = k_{LL} - i\tau_s$, with k_{LL} being the lossless wavenumber and τ_s being a variable that determines the amount of bulk loss. Optimization experiments sweeping the value of τ_s show that it is difficult to choose an appropriate value of τ_s that yields a design with high absorption.

- The last study is single-frequency optimization of the Helmholtz resonators with and without losses. Here, it is found that the design of the Helmholtz resonators

based on lossy optimization yields the best performance, and the absorption capabilities of the lossless optimized design is even worse when compared to the initial design.

In all the numerical experiments presented in Paper E, it is found that for this particular optimization problem, designs created including viscous and thermal losses yield the best performance.

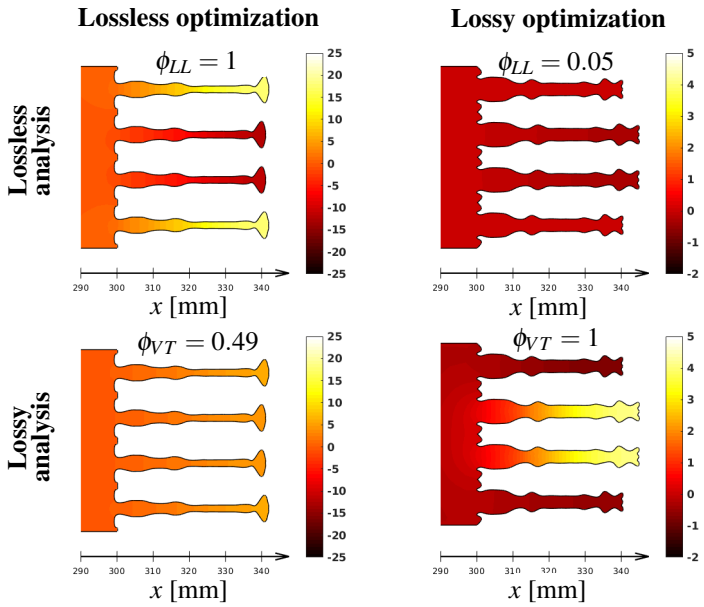

Figure 5.4: Comparison (crosscheck) of the lossless and lossy optimized designs of the impedance tube termination reproduced from Paper E. Here, ϕ_{LL} and ϕ_{VT} are the lossless and lossy objective functions calculated for the two designs. The initial design consists of simple quarter wave resonators controlled using a cubic spline representation of the boundary as depicted in Fig. 5.3a. The plotted field variable is the real part of the pressure in Pascal.

5.8 Shape optimization of an acoustic cloak

In Paper B, an existing acoustic cloaking design was investigated with the conclusion that losses are negligible. The particular cloak used 120 small cylinders to achieve high performance in terms of a low averaged visibility. We will demonstrate here how the shape optimization technique proposed in this chapter can also be utilized in optimizing devices like the acoustic cloak. Since losses are negligible, optimization is carried out using isentropic BEM. In this case, 16 small cylinders are located around the object. Four of the cylinders acts as reference cylinders parametrized using cubic splines, and the remaining cylinders follow the shape of the reference cylinders symmetrically. By minimizing the total scattered pressure field surrounding the cloak, a design is created with similar properties as the design consisting of 120 cylinders. Fig. 5.5 shows the initial design and the optimized design. The figure also includes field pressure calculations showing how the optimized cloaking design reconstructs the field into an undisturbed plane propagating wave.

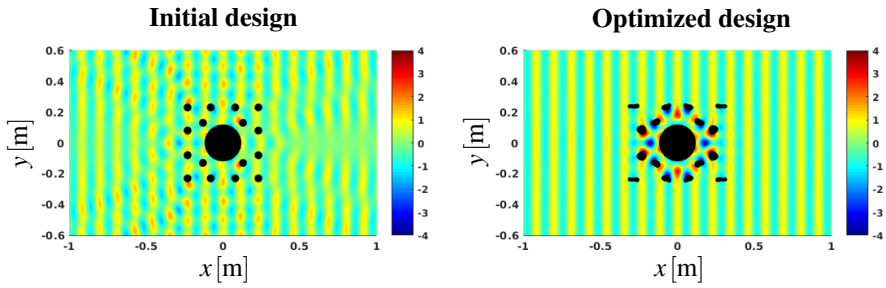

Figure 5.5: Shape optimization of an acoustic cloaking device. On the left, the initial design consisting of 16 small cylinder parametrized using cubic splines. On the right, the optimized cloak. The colormap in both plots represents the real part of the pressure.

To validate the performance of the shape optimized cloak, the average visibility is compared with the existing cloak consisting of 120 cylinders. The average visibility for the two designs is plotted in Fig. 5.6. It is shown that the shape optimized cloak achieves almost the same performance as the existing cloak. However, the shape optimized cloak achieves the desirable low visibility with much fewer scatters.

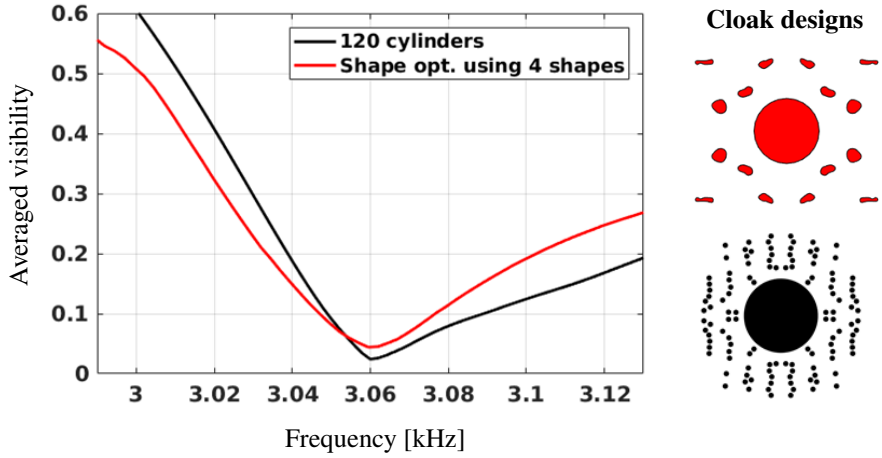

Figure 5.6: A comparison of the two cloaking designs. On the left, the average visibility of the two designs. The black curve is the visibility of the cloak from Ref [79] consisting of 120 cylinders and the red curve is the visibility of the shape optimized cloak. On the right, the two cloak designs. The red coloured cloak is optimized using shape optimization and the design of the black coloured cloak is taken from Ref. [79].

5.9 Contribution

Paper E is among the first publications to discuss how acoustic viscous and thermal losses can affect optimization. Furthermore, the combination of viscothermal BEM and shape optimization is new. This combination is attractive because viscothermal BEM avoids domain meshes and can handle complex domains with overlapping boundary layers. From a shape optimization perspective, the fact that domain meshes and boundary layer meshes can be avoided makes the optimization implementation simple and it is possible to circumvent, for example, re-meshing during optimization.

Several steps have been taken to improve the optimization time and hence the usability of the proposed shape optimization technique. One approach is the sparse assembly method that enhances the assembly speed of the viscous and thermal matrices another is the implementation of the two-dimensional BEM assembly routine into compiled C++/MEX , which has contributed with increased optimization speed.

In Paper E, results show that viscous and thermal dissipation can have a significant impact on the performance of the shape optimized resonators. However, the effect of losses depends on the problem. In other cases, the extra effort of including losses might not be necessary. As an example, viscothermal losses have very little influence on the acoustic cloaking device and can be shape optimized with regular isentropic BEM as in Section 5.8.

Chapter 6

Discussion and conclusions

The PhD thesis has treated three different subjects related to acoustic viscous and thermal dissipation; namely, an investigation of the effect of acoustic losses on two novel acoustic devices, improving an existing viscothermal BEM implementation and the development of a shape optimization technique based on the viscothermal BEM.

Modelling of two novel acoustic devices

Including viscous and thermal dissipation into numerical acoustic simulations based on the FLNS equations comes at a significant computational cost. Therefore, if possible, it is desirable to simplify the problem using isentropic assumptions. In some cases, this requires a profound understanding of the given problem to decide on the suitable modelling strategy. As an example, Paper A presents a metamaterial developed under the assumptions that the acoustic wave behaviour can be considered lossless. This assumption leads to an analytically and numerically designed metamaterial that exhibits double negative behaviour using the combined effect of periodically distributed scatterers and quarter-wave resonators. Unfortunately, measurements in Ref. [78] and lossy numerical FEM and BEM simulations in Paper A reveal that viscothermal losses negatively impacts the performance of the metamaterial, making the initially proposed design lose its double-negative band. A similar comparison is made in Paper B where numerical experiments investigate the effect of losses on an acoustic cloaking device based on scattering cancellation. In this type of device, it is found that losses can be considered negligible, and the isentropic assumption is sufficient to give an accurate estimate of the cloaking performance. The main difference between the two types of devices is the fact that the metamaterial utilizes quarter-wave resonators to obtain the desired effects. The quarter-wave resonators, and other resonators for that matter, will in most cases contribute with a considerable amount of loss.

The metamaterial simulations has served as a good benchmark to show the capabilities of the viscothermal BEM and its applicability to solve complicated large problems.

While not used in this project, the SLNS FEM implementation is an alternative to the FLNS FEM and could be used to more efficiently simulate the metamaterial in a FEM framework. In situations where it is not directly apparent that losses can play an important role, i.e. the geometry is far from having overlapping boundary layers, computationally cheaper methods like the BLI models are very interesting, since they would allow for a cheap estimation of how losses influence a given problem. Additionally, the BLI formulation should also be suitable for implementation into the BEM framework used here.

Improving the viscothermal BEM

A potential shortcoming of the previous viscothermal BEM is the use of first and second order finite difference coupling terms to estimate tangential derivatives of the acoustic pressure. The use of finite difference is prone to some error and is cumbersome to implement in three dimensions. This is addressed in Paper C and Paper D, where two new coupling strategies are discussed which improve on the existing implementation by removing the use of finite difference.

The first approach is TD-BEM which uses the boundary element itself to estimate the tangential derivatives by an additional set of two-dimensional tangential derivative boundary element equations. As a result, only first order tangential derivative calculations are necessary. Moreover, the previous implementation relies on an averaging of the normal and tangential vectors at the element interfaces. In the TD-BEM implementation, the averaging is avoided by using discontinuous elements where the normal and tangential vectors are uniquely defined at the collocation points. The approach is evaluated and compared with the previous implementation through two simple test cases. The first test case is a convergence study using an analytical solution of an oscillating cylinder as a reference (Fig. 4.2). It is found that higher mesh densities seem to favour the TD-BEM with slightly lower errors in the pressure and viscous velocity calculation. On the other hand, the viscous velocity is found to have larger errors at low mesh densities. It is not fully understood why this is the case, but it might be that the estimation of the tangential derivatives of the rapid decaying viscous velocity using boundary element itself requires a better mesh resolution. A plausible solution would be to use a coarse pressure mesh and a more refined mesh describing the viscous velocity. However, such implementation would come at an increased computational cost. Nevertheless, it should be noted that the lowest mesh densities corresponds to very coarse meshes, considered insufficient in general. The second test case is a narrow

duct, which highlights some of the potential issues with the FDD-BEM and demonstrates the strength of TD-BEM. It is shown that the FDD-BEM is very sensitive to irregular element sizes which can lead to a larger error. The same instability issue is not observed when using TD-BEM. Computationally, the TD-BEM has some disadvantages since the method requires an assembly of an additional set of tangential derivative BEM matrices.

The second approach, SFD-BEM, directly uses the shape functions to estimate the tangential derivatives. The result is an expanded system of equations where both the acoustic pressure and viscous velocity becomes dependent variables. In Paper D, the SFD-BEM concept is implemented into a three-dimensional formulation and tested through two test cases: an oscillating sphere and a condenser microphone. It is shown that the SFD-BEM is an improvement over the previous finite difference implementation with better stability and reduced errors. Notably is the calculation of the viscous velocity which is significantly better. It should be noted, that the use of finite difference in three-dimensions is more problematic and prone to considerably larger errors as compared to two dimensions. SFD-BEM, as presented in Paper D, relies on continuous elements which require averaging of both the normal and tangential vectors at element interfaces, but also the tangential derivatives. However, the averaging can be avoided by using the aforementioned discontinuous elements. Additionally, since the approach relies on the shape functions to estimate the tangential derivatives, the tangential derivative will always become one order lower than the element order. Therefore, higher order elements are a requirement. In Paper D, isoparametric continuous quadratic elements are used, meaning that the description of the tangential derivative is linear. As a benefit over the TD-BEM, the SFD-BEM only requires assembly of the acoustic, thermal and viscous matrices. In the BEM implementation, most of the time is spent on the assembly of matrices, making the SFD-BEM faster as compared to TD-BEM.

In this project, much effort is given towards solutions that match the boundary conditions described in a local node-related coordinate system. In other words, the no-slip condition is described in terms of its normal an tangential components using Eq (3.20) and Eq. (3.21). During this project another possibility was considered but not implemented due to time limitations: fulfilling the boundary conditions using a Cartesian description of the no-slip condition, i.e. Eq. (3.19). As an example, the gradients of p_a and p_h can be found by taking the Cartesian derivative of the Kirchoff-Helmholtz integral. This approach would in theory avoid the necessary translation using the Hadamard product. On the other hand, such method would require integration of hypersingular kernels. Another idea is to solve and fulfil the boundary conditions using

some kind of iterative approach.

Acoustic shape optimization with losses

In Paper E, a two-dimensional shape optimization technique based on the SFD-BEM that includes modelling of acoustic viscous and thermal dissipation is developed. The technique is applied to maximize the absorption coefficient of quarter-wave and Helmholtz resonators located at an impedance tube termination. A series of numerical experiments investigate the role of losses when performing shape optimization. For the particular test cases, it is found that losses play a significant role and near perfect absorption can only be obtained if losses are included.

During the development and testing of the shape optimization technique multiple test cases have been studied which are not included in this thesis. The primary goal has been to establish an awareness that losses can play an important role when performing optimization. The example chosen here, an impedance tube, is found to be a good benchmark for lossy optimization since it isolates the effect of losses. In fact, optimization can only be performed if the numerical model contains some loss, otherwise the absorption coefficient will always be equal to zero. In isentropic BEM, intrinsic numerical damping contributes with losses and makes shape optimization of the quarter-wave and Helmholtz resonators possible. It has been observed in some test cases that numerical damping contributes to the optimization by creating meaningful designs that sometimes are similar to what is obtained with the viscothermal BEM. A similar situation is seen in the optimization of the quarter-wave resonators, where the final lossless optimized design has some absorbing capabilities.

Another observation worth noting is that visothermal dissipation stabilizes the optimization process, and lossy optimization usually requires less iterations.

6.1 Conclusions

The most important conclusions from the papers can be summarized as follows:

- It is numerically verified in Paper A that acoustic dissipation is the reason why the metamaterial is not behaving as intended when measured.

- Paper B shows that losses have very little influence on the averaged visibility and the acoustic cloaking device performance in general.

- By utilizing either tangential derivative boundary element or the shape functions it is found possible in Paper C and Paper D to avoid the use of the tangential derivative finite difference coupling terms used in the previous viscothermal BEM implementations. The two new approaches demonstrate increased stability and error reduction.

- Paper E sussesfully implements a two-dimensional gradient-based shape optimization technique that is capable of including acoustic viscous and thermal dissipation. The technique is demonstrated by maximizing the absorption coefficient of quarter-wave and Helmholtz resonators. Shape optimization results confirm that accurate modelling of acoustic losses is necessary to obtain designs with nearly perfect absorption.

6.2 Future research

It is intended that the shape optimization technique developed in this thesis can be used to design and improve the performance of acoustic transducers and hearing aids, but also be applied to create new metamaterial designs where the effect of losses is included in the design process. The developed optimization technique seems promising; however, the thesis has only considered two-dimensional simple academic problems. Therefore, the extension into three dimensions is necessary to facilitate optimization of real-world problems. Such an extension would require a more efficient sensitivity analysis based on e.g. an adjoint method. Additionally, the work carried out here is purely numerical, and experimental validation should be performed to verify the usability of the proposed shape optimization technique. The realization of optimized designs would require the inclusion of manufacturing constraints and robustness measures in the optimization process. Another direction is to extend the shape optimization technique to account for the mechanical coupling which is important in, e.g. hearing aids.

As already briefly discussed, other directions for the viscothermal BEM implementation are possible, and methods to fulfil the boundary conditions differently or relying on iterative methods could be subject for further research. Moreover, more direct studies comparing viscothermal FEM and BEM models are necessary to give a better idea of the computational benefits of the BEM in large-scale computations. To do this on an equal footing, implementation of the three dimensional viscothermal BEM into more efficient languages like C++ or fortran is required.

Bibliography

[1] P. M. Morse and K. U. Ingard. *Theoretical acoustics*. McGraw-Hill, Inc, 1968.

[2] A. D Pierce. *Acoustics: An Introduction to Its Physical Principles and Applications*. Acoustical Society of America, 1991 (second printing).

[3] R. Christensen. *Acoustic Modeling of Hearing Aid Components*. PhD thesis, University of Southern Denmark, 2010.

[4] W. R. Kampinga. *Viscothermal acoustics using finite elements. Analysis tool for engineers*. PhD thesis, University of Twente, Enschede, 2010.

[5] P. Honzik, C. Guianvarc'h, and M. Bruneau. Modeling of capacitive mems microphone with square membrane or plate using integral method. *ELSEVIER SCIENCE BV*, 120:418–421, 2015. doi: 10.1016/j.proeng.2015.08.656.

[6] D. Homentcovschi, R. N. Miles, P. V. Loeppert, and A. J. Zuckerwar. A microacoustic analysis including viscosity and thermal conductivity to model the effect of the protective cap on the acoustic response of a mems microphone. *Microsystem Technologies-micro-and Nanosystems-information Storage and Processing Systems*, 20(2):265–272, 2014. doi: 10.1007/s00542-013-1800-5.

[7] V. Cutanda Henríquez. *Numerical transducer Modeling*. PhD thesis, Technical University of Denmark, Lyngby, 2002.

[8] M. J. H. Jensen and E. S. Olsen. Virtual prototyping of condenser microphones using the finite element method for detailed electric, mechanic, and acoustic characterization. volume 19, page 030039, 2013. doi: 10.1121/1.4799295.

[9] G. Plantier and M. Bruneau. Heat conduction effects on the acoustic response of a membrane separated by a very thin air film from a backing electrode. *Journal D'acoustique*, 3(3):243–50, 243–250, 1990.

[10] R. Christensen and U. Skov. Compression driver simulation incl. vibroacoustic, viscothermal & porous acoustics. In *Proceedings from the COMSOL conference in Stuttgart (Germany)*, 2011.

[11] R. Christensen and U. Skov. Simulation of a 4" compression driver using a fully coupled vibroacoustic finite element analysis including viscous and thermal losses. In *Audio Engineering Society Convention 132*, Apr 2012. URL http://www.aes.org/e-lib/browse.cfm?elib=16310.

[12] M. Berggren, A. Bernland, and D. Noreland. Acoustic boundary layers as boundary conditions. *Journal of Computational Physics*, 371:633–650, 2018. doi: 10.1016/j.jcp.2018.06.005.

[13] M. A. Temiz, I. L. Arteaga, and A. Hirschberg. Sound Absorption Measurements for Mirco-Perforated Plates: The Effect of Edge Profile. In *Proceedings from EURONOISE, 31 May - 3 June, Maarstrcih (Netherlands)*, 2015.

[14] J. Carbajo, J. Ramis, L. Godinho, P. Amado-Mendes, and J. Alba. A finite element model of perforated panel absorbers including viscothermal effects. *Applied Acoustics*, 90:1–8, 2015. doi: 10.1016/j.apacoust.2014.10.013.

[15] S. A. Cummer, J. Christensen, and A. Alù. Controlling sound with acoustic metamaterials. *Nature reviews materials*, 1:1–13, 2016. doi: doi:10.1038/natrevmats.2016.1.

[16] H. Ruiz, C. C. Claeys, E. Deckers, and W. Desmet. Numerical and experimental study of the effect of microslits on the normal absorption of structual metamaterials. *Mechanical Systems and Signal processing*, 70-71:909–918, 2016. doi: doi:10.1016/j.ymssp.2015.09.028.

[17] H. Ryoo and W. Jeon. Dual-frequency sound-absorbing metasurface based on viscothermal effects with frequency dependence. *Journal of Applied Physics*, 123:115110, 2018. doi: 10.1063/1.5017540.

[18] N. Jiménez, V. Romero-García, P. Pagneux, and J. Groby. Rainbow-trapping absorbers: Broadband, perfect and asymmetric sound absorption by subwavelength panels for transmission problems. *Scientific Reports*, 7(1):13595, 2017. doi: 10.1038/s41598-017-13706-4.

[19] M. Molerón, M. Serra-Garcia, and C. Daraio. Visco-thermal effects in acoustic metamaterials: from total transmission to total reflection and high absorption. *New J. Phys.*, 18:033003, 2016. doi: 10.1088/1367-2630/18/3/033003.

[20] E. Wadbro and M. Berggren. Topology optimization of an acoustic horn. *Comput. Methods Appl. Mech. Engrg.*, 196:420–436, 2006. doi: 10.1016/j.cma.2006.05.005.

[21] R. Udawalpola, E. Wasbro, and M. Berggren. Optimization of an acoustic horn with respect to efficientcy and directivity. *Int. J. Numer. Meth. Engng*, 73:1571–1606, 2007. doi: 10.1002/nme.2132.

[22] R. Udawalpola, E. Wasbro, and M. Berggren. Optimization of a variable mouth horn. *Int. J. Numer. Meth. Engng*, 85:591–606, 2010. doi: 10.1002/nme.2982.

[23] R. Christensen. Topology optimization of thermoviscous acoustics in tubes and slits with hearing aid applications. *Proceedings of the COMSOL Conference in Rotterdam*, 2017.

[24] M. J. Turner, R. W. Clough, H. C. Martin, and L. J. Topp. Stiffness and deflection analysis of complex structual. *Journal of the aeronautical sciences*, 23(9):805–823, 1956. doi: 10.2514/8.3664.

[25] T. W. Wu. *Boundary Element Acoustic*. WIT press, 2000.

[26] P. M. Juhl. *The Boundary Element Method for sound Field Calculations*. PhD thesis, Department of Acoustic Technology, Technical Univarity of Denmark, 1993.

[27] A. F. Seybert, B. Soenarko, F. J. Rizzo, and D. J. Shippy. An advanced computational method for radiation and scattering of acoustic waves in three dimensions. *Journal of the Acoustical Society of America*, 77(2):362–8, 362–368, 1985. doi: 10.1121/1.391908.

[28] A. Sutradhar, G. H. Paulino, and L. J. Gray. Symmetric galerkin boundary element method. *Symmetric Galerkin Boundary Element Method*, pages 1–276, 2008. doi: 10.1007/978-3-540-68772-6.

[29] V. Cutanda Henríquez and P. M. Juhl. OpenBEM - an open source Boundary Element Method software in acoustics,. *Proceedings of the 39th International Congress on Noise Control Engineering, Inter-noise, Lisbon (Portugal)*, 2010.

[30] H. A. Schenck. Improved integral formulation for acoustic radiation problems. *The Journal of the Acoustical Society of America*, 44(1):44, 1968. doi: 10.1121/1.1911085.

[31] G. Bartolozzi, D'Amico R., A. Pratellesi, and Pierini M. An efficient method for selecting chief points. In *Proceedings of the 8th International Conference on Structual Dynamics, 4-6 July, Leauven (Belgium)*, 2011.

[32] A. J. Burton and G. F. Miller. The application of integral equation methods to the numerical solution of some exterior boundary-value problems. *Proc. Roy. Soc. Lond. A.*, 323(1553):201–210, 1971. doi: 10.1098/rspa.1971.0097.

[33] S. Marburg. The Burton and Miller method: Unlocking another mystery of its coupling parameter. *Journal of Computational acoustics*, 24(1):1550016, 2016. doi: 10.1142/S0218396X15500162.

[34] D. S. Burnett. A three-dimensional acoustic infinite element based on a prolate spherodal multipole expansion. *The Journal of the Acoustical Society of America*, 96(5):2798, 1994. doi: doi.org/10.1121/1.411286.

[35] J. Autrique and F. Magoués. Studies of an infinite element method for acoustical radiation. *Applied Mathematical Modelling*, 30(7):641–655, 2005. doi: 10.1016/j.apm.2005.08.022.

[36] J. J. Shirron and S. Dey. Acoustic infinite elements for non-separable geometries. *Comput. Methods Appl. Mech. Engrg.*, 191(37-38):4123–4139, 2002. doi: 10.1016/S0045-7825(02)00355-9.

[37] J. Berenger. A perfectly matched layer for the absorption of electromagnetic waves. *Journal of Computational Physics*, 114(2):185–200, 1994. doi: 10.1006/jcph.1994.1159.

[38] Q. Liu and J. Tao. The perfectly matched layer for acoustic waves in absorptive media. *J. Acoust. Soc. Am.*, 102(4):2072–2082, 1997. doi: 10.1121/1.419657.

[39] A. Bermúdez, L. Hervella-Nieto, A. Prieto, and Rodriguez R. An optimal perfectly matched layer with unbounded absorbing function for time-harmonic acoustic scattering problems. *Journal of Computational Physics*, 223(2):469–488, 2007. doi: 10.1016/j.jcp.2006.09.018.

[40] COMSOL Multiphysics Reference Manual, version 5.2. COMSOL Multiphysics Reference Manual, version 5.2. COMSOL, Inc, www.comsol.com.

[41] G. Kirchoff. Uber den Einfluss der Wärmeleitung in einem Gase auf due Schallbewegung. *Annalen Der Physik Und Chemie*, 210(6):177–193, 1868. doi: 10.1002/andp.18682100602and10.1002/(ISSN)1521-3889.

[42] Rayleigh. *The theory of sound volume 2, 2nd edition*. Dover publications, 1894.

[43] C. Zwikker and C. W. Kosten. *Sound absorbing materials*. Elsevier publising company. inc, 1949.

[44] H. Tijdeman. On the propagation of sound waves in cylindrical tubes. *Journal of Sound and Vibration*, 39(1):1–33, 1975. doi: 10.1016/S0022-460X(75)80206-9.

[45] A. Cummings. Sound propagation in narrow tubes of arbitrary cross-section. *Journal of Sound and Vibration*, 162(1):27–42, 1991. doi: 10.1006/jsvi.1993.1100.

[46] A. Cummings. The propagation of plane sound waves in narrow and wide circular tubes, and generalization to uniform tubes of arbitary cross-sectional shape. *Journal of Acoustical Society of America*, 89(2):550–558, 1991. doi: 10.1121/1.400379.

[47] W. M. Beltman. *Viscothermal wave propagation including acousto-elastic interaction*. PhD thesis, University of Twente, Enschede, 1998.

[48] W. M. Beltman. Viscothermal wave propagation including acousto-elastic interaction, part I: theory. *Journal of Sound and Vibration*, 227(3):555–586, 1999. doi: 10.1006/jsvi.1999.2355.

[49] W. M. Beltman. Viscothermal wave propagation including acousto-elastic interaction, part II: applications. *Journal of Sound and Vibration*, 227(3):587–609, 1999. doi: 10.1006/jsvi.1999.2356.

[50] W. M. Beltman, P. J. M. van der Hoogt, R. M. E. J. Spiering, and H. Tijdeman. Implementation and experimental validation of a new viscothermal acoustic finite element for acousto-elastic problems. *Journal of Sound and Vibration*, 216 (1):159–185, 1998. doi: 10.1121/1.400379.

[51] A. H. Benade. On the Propagation of Sound Waves in a Cylindrical Conduit. *Journal of Acoustical Society of America*, 44(2):616–623, 1968. doi: 10.1121/1.1911130.

[52] D. H. Keefe. Acoustical wave propagation in cylindrical ducts: Transmission line parameter approximations for isothermal and nonisothermal boundary conditions. *Journal of Acoustical Society of America*, 75(1):58–62, 1984. doi: 10.1121/1.390300.

[53] J. C. Zuercher, E. V. Carlson, and M. C. Killion. Small acoustic tubes: New approximations including isothermal and viscous effects. *Journal of Acoustical Society of America*, 83(4):1653–1660, 1988. doi: 10.1121/1.395920.

[54] R. Christensen, P. Juhl, and Cutanda Henríquez V. Practical modeling of acoustic losses in air due to heat conduction and viscosity. In *Proceedings from the European Conference on Noise Control, June 29-July 4, Paris (France)*, 2008.

[55] M. Malinen, M. Lyly, P. Raback, A. Karkkainen, and L. Karkkainen. A finite element method for the modeling of termo-viscous effects in acoustics. In *Proceedings of the 4th European Congress on Computational Methods in Applied and Engineering ECCOMAS, Jyvaskyla, Finland*, 2004.

[56] M. J. J. Nijhof, Y. H. Wijant, and A. de Boer. An acoustic finite element including viscothermal effects. In *Proceedings from the 14th International Congress on Sound and vibration, 9-12 july, Cairns (Australia)*, 2007.

[57] L. Cheng, R. D. White, and K. Grosh. Three-dimensional viscous finite element formulation for acoustic fluid-structure interaction. *Computer Methods in Applied Mechanics and Engineering*, 197(49-50):4160–4172, 2008. doi: 10.1121/1.395920.

[58] N. Joly. Finite element modeling of thermoviscous acoustics in closed cavities. In *Proceeding from Acoustics'08, June 29-July 4, Paris (France)*, 2008.

[59] W. R. Kampinga, Y. H. Wijnant, and A. de Boer. Performance of Several Viscothermal Acoustic Finite Elements. *Acta Acoustica United with Acustica*, 96 (1):115–124, 2010. doi: 10.3813/AAA.918262.

[60] G. C. Martins, J. A. Cordioli, and R. Jordan. An analysis of mesh parameters of a viscothermal acoustic FE model. In *Proceedings from the 18th International Congress on Sound and vibration, 9-12 july, Rio de Janeiro (Brazil)*, 2011.

[61] R. Bossart, N. Joly, and M. Bruneau. Hybrid numerical and analytical solutions for acoustic boundary problems in thermo-viscous fluids. *Journal of Sound and Vibration*, 263(1):69–84, 2002. doi: 10.1016/S0022-460X(02)01098-2.

[62] K. Schmidt and A Thöns-Zueva. Impedance boundary conditions for acoustic time harmonic wave propagation in viscous gases. 2014.

[63] R. Kampinga, Y. Wijnant, and A. de Boer. A two step viscothermal acoustic FE method. In *Proceedings from the 16th International Congress on Sound and vibration, 5-9 july, Kraków (Poland)*, 2009.

[64] E. Dokumaci. An integral equation formulation for boundary element analysis of acoustic radiation problems in viscous fluids. *Journal of Sound and Vibration*, 147(2):335–348, 1991. doi: 10.1016/0022-460X(91)90720-5.

[65] E. Dokumaci. Prediction of the effects of entropy fluctuations on sound radiation from vibrating bodies using an integral equation approach. *Journal of Sound and Vibration*, 186(5):805–819, 1995. doi: 10.1006/jsvi.1995.0489.

[66] C. Karra, M. Ben Tahar, G. Marquette, and Chau M. T. Boundary element analysis of problems of acoustic propagation in viscothermal fluid. In *Proceedings of internose, 30 July - 2 August , Liverpool (UK)*, 1996.

[67] C. Karra and M. Ben Tahar. An integral equation formulation for boundary element analysis of propagation in viscothermal fluid. *J. Acoust. Soc. Am.*, 102 (3):1311–1318, 1997. doi: 10.1121/1.420050.

[68] V. Cutanda Henríquez and P. M. Juhl. Implementation of an acoustic 3d bem with visco-thermal losses. In *Proceedings of internose, 15-18 Sept , Insbruck (Austria)*, 2013.

[69] V. Cutanda Henríquez and P. M. Juhl. Verification of an acoustic 3d bem with visco-thermal losses. In *Proceedings of internose, 15-18 Sept , Insbruck (Austria)*, 2013.

[70] V. Cutanda Henríquez and P. M. Juhl. An axisymmetric boundary element formulation of sound wave propagation in fluids including viscous and thermal losses. *J. Acoust. Soc. Am.*, 134(5):3409–3418, 2013. doi: 10.1121/1.4823840.

[71] M. Bruneau, Ph. Herzog, J. Kergomard, and J. D. Polak. General formulation of the dispersion equation in bounded viso-thermal fluid, and application to some simple geometries. *Wave Motion **11***, pages 441–451, 1988. doi: 10.1016/j.jcp.2006.09.018.

[72] C. Grossmann and H. G Roos. *Numerical treatment of partial differential equations*. Springer, 2007.

[73] N. Sukumar and J. E. Bolander. Numerical computation of discrete differential operators on non-uniform grids. *Cmes-computer Modeling in Engineering and Sciences*, 4(6):691–705, 2003.

[74] R. Martinez. The thin-shape breakdown (tsb) of the helmholtz integral equation. *The Journal of the Acoustical Sociaty of America*, 90(5):2728, 1991. doi: 10.1121/1.401868.

[75] V. Cutanda Henríquez, P. M. Juhl, and F. Jacobsen. On the modeling of narrow gaps using the standard boundary element method. *Journal of the Acoustic Society of America*, 109(4):1296–1303, 2001. doi: 10.1121/1.1350399.

[76] S. Sorokin and S. T. Christensen. Low-frequency breakdown of boundary element formulation for closed cavities in excitation conditions with a 'breathing'-type component. *Communications in numerical methods in engineering*, 16(5):325–334, 2000. doi: 10.1002/(SICI)1099-0887(200005)16:5<325::AID-CNM339>3.0.CO;2-G.

[77] K. A. Hussain and K. S. Peat. Boundary element analysis of low frequency cavity acoustical problems. *Journal of Sound and Vibration*, 169(2):197–209, 1994. doi: 10.1006/jsvi.1994.1013.

[78] R. Garciía-Salgado, V. M. García-Chocano, D. Torrent, and J. Sánchez-Dehesa. Negative mass density and -near-zero quasi-two-dimensional metamaterial: Design and application. *Phys. Rev. B*, 88(22):224305, 2013. doi: 10.1103/PhysRevB.88.224305.

[79] V. M. Garcia-Chocano, L. Sanchis, A. Diaz-Rubio, J. Martinez-Pastor, F. Cervera, R. Llopis-Pontiveros, and J. Sanchez-Dehesa. Acoustic cloak for airborne sound by inverse design. *Applied Physics Letters*, 99(7):074102, 2011. doi: 10.1063/1.3623761.

[80] R. Gallego and A.E Martínez-Castro. Boundary integral equation for tangential derivative of flux in laplace and helmholtz equations. *Int. J. Numer. Meth. Engng*, 66(2):334–363, 2006. doi: 10.1002/nme.1563.

[81] S.A. Yang. Evaluation of the Helmholtz boundary integral equation and its normal and tangential derivatives in two dimensions. *Journal of Sound and Vibrations*, 301(3-5):864–877, 2007. doi: 10.1016/j.jsv.2006.10.023.

[82] S. Marburg and S. Schneider. Influence of Element Types on Numeric error for Acoustic Boundary Elements. *Journal of Computational Acoustics*, 11(3):363–386, 2003. doi: 10.1142/S0218396X03001985.

[83] S. Marburg. *Discretization Requirements: How many Elements per Wavelength are Necessary?. In: Marburg S., Nolte B. (eds) Computational Acoustics of Noise Propagation in Fluids - Finite and Boundary Element Methods.* Springer Berlin Heidelberg, 2008.

[84] J. A. Liggett and J. R. Salmon. Cubic spline boundary elements. *Int. J. Numer. Meth. Engng*, 17(4):543–556, 1980. doi: 10.1002/nme.1620170405and10.1002/(ISSN)1097-0207.

[85] A. W. Overhauser. Analytic definition of curves and surfaces by parabolic blending. Technical Report SL 68-40, Mathematical and Theoretical Sciences Department, Scientific Laboratory, Ford Motor Company, Dearborn, Michigan, May 1968.

[86] C. V. Camp and G. S. Gipson. Overhauser elements in boundary element analysis. *Mathematical and Computer Modelling*, 15(3-5):59–69, 1991. doi: 10.1016/0895-7177(91)90053-A.

[87] H. Hadavinia, R. P. Travis, and R. T. Fenner. C1-continuous generalised parabolic blending elements in the boundary element method. *Mathematical and Computer Modelling*, 31(8-9):17–34, 2000. doi: 10.1016/S0895-7177(00)00057-1.

[88] L. P. Blinova and V. N. Kozhin. Radiation of a cylinder oscillating in a viscous medium. *Fluid Dynamics*, 5(1):107–111, 1972. doi: 10.1007/BF01015007.

[89] S. Temkin. *Elements of acoustics*. Wiley New York, 1981.

[90] MATLAB Optimization Toolbox. MATLAB optimization toolbox, 2017b. The MathWorks, Natick, MA, USA.

[91] J. Nocedal and S. J. Wright. *Numerical Optimization, Second Edition*. Springer, 2006.

[92] O. Sigmund. On the usefulness of non-gradient approaches in topology optimization. *Structural and Multidisciplinary Optimization*, 43(5):589–596, 2011. doi: 10.1007/s00158-011-0638-7.

[93] D. Duhamel. Shape optimization of noise barriers using genetic algorithms, 2006.

[94] E. A. Divo, A. J. Kassab, and M. S. Ingber. Shape optimization of acoustic scattering bodies. *Engineering Analysis With Boundary Elements*, 27(7):695–703, 2003. doi: 10.1016/S0955-7997(03)00022-5.

[95] R. Toledo, J. J. Aznarez, D. Greiner, and O. Maeso. Shape design optimization of road acoustic barriers featuring top-edge devices by using genetic algorithms and boundary elements. *Engineering Analysis With Boundary Elements*, 63:49–60, 2016. ISSN 1873197x, 09557997. doi: 10.1016/j.enganabound.2015.10.011.

[96] T. Airaksinen and E. Heikkola. Multiobjective muffler shape optimization with hybrid acoustics modeling. *Journal of the Acoustical Society of America*, 130 (3):1359–1369, 2011. ISSN 15208524, 00014966, 01630962. doi: 10.1121/1.3621119.

[97] B. Mohammadi and O. Pironneau. *Applied Shape Optimization for Fluids, Second Edition*. Oxford university press, 2010.

[98] J. Semmler, L. Pflug, M. Stingl, and G. Leugering. *Shape Optimization in Electromagnetic Applications*, pages 251–269. Springer International Publishing, Cham, 2015. ISBN 978-3-319-17563-8. doi: 10.1007/978-3-319-17563-8_11. URL https://doi.org/10.1007/978-3-319-17563-8_11.

[99] R. Udawalpola. *Shape Optimization for Acoustic Wave Propagation Problems*. PhD thesis, University of uppsala, 2010.

[100] J. A. Samareh. A survey of shape parameterization techniques. *CEAS/AIAA/ICASE/NSA Langley International Forum on Aeroelasticity and Structual Dynamics*, pages 333–343, 1999.

[101] C. Liu, L. Chen, W. Zhao, and H. Chen. Shape optimization of sound barrier using an isogeometric fast multipole boundary element method in two dimensions, 2017.

[102] B. U. Koo, J. G. Ih, and B. C. Lee. Acoustic shape sensitivity analysis using the boundary integral equation. *Journal of the Acoustical Society of America*, 104 (5):2851–2860, 1998. doi: 10.1121/1.423869.

[103] L. Chen, C. Zheng, and H. Chen. A wideband fmbem for 2d acoustic design sensitivity analysis based on direct differentiation method. *Computational Mechanics*, 52(3):631–648, 2013. doi: 10.1007/s00466-013-0836-9.

[104] R. Udawalpola, E. Wadbro, and M. Berggren. Optimization of a variable mouth acoustic horn. *International Journal for Numerical Methods in Engineering*, 85 (5):591–606, 2011. doi: 10.1002/nme.2982.

[105] L. Chen, L. Liu, W. Zhao, and H. Chen. 2d acoustic design sensitivity analysis based on adjoint variable method using different types of boundary elements. *Acoustics Australia*, 44(2):343–357, 2016. doi: 10.1007/s40857-016-0065-4.

[106] T. Matsumoto, T. Yamada, T. Takahashi, C. J. Zheng, and S. Harada. Acoustic design shape and topology sensitivity formulations based on adjoint method and bem, 2011.

[107] ISO 10534-2:1998. ISO 10534-2:1998, Acoustics – Determination of sound absorption coefficient and impedance in impedance tubes – Part 2: Transfer-function method, 1998.

[108] R. E. Christensen and E. Fernandez-Grande. Experimental validation of a topology optimized acoustic cavity. *J. Acoust. Soc. Am.*, 138:3470–3474, 2015. doi: 10.1121/1.4936905.

Paper A

A Numerical Model of an Acoustic Metamaterial using the Boundary Element Method Including Viscous and Thermal Losses

(Including erratum)

Journal of Computational Acoustics, Vol. 25, No. 4 (2017) 1750006 (11 pages)

DOI: 10.1142/S0218396X17500060

INTERNATIONAL ASSOCIATION
FOR MATHEMATICS AND
COMPUTERS IN SIMULATION

A Numerical Model of an Acoustic Metamaterial Using the Boundary Element Method Including Viscous and Thermal Losses

V. Cutanda Henríquez*, P. Risby Andersen† and J. Søndergaard Jensen‡

Centre for Acoustic-Mechanical Micro Systems
Technical University of Denmark, Ørsteds Plads
Building 352, DK 2800, Kgs. Lyngby, Denmark
**vcuhe@elektro.dtu.dk*
†*prand@elektro.dtu.dk*
‡*json@elektro.dtu.dk*

P. Møller Juhl

Mærsk Mc-Kinney Møller Institute
University of Southern Denmark
Campusvej 55, DK 5230 Odense M, Denmark
pmjuhl@mmmi.sdu.dk

J. Sánchez-Dehesa

Wave Phenomena Group, Department of Electronic Engineering
Universitat Politècnica de València
Camino de Vera s.n. building 7F, ES 46022 Valencia, Spain
jsanched@upv.es

Received 31 May 2016
Accepted 3 October 2016
Published 13 December 2016

In recent years, boundary element method (BEM) and finite element method (FEM) implementations of acoustics in fluids with viscous and thermal losses have been developed. They are based on the linearized Navier–Stokes equations with no flow. In this paper, such models with acoustic losses are applied to an acoustic metamaterial. Metamaterials are structures formed by smaller, usually periodic, units showing remarkable physical properties when observed as a whole. Acoustic losses are relevant in metamaterials in the millimeter scale. In addition, their geometry is intricate and challenging for numerical implementation. The results are compared with existing measurements.

Keywords: Boundary element method; acoustic metamaterials; viscous and thermal acoustic losses.

1. Introduction

Acoustic metamaterials are artificial periodic structures with unit cells containing features such as resonators or scatterers.[1] The macroscopic acoustic properties may show values that

are outside the limits of what is achievable with regular materials in the sub-wavelength range, leading to interesting applications. Acoustic metamaterials have been studied with approximate analytical models and numerical methods, and measurements have been carried out.[2]

Sound waves are subject to losses due to fluid viscosity and heat exchange. Such losses are particularly relevant in the vicinity of boundaries: On one hand, particle velocity must match boundary velocity in its normal and tangential components (nonslip condition), creating a *viscous boundary layer* where viscous losses are relevant. On the other hand, the boundary usually has a much higher thermal conductivity than the fluid, thus reducing the temperature variations associated with acoustic waves, generating losses in a *thermal boundary layer* of a similar thickness, which for audible frequencies in air varies from a fraction of a millimeter to a few micrometers. These viscous and thermal losses are usually taken into account as an acoustic impedance of the boundary, and the sound field can be described by the lossless wave equation.[3] However, when the dimensions of the domain or some part of it are similar to the boundary layer thickness, it becomes necessary to take losses in the domain into account. This is the case of small acoustic devices such as acoustic transducers, couplers, hearing aids and small-scale acoustic metamaterials.

Recent research has led to new implementations of viscous and thermal losses in numerical methods. The boundary element method (BEM) is the basis of a full implementation with acoustic losses.[4,5] It is based on the Kirchhoff decomposition of the Navier–Stokes equations, where the so-called viscous, thermal and acoustic modes are described with different equations and coupled at the boundaries.[3,6,7] As in the lossless case, BEM meshes are defined on the boundaries, where the three modes are coupled through boundary conditions. The BEM with losses has been implemented for research purposes with the objective of dealing with particularly challenging and computationally demanding cases, such as condenser microphones and the structure brought forward in this paper.[8,9]

The finite element method (FEM) can also be used to directly solve the no-flow linearized Navier–Stokes equations with no further hypotheses, and is suitable for any geometry.[10–13] The FEM implementation with losses is available with some commercial FEM software packages.[14]

Besides the full BEM and FEM with viscous and thermal losses, there are other implementations where some restricting assumptions are made.[15,16] These alternative implementations are not investigated in this paper.

In a recent publication an acoustic metamaterial was studied using theoretical models, complemented with experiments.[17] However, poor agreement was found, and the authors speculated that the possible cause was the fact that no losses were included in the theoretical models. In this paper, BEM and FEM models with viscous and thermal losses are presented and employed for modeling the metamaterial. This particular problem has three features, that makes it relevant as a test case: (i) it has implications that are relevant for metamaterial research where acoustics losses are often neglected, (ii) it is a suitable problem where implementations of losses need to handle an intricate geometry, and (iii) it is on the limit of what is possible with numerical tools in terms of computational load. The present

paper is motivated by issues (ii) and (iii). There are indeed in the literature some examples of computationally heavy models and also containing intricacies.[15,18] Acoustic metamaterials, however, must contain and are based on internal, often complex, periodic structures where losses in individual units add up in the complete setup. They are a class of problems where full numerical models with no geometrical restrictions such as the aforementioned full BEM and FEM implementations with losses are the obvious choice.

In Sec. 2, the acoustic metamaterial and its desired properties are described, outlining the relevant background of the investigation in Ref. 17. Section 3 contains descriptions of the BEM and FEM models with losses employed. The results of the simulation with losses are presented and compared with existing measurements in Sec. 4. The paper is summarized in Sec. 5.

2. The Acoustic Metamaterial

An acoustic metamaterial is presented and studied in Ref. 17 using analytical and numerical models that do not include losses. This material is formed by unit cells as shown in Fig. 1, which are arranged in a periodic structure embedded between two horizontal planes separated by the distance h. The unit cell contains a number of wells of depth L acting as resonators. If the periodic structure is observed as a whole, there is a range of frequencies where it shows the so-called double-negative behavior: negative effective bulk modulus and negative effective mass. As a consequence, the lossless models predict that the metamaterial has extraordinary properties such as tunneling through narrow channels, control of the radiation field, perfect transmission through sharp corners and power splitting.

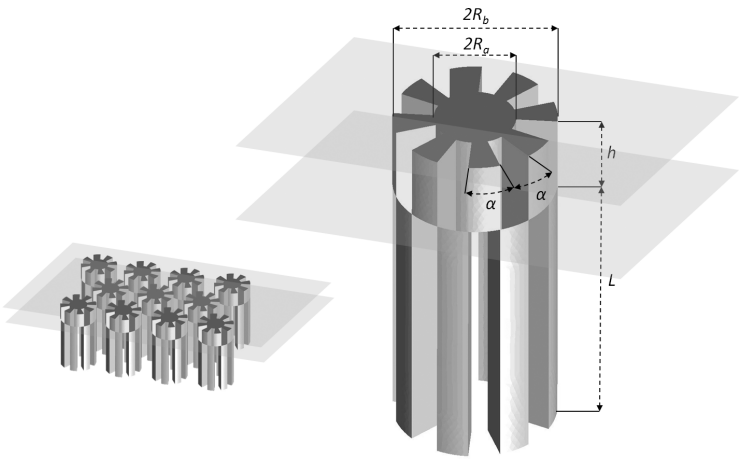

Fig. 1. Metamaterial single unit as described by Graciá-Salgado *et al.* with the relevant dimensions. The structure is embedded between two horizontal planes separated by distance h, leaving the lower part of length L below the lower plane and forming wells that may act as resonant elements. R_a is the inner radius, R_b is the outer radius and α is the angle that corresponds to a well (or between wells) sector. The units are arranged regularly as a grid to form the metamaterial, as shown in the sketch to the left.

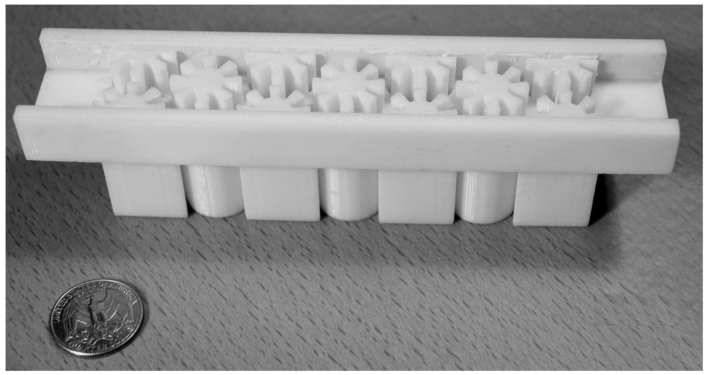

Fig. 2. Picture of one of the two metamaterial samples that were fabricated and measured by Graciá-Salgado *et al.* labeled Sample A. This sample is modeled in this paper using FEM and BEM with losses.

Table 1. Geometrical parameters of the two metamaterial samples used in experiments by Graciá-Salgado *et al.* See Fig. 1 for a graphical description.

Sample	R_a (mm)	R_b (mm)	h (mm)	L (mm)	a (mm)	α (rad)
A	4.6	9.2	9	31.5	21	$\pi/8$
B	3.5	7	9	22.5	21	$\pi/8$

Two versions of the metamaterial were produced by 3D printing and used for measurements by Graciá-Salgado *et al.* The scattering units were distributed in a hexagonal lattice with a lattice constant a of 21 mm. The measurements in Ref. 17 were made by inserting the fabricated section of the periodic structure into a rectangular duct and exposing it to a wave propagating inside. In order to evaluate the transmittance, the sound pressure measured at the end of the duct was compared with an equivalent reading in a rectangular duct with no metamaterial. The duct is narrow enough to ensure a good approximation to a plane wave with no high-order propagating modes in the bandwidth of interest (1–5 kHz). Two different samples of the metamaterial were fabricated with different geometrical parameters, one of them shown in Fig. 2. The dimensions are listed in Table 1. The samples are delimited by hard walls that are smooth and rigid, creating reflections and resembling a structure that extends infinitely in the direction normal to the wave on the lattice plane.

The measurement results did not confirm the expected double-negative behavior in any of the two samples. In the following sections, these results will be compared to models with losses. Only results for Sample A are presented in this paper.

3. Description of the Numerical Implementations

The two numerical implementations of acoustics with thermal and viscous losses are outlined in the following. A short description of each of them is followed by model details of the metamaterial test case.

3.1. *BEM with losses*

The BEM implementation with losses is based on the Kirchhoff decomposition of the Navier–Stokes equations,[6,7]

$$(\Delta + k_a^2)p_a = 0, \tag{1}$$

$$(\Delta + k_h^2)p_h = 0, \tag{2}$$

$$(\Delta + k_v^2)\mathbf{v}_v = \mathbf{0}, \quad \text{with } \Delta \cdot \mathbf{v}_v = 0, \tag{3}$$

where the indexes (a, h, v) represent the so-called acoustic, thermal and viscous modes, which can be treated independently in the acoustic domain and linked through the boundary conditions. The total pressure is the sum $p = p_a + p_h$ of the acoustic and thermal components (there is no pressure associated with the viscous mode), while the velocity has contributions from all three modes $\mathbf{v} = \mathbf{v}_a + \mathbf{v}_h + \mathbf{v}_v$. The wavenumbers k_a, k_h and k_v are based on the lossless wavenumber k and physical properties of the fluid, such as the viscosity, bulk viscosity and thermal conductivity coefficients, air density, and specific heats. Equation (1) is a wave equation, while Eqs. (2) and (3) are diffusion equations, given the large imaginary part of k_h and k_v. Equation (3) is a vector equation and therefore it can be split into three components, giving a total of five equations with five unknowns.

The implementation in BEM is made by discretizing Eqs. (1)–(3) independently and combining them into a single matrix equation using the boundary conditions. The matrix equation is solved for the acoustic pressure p_a and subsequently other variables are obtained on the boundary. From the boundary values, any domain field point can be calculated.[4,5] The implementation is based on the research software OpenBEM, which solves the Helmholtz wave equation using the direct collocation technique.[19] Equations (1)–(3) are formally equivalent to the Helmhotz wave equation.

In BEM, only the domain boundary is meshed, saving degrees of freedom as compared with other numerical methods like the FEM. However, the BEM coefficient matrices are frequency dependent and fully populated, which may counterbalance the mesh reduction when compared with other methods. In the case of BEM with viscous and thermal losses, three sets of coefficient matrices are used, corresponding to the three *modes*: acoustic, thermal and viscous. The thermal and viscous coefficient matrices are usually sparse due to the short reach of such effects, as compared with the overall dimensions of the setup.

3.1.1. *Description of the BEM metamaterial model*

The boundary mesh, shown in Fig. 3, has been created using the Gmsh grid generator.[20] The metamaterial mesh has 6799 nodes and 13 606 elements. The BEM implementation, and the OpenBEM software it is based on, are fully implemented in the Matlab programming language and no external solvers or preconditioners are used. The calculation of the coefficient matrices needs about 1 h per frequency in a six-core 3.5 GHz processor with 64 GB of memory. The limiting factor is processor capacity, rather than memory. Solving the system takes

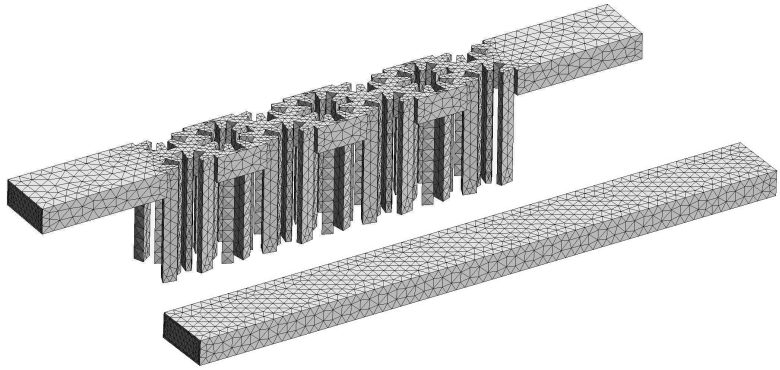

Fig. 3. Boundary mesh employed in the BEM model with losses. Upper, metamaterial sample; lower, empty duct. Linear three-node triangular elements are used.

6 mins per frequency. The size of the system to be solved is the same as the number of degrees of freedom of the boundary mesh. The calculated frequencies are spaced by 100 Hz from 1 kHz to 5 kHz, giving 41 frequencies. The sparsity of the thermal and viscous coefficient matrices is believed to enable some speed increase of the calculation, but it has not been directly exploited.

In parallel, an empty rectangular duct of the same dimensions has been calculated. The purpose of the empty duct is acting as a reference for the calculation of the metamaterial transmittance and reflectance. This reference could also be calculated analytically, but the numerical version serves as a test for the calculation issues described in the following.

The duct where the metamaterial is inserted and the empty duct used as a reference are assumed sufficiently long so that no reflections are created on any of the two terminations, emitting and receiving. In the FEM calculation described later, perfectly matched layers are used for this purpose. In the BEM code, the emitter and receiving lids are given an impedance of ρc instead, to make them anechoic to an incoming plane wave. One of the terminations acts as a plane piston with a normal velocity of $1/\rho c$ m/sec amplitude, so as to normalize the resulting plane wave to an amplitude of one.

The boundary conditions are set so as the mesh nodes on the rim of the lids can represent a sharp transition between the lid and the duct walls. This is done by splitting the columns in the acoustic coefficient matrix corresponding to the normal derivative of the pressure in the acoustic mode.[21]

In order to compare with the measurements in Ref. 17, transmitted power at the receiving end needs to be calculated. Pressure and particle velocity in the propagation direction (X-coordinate, duct length direction) are calculated on 10 field points situated on a plane that is normal to the propagation direction, thus allowing an estimation of the acoustic intensity and power. An equivalent calculation is made at the emitting side which is used to calculate the reflectance of the metamaterial. Measurement results are not available for the latter calculation, and it is not shown in this paper.

3.2. *FEM with losses*

Corresponding FEM simulations were carried out using the commercial software COMSOL. To accurately capture the effects of viscosity and thermal conduction for complex geometries like the metamaterial, the full linearized Navier–Stokes description is necessary. The equations solved are the momentum, continuity and energy equations,

$$i\omega\rho_0\mathbf{u} = \nabla\cdot\left(-p\mathbf{I} + \mu\left(\nabla\mathbf{u} + \nabla\mathbf{u}^T\right) - \left(\frac{2}{3}\mu - \mu_B\right)(\nabla\cdot\mathbf{u})\,\mathbf{I}\right) + \mathbf{F}, \tag{4}$$

$$i\omega\rho + \rho_0\nabla\cdot\mathbf{u} = 0, \tag{5}$$

$$i\omega\rho_0 C_p T = -\nabla\cdot(-k\nabla T) + i\omega\alpha_0 T_0 p, \tag{6}$$

$$\rho = \rho_0(\beta_T p - \alpha_0 T). \tag{7}$$

The acoustic variables are; particle velocity $\mathbf{u}$, pressure p, temperature T. $\mathbf{F}$ is a volume force acting on the fluid. The parameters of air are expressed as: ρ_0 the equilibrium density, T_0 the equilibrium temperature, μ the dynamic velocity, μ_B the bulk viscosity, C_p the heat capacity at constant pressure, k thermal conductivity, α_0 coefficient of thermal expansion and β_T isothermal compressibility.

The above equation set is solved using the regular FEM approach, transforming the equations into weak form. This results in a system of equations having pressure, particle velocity and temperature as variables. Five degrees of freedom are introduced per node, meaning that the system in general will be five times larger as compared to the lossless counterpart for the same mesh.

3.2.1. *Description of the FEM metamaterial model*

The model geometry is shown in Fig. 4, highlighting the Perfectly Matched Layers (PML) and the excitation. The models of the empty duct and the actual metamaterial are shown together, but the two geometries are solved separately, so that more elements in the metamaterial computation can be employed. Excitation of the waveguides is done though a body force with a small gap of air followed by a PML. This configuration was chosen to ensure full absorption at the inlet of waves reflected back from the metamaterial. Similarly, waves emerging at the other end of the metamaterial section are absorbed in the model with another PML.

In order to capture the effects of viscosity and thermal conduction in FEM, the viscous and thermal boundary layers need to be meshed with mesh densities that are much higher than in the remaining domain regions. In complex models like the metamaterial sample modeled in this paper, this will mean a substantial increase of the number of degrees of freedom. The computer used for the FEM simulations has a six-core processor with 128 GB of memory. The presented results are computed with a memory load of approximately 100 GB. Computation of the full frequency range is carried out with a 25 Hz stepping, taking approximately 21 h. The resulting system consists of 3.6 million degrees of freedom, solved with an iterative solver using direct preconditioners.[22]

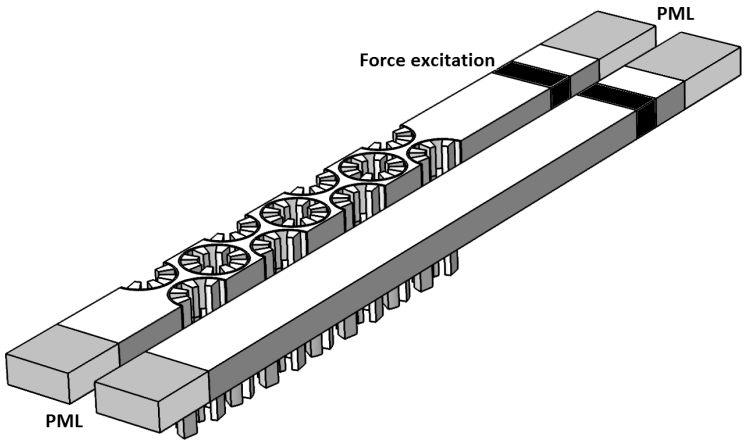

Fig. 4. Geometry of the FEM model with losses, including the metamaterial sample and the reference rectangular duct. The PML terminations and force excitations are marked in the drawings.

Due to the usually larger system size of the viscothermal FEM formulation, special attention must be paid to the meshing of the domain, especially near wall regions where viscosity and thermal conduction become important. Boundary layer meshes for the entire geometry have been applied. Several configurations ranging from one to five element layers within the viscothermal boundary layers have been studied. These different computations only show insignificant changes in the computational result, indicating that the calculations can be limited to a very rough boundary layer mesh containing only one element within the boundary layer, thus reducing the overall computational load. Nevertheless, the presented FEM results correspond to simulations with the highest possible mesh density near boundaries.

4. Results

As previously mentioned, there are measurements available from Graciá-Salgado *et al.* of the transmittance (transmitted power/incident power) of the metamaterial. Figure 5 shows these measurements together with the results from BEM and FEM with losses. The FEM calculation with no losses (also from Ref. 17) is also shown. The lossless metamaterial exhibits negative density and bulk modulus (double-negative behavior) within a narrow band close to 2.5 kHz, which disappears when losses are present. This is an important outcome that may have an impact in metamaterial design.

In this paper we are concerned however with the performance of the numerical methods. The BEM and the FEM calculations with losses appear to be rather close to each other, and away from the measurement results. Only at high frequencies this picture is less clear, possibly a consequence of the BEM mesh density becoming insufficient. Indeed all three results with losses (BEM, FEM and measurements) are difficult to obtain and subject to errors, so no clear-cut conclusion can be drawn. In FEM, it has not been possible to increase

significantly the mesh at the boundary layers in order to study its effect. In BEM, a mesh with less nodes than the one employed in this paper showed similar results. Also in BEM, a drastic increase in mesh density would also make the calculation unaffordable. However, to some extent the FEM and BEM results validate each other.

Using the numerical calculations, it is possible to examine the behavior of the structure in a detail that is not reachable to measurements. As an example, Fig. 6 shows the pressures along the propagation direction on the boundary of the metamaterial within the double-negative band, calculated using BEM. Note that the BEM predicts the double-negative behavior at a frequency of around 2600 Hz, and this value is used in Fig. 6. The FEM calculation with no losses in Fig. 5 shows a double negative band at 2400–2500 Hz.

If the duct was plain and empty, the boundary conditions would produce a plane progressive wave of amplitude 1, which is marked in Fig. 6 as thin solid lines. The amplitudes

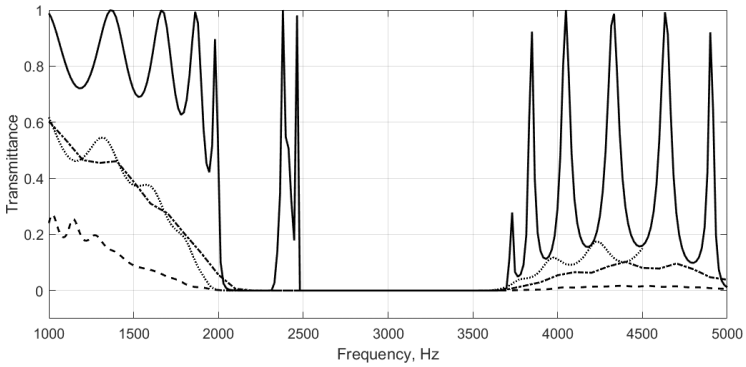

Fig. 5. Transmittance, obtained at the receiving end of the setup. Solid line, FEM model without losses; dotted line, FEM model with losses; dash-dotted line, BEM model with losses; dashed line, measurements by Graciá-Salgado *et al.*

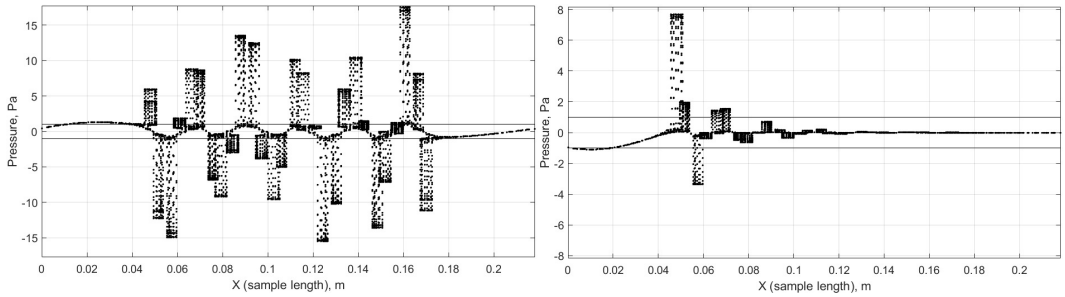

Fig. 6. Sound pressure at a given instant of time on the surface mesh, calculated with BEM. The abscissas are the positions of the nodes in the propagation direction. The frequency is 2600 Hz, which is within the double-negative band predicted by BEM. Left, calculation with no losses; right, calculation with viscous and thermal losses.

in the resonator units are much larger, and in the simulation with no losses they combine in such a way as to produce the extraordinary behavior described by Graciá-Salgado *et al.* The same figure shows the effect of losses, which prevent wave propagation to the receiving end and destroy the interplay between metamaterial units.

5. Conclusions

A metamaterial test case from the literature has been modeled using BEM and FEM with losses. The simulations confirm the conclusion from existing measurement results: the double-negative behavior associated with the metamaterial's extraordinary properties is prevented by viscous and thermal losses. This conclusion applies in principle to this particular metamaterial, but may serve as a warning when estimating the behavior of similar structures.

The test case is a challenging calculation both for BEM and FEM with losses. Numerical transmittance results with losses using FEM and BEM are not far from each other, and both predict less losses than the measurements. This can serve, to some extent, as a verification of the numerical implementations with losses. However, it should be kept in mind that measurements are also challenging and subject to deviations. Further refinement of the numerical models would be necessary to obtain a better estimation, but this would lead to a drastic increase of the computational burden, which is not bearable with the computers used in this work. A possible way forward would be the creation of more efficient implementations of acoustic losses.

Acknowledgments

The authors wish to thank Mads J. Herring Jensen, from the company COMSOL, for his support in setting up the FEM model of the metamaterial. J. Sánchez-Dehesa acknowledges the support by the Spanish Ministerio de Economía y Competitividad, and the European Union Fondo Europeo de Desarrollo Regional (FEDER) through Project No. TEC2014-53088-C3-1-R.

References

1. R. V. Craster and S. Guenneau (eds.), *Acoustic Metamaterials. Negative Refraction, Imaging, Lensing and Cloaking* (Springer, London, 2013).
2. S. A. Cummer, J. Christensen and A. Alù, Controlling sound with acoustic metamaterials, *Nat. Rev. Mat.* **1**(3) (2016) 16001.
3. P. M. Morse and K. U. Ingard, *Theoretical Acoustics* (McGraw-Hill, Princeton, 1968).
4. V. Cutanda Henríquez and P. M. Juhl, An axisymmetric boundary element formulation of sound wave propagation in fluids including viscous and thermal losses, *J. Acoust. Soc. Am.* **134**(5) (2013) 3409–3418.
5. V. Cutanda Henríquez and P. M. Juhl, Implementation of an acoustic 3D BEM with visco-thermal losses, in *Proc. Internoise 2013*, 15–18 September 2013, Innsbruck, Austria.
6. A. D. Pierce, *Acoustics*: *An Introduction to Its Physical Principles and Applications*, Chap. 10 (McGraw Hill, New York, 1981).

7. M. Bruneau, Ph. Herzog, J. Kergomard and J. D. Polack, General formulation of the dispersion equation in bounded visco-thermal fluid, and application to some simple geometries, *Wave Motion* **11** (1989) 441–451.
8. V. Cutanda Henríquez and P. M. Juhl, Modelling measurement microphones using BEM with visco-thermal losses, in *Proc. Joint Baltic-Nordic Acoustics Meeting*, 18–20 June 2012, Odense, Denmark.
9. V. Cutanda Henríquez, S. Barrera-Figueroa, A. Torras Rosell and P. M. Juhl, Study of the acoustical properties of a condenser microphone under an obliquely incident plane wave using a fully coupled three-dimensional numerical model, in *Proc. Internoise 2015*, 9–12 August 2015, San Francisco, USA.
10. R. Bossart, N. Joly and M. Bruneau, Methodes de modelisation numerique des champs acoustiques en fluide thermovisqueux, in *Actes du 6e Congrès Franais d'Acoustique*, Lille, France (2002), pp. 411–414.
11. M. Malinen, M. Lyly, P. Råback, A. Kärkkäinen and L. Kärkkäinen, A finite element method for the modeling of thermo-viscous effects in acoustics, in *Proc. 4th European Cong. Computational Methods in Applied Sciences and Engineering (ECCOMAS)*, Jyväskylä, Finland (2004).
12. N. Joly, Coupled equations for particle velocity and temperature variation as the fundamental formulation of linear acoustics in thermo-viscous fluids at rest, *Acta Acust. Acust.* **92** (2006) 202–209.
13. R. Kampinga, Performance of several viscothermal acoustic finite elements, *Acta Acust. Acust.* **96** (2010) 115–124.
14. COMSOL Multiphysics Reference Manual, version 5.2 (2015).
15. R. Kampinga, An efficient finite element model for viscothermal acoustics, *Acta Acust. Acust.* **97** (2011) 618–631.
16. W. M. Beltman, Viscothermal wave propagation including acousto-elastic interaction. Part I: Theory and Part II: Applications, *J. Sound Vib.* **227**(3) (1999) 555–586 and 587–609.
17. R. Graciá-Salgado, V. M. García-Chocano, D. Torrent and J. Sánchez-Dehesa, Negative mass density and ρ-near-zero quasi-two-dimensional metamaterials: Design and applications, *Phys. Rev. B* **88** (2013) 224–305.
18. D. Homentcovschi and R. N. Miles, An analytical-numerical method for determining the mechanical response of a condenser microphone, *J. Acoust. Soc. Am.* **130**(6)(2011) 3698–3705.
19. V. Cutanda Henríquez and P. M. Juhl, OpenBEM — An open source Boundary Element Method software in Acoustics, in *Internoise 2010*, 13–16 June 2010, Lisbon, Portugal.
20. C. Geuzaine and J.-F. Remacle, Gmsh: A three-dimensional finite element mesh generator with built-in pre- and post-processing facilities. *Int. J. Numer. Methods Eng.* **79**(11) (2009) 1309–1331.
21. P. M. Juhl, The boundary element method for sound field calculations, Ph.D. thesis, Report No. 55, Technical University of Denmark (1993).
22. COMSOL Multiphysics Acoustics Module User's Guide, version 5.2 (2015).

Journal of Computational Acoustics

Erratum to "A Numerical Model of an Acoustic Metamaterial using the Boundary Element Method Including Viscous and Thermal Losses" (Journal of Computational Acoustics, 2016, Volume 25, DOI: 10.1142/S0218396X17500060)

V. Cutanda Henríquez*, P. Risby Andersen†, J. Søndergaard Jensen‡

Centre for Acoustic-Mechanical Micro Systems, Technical University of Denmark
Ørsteds Plads, Building 352, DK-2800, Kgs. Lyngby, Denmark
**vcuhe@elektro.dtu.dk*
†*prand@elektro.dtu.dk*
‡*json@elektro.dtu.dk*

P. Møller Juhl

Mærsk Mc-Kinney Møller Institute, University of Southern Denmark,
Campusvej 55, DK-5230 Odense M, Denmark
pmjuhl@mmmi.sdu.dk

J. Sánchez-Dehesa

Wave Phenomena Group, Department of Electronic Engineering, Universitat Politècnica de València,
Camino de Vera s.n. (building 7F), ES-46022 Valencia, Spain
jsanched@upv.es

Received (Day Month Year)
Revised (Day Month Year)

One of the curves in Figure 5 of the published paper should be modified. It corresponds to the transmittance measurement results. The results were obtained from a previous publication (reference [17] in the published paper), but the data was incorrectly squared.

Figure 1 below is a new version of Figure 5 in the original paper, where the measurement curve has been plotted without squaring. The measurement plot is now closer to the transmittance curves calculated using the Finite Element Method and the Boundary Element Method with losses.

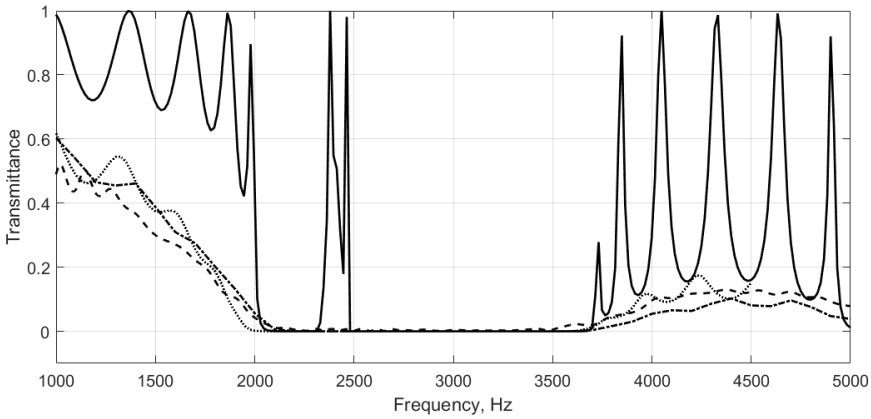

Fig. 1. Transmittance, obtained at the receiving end of the setup. Solid line, FEM model without losses; dotted line, FEM model with losses; dash-dotted line, BEM model with losses; dashed line, measurements by Graciá-Salgado et al..

Paper B

Visco-thermal effects on an acoustic cloak based on scattering cancellation

NOVEM 2018
Noise and vibration emerging methods
The 6th conference, 7 – 9 May 2018
Ibiza – Spain

VISCO-THERMAL EFFECTS ON AN ACOUSTIC CLOAK BASED ON SCATTERING CANCELLATION

Peter Risby Andersen[1*] , Vicente Cutanda Henríquez[1†], Niels Aage[1‡] and José Sánchez-Dehesa [2]

[1]Centre for Acoustic-Mechanical Micro Systems, Technical University of Denmark, Ørsteds Plads, Building 352, DK-2800, Kgs. Lyngby, Denmark
[*]Email: prand@elektro.dtu.dk
[†]Email: vcuhe@elektro.dtu.dk
[‡]Email: naage@mek.dtu.dk

[2] Wave Phenomena Group, Universitat Politècnica de València, Camino de Vera s.n. (Building 4D), ES-46022 Valencia, Spain
Email: jsdehesa@upv.es

ABSTRACT

Recent research has shown that the performance of acoustic metamaterials can be greatly influenced by the effects of viscous and thermal dissipation. In the worst case, an isentropic assumption can lead to an undesired performance. To further investigate the impact of losses on novel acoustic devices, an already known acoustic cloak is validated numerically, including the viscous and thermal dissipation effects. The specific cloaking device is realized using 120 small aluminium cylinders distributed around a larger cylindrical object, in such a way, that plane waves incident to the cloak will appear to be undisturbed, at the operational frequency of 3061 Hz. The initial optimization procedure for determining the positions of the small cylinders assumes isentropic conditions neglecting dissipative effects, meaning that the actual realization of the cloak might behave differently than intended. Through numerical simulations the acoustic cloak performance is compared with and without dissipation, giving an estimate of the differences that can be expected in similar cases. The results show that losses have very little impact on the key performance characteristic, the averaged visibility.

1 INTRODUCTION

The effect of viscous and thermal acoustic losses is often neglected when developing, for example, acoustic metamaterials or other type of acoustic devices, due to the assumption that viscous and thermal boundary layers are much smaller compared to the geometry under consideration. This

sometimes overlooked effect was recently discussed in several papers, showing that losses can play a significant role for the behaviour of such devices, meaning that the usual isentropic assumption might not be sufficient.[1–3] To further investigate the effect of losses, this paper validates the dissipative impact on an already existing acoustic cloak found in a paper by García-Chocano.[4] The specific cloak was designed from an inverse design optimization procedure by distributing small rigid cylinders around a larger cylindrical object a in way that effectively hides the larger cylinder due to scattering cancellation. The general acoustic behaviour of the cylinders is described through a 2D multiple scattering method assuming isentropic conditions and an incident plane wave.[5] The final optimized cloak design consists of 120 small cylinders distributed around the object, with an operational frequency of 3061 Hz. Similar cloaking designs based on scattering cancellation developed through topology optimization can be found in the literature of both acoustic and optical cloaks.[6–8] In the paper by García-Chocano the design is validated both experimentally and numerically using a two-dimensional isentropic Finite Element Method (FEM) description of the cloak. One of the findings is that the experimental cloaking performance deviates from the FEM simulations assuming an incident plane wave to the cloak. This difference is partly improved by fitting the actual, non-plane, shape of the experimental incident wave to the FEM calculations. But even with this improvement, experimental and numerical results still seem to deviate outside the operational frequency. In the experimental work an attenuation of the pressure amplitude of 15 % as compared to simulations is also observed.

In the following, the cloak will be evaluated numerically using both FEM and Boundary Element Method (BEM) including the effects of acoustic viscous and thermal losses, to give an estimate of how the performance can be expected to change due to losses. Simulations will, for simplicity and clarity, restrict themselves to incident plane waves, since this is also the initial design assumption.

Firstly, the cloak geometry and performance parameter, the averaged visibility, are introduced. This is followed by sections on the numerical implementations including losses and simulation results. Finally, conclusions are given on what to expect due to losses on this type of acoustic device.

2 ACOUSTIC CLOAKING DEVICE

This section provides a brief introduction to the actual acoustic cloak under study here. For a more comprehensive description, the reader is referred to the original paper by García-Chocano.[4] The final optimized distribution of the 120 cylinders is seen in Figure 1. Each of the small cylinders has the same radius of 0.75 cm and the radius of the larger central cylindrical object is 11.25 cm.

The experiment was realized using aluminium cylinders placed in a two dimensional acoustic wave guide with the dimensions $4.6 \times 3.66 \times 0.05$ m^3, ensuring that the chamber is well below the cut-off frequency of plausible modes in the z axis. This experimental setup is expected to be equivalent to simplified two-dimensional numerical simulations. While these two-dimensional type of wave guide computations are simpler to conduct, they do lack the losses due to the upper and lower walls of the wave guide. In order to examine this, the results section also contains simulations of an empty duct including losses, investigating the effect of not including the upper and lower walls of the wave guide.

2.1 Visibility

The main validation of the performance and impact due to losses will be done in terms of the so-called averaged visibility, which is a measure of how well the cloak hides the larger cylinder. The

averaged object visibility, γ, is defined as [4]

$$\gamma = \frac{1}{N} \sum_{j} \frac{|P_{max,j}| - |P_{min,j}|}{|P_{max,j}| + |P_{min,j}|} \tag{1}$$

with $P_{max,j}$ and $P_{min,j}$ being the maximum and minimum pressure amplitudes along the wave front j in the measurement region shown in Figure 1, located behind the cloak. The measurement region will contain around five wavelengths near the operational frequency.

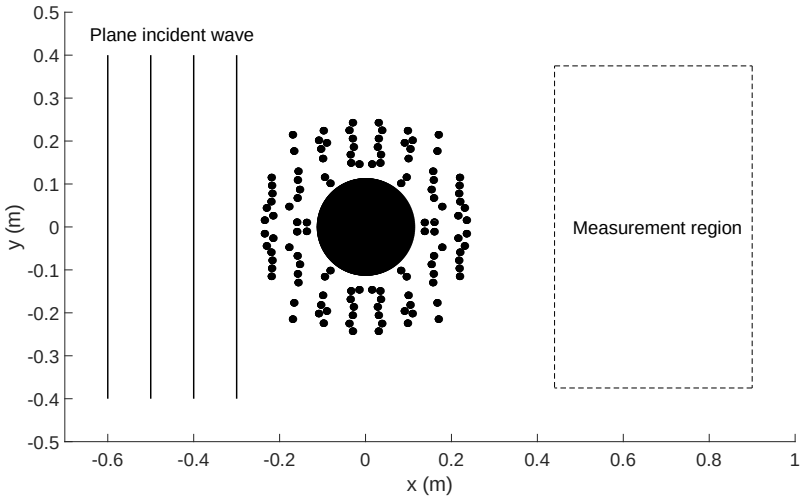

Figure 1: The acoustic cloak geometry as proposed in [4]. The cloak consists of 120 cylinders, all with the same radius of 0.75 cm, distributed around a larger central cylindrical object with a radius of 11.25 cm. Evaluation of the visibility, γ, is done by observing the acoustic pressure in the measurement region as seen in the figure.

3 NUMERICAL METHODS INCLUDING VISCOUS AND THERMAL LOSSES

The two main mechanisms accounting for the loss of energy in an acoustic wave are viscous and thermal effects. Fluid particles tend to stick to the surfaces (no-slip condition), forming the so-called viscous boundary layer. The viscous boundary layer thickness is frequency dependent. For the operational frequency of the cloak, the expected boundary layer thickness is approximately 38 μm. [9] A similarly sized thermal boundary layer will also form near boundaries, due to the much higher heat capacity of the boundary material, essentially withholding an isothermal boundary condition, forcing flux of heat between the boundary and the acoustic medium. To account for the effects of both viscous and thermal losses in numerical acoustics simulations the full linearised Navier-Stokes equations assuming no flow are utilized. Mainly two numerical acoustic methods for the full linearised Navier-Stokes equations exist, namely the BEM and the FEM. Both methods will be used in the following sections to account for losses.

3.1 BEM with losses

The BEM implementation including losses relies on the Kirchoff decomposition of the Navier-Stokes equations,

$$\Delta p_a + k_a^2 p_a = 0 \tag{2}$$

$$\Delta p_h + k_h^2 p_h = 0 \tag{3}$$

$$\Delta \vec{v}_v + k_v^2 \vec{v}_v = 0, \quad \text{with} \quad \nabla \cdot \vec{v}_v = 0 \tag{4}$$

discretized individually using direct collocation BEM and coupled at the boundary through the no-slip and isothermal boundary conditions. The subscripts a, h and v indicate the acoustic, thermal and viscous modes, respectively. While Eq. (2) resembles an actual acoustic Helmholtz equation, Eqs. (3) and (4) can rather be considered as diffusion equations. A full review of the method and implementation aspects can be found in the work by Cutanda and co-workers [10, 11]. This approach was further extended by the first author to include two dimensions using the research software OpenBEM.[12, 13] The following BEM simulations apply a mesh using quadratic continuous Lagrange elements, having an element size well above the usual 6 elements per wave length assumption. The resulting system of equations consists of approximately 6000 degrees of freedom.

3.2 FEM with losses

The FEM implementation of the Navier-Stokes equations relies on a more direct approach. Applying FEM to the linearised conservation of mass, energy and momentum equations.[14, 15] Simulations were carried out using the "Thermoviscous" implementation in COMSOL MULTIPHYSICS®. The simulated geometry requires free field conditions, which is full-filled by using a surrounding perfectly matched layer (PML) of the acoustical domain. Further, simulations are carried out using a sufficient boundary layer mesh adapted to the expected layer thickness and having eight elements covering the surface's perpendicular direction. The complete system solved for has around 4 million degrees of freedom.

4 SIMULATION RESULTS

In the following subsections, simulation results are presented of the acoustic cloak, and the influence of viscous and thermal losses is discussed. A direct comparison of the acoustic pressure at the operational frequency of the cloak is introduced first, followed by a section on the main performance characteristics of the cloak in terms of the average visibility. In the end, simulation results are shown of an empty waveguide with a finite height, to give an estimate of the attenuation due to the upper and lower walls of the wave guide used in the experiment.

4.1 Acoustic pressure field at the operational frequency

The real part of the acoustic pressure is shown in Figure 2 in the computational domain for both the isentropic and lossy FEM solution of the cloak at the operational frequency, 3061 Hz. The Figure also contains an absolute difference plot of the two field calculations showing that some differences exist. Especially, the interior of the cloak seems to show the larger differences. The measurement region presents smaller differences, having a periodic difference behaviour, perhaps indicating some phase shifting of the resulting wave due to losses.

4.2 Visibility of the cloak

The averaged visibility with and without losses is seen in Figure 3. The black curve is the isentropic solution for a FEM calculation, similar lossless BEM calculations have been conducted

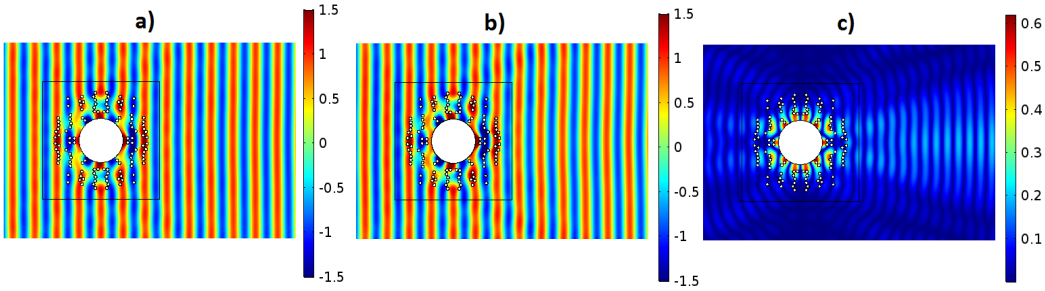

Figure 2: A comparison of the real part of the acoustic pressure for FEM simulations a) insentropic caculation b) including viscous and thermal losses c) the absolute difference between the lossy and isentropic real part of the pressure. The frequency is 3061 Hz

showing identical visibility, but for brevity only the FEM solution is plotted. The average visibility of the lossy FEM (green curve) and BEM (Red dots) simulations is also plotted, showing that the FEM solution is deviating more from the isentropic solution compared to BEM calulations. It is not fully understood why there is this difference between lossy FEM and BEM calculations. The BEM calculations are very similar to the isentropic calculation. Due to the difference in the simulation parameters, speed of sound and temperature conditions of the experimental data, all simulated data is shifted 26 Hz to match the operational frequency of the measurements, 3061 Hz. For all the numerical results there is a large deviation in averaged visibility from the actual measurements, which is also the case for the plane incident wave calculations in the original paper by García-Chocano. The reason for this is assumed to be the non-plane incident wave front of the actual experiment. It should also be noted that comparing the original insentropic plane incident wave averaged visibility calculations found in the work by García-Chocano, there is a slight disagreement in the averaged visibility outside the operational frequency. It is unclear why this difference exists, but an explanation could perhaps be the different simulation boundary conditions or parameters employed. The averaged visibility results presented in Figure 3 do in general have a slightly more broadband nature.

4.3 Empty waveguide

Since the simulations so far have shown that the losses seem to only have a minor impact on the solution of the averaged visibility, it is interesting to investigate what amount of attenuation can be expected from the finite height of the waveguide itself, since this effect is not included when considering the cloak as a two-dimensional study case. Therefore, yet another FEM simulation has been conducted representing an empty infinite slit in two dimensions, see Figure 4, containing the height of the actual waveguide and using a perfectly matched layer to replicate an infinite termination. In the numerical simulations, the duct is set with a pressure magnitude of 1 Pa at the inlet. The acoustic pressure is then measured at the central part of duct, giving an average estimate of what kind of attenuation is to be expected due to losses from the upper and lower walls of the waveguide. The average attenuation for different waveguide heights is seen in Figure 5. In the experiment, the waveguide height is 5 cm, which simulations show corresponds to an average attenuation of 2.5 % in the measurement region. As it is observed, the average attenuation magnitude is sensitive to the chosen height of the waveguide, so care must be taken when designing experiments of this type to avoid the influence from losses.

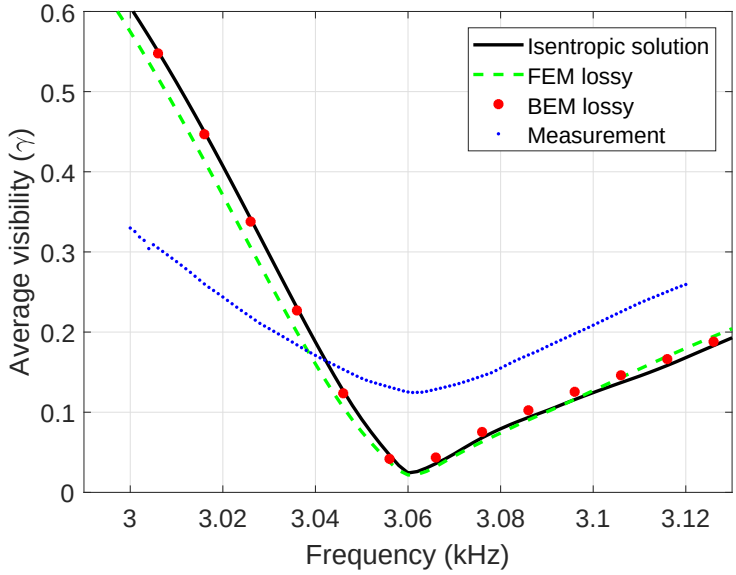

Figure 3: Average visibility of the cloak, comparing the effect of lossy FEM simulations (green dashed line), lossy BEM simulations (big red dots) to an isentropic FEM calculation (black solid line). The Figure also includes measurements (small blue dots) found in Ref. [4]

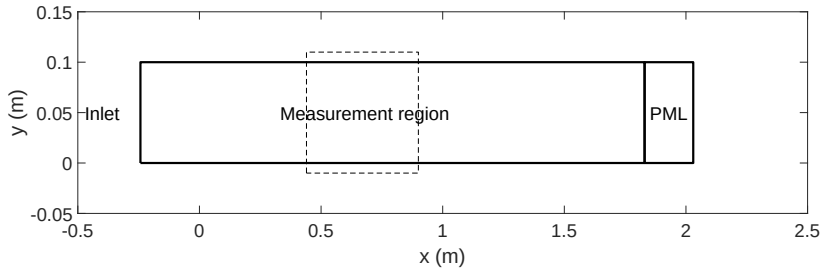

Figure 4: Empty duct geometry, containing the positions of the inlet which is at the entrance of the cloak and the measurement region in which visibility and average attenuation are calculated.

5 CONCLUSIONS

The effect of viscous and thermal losses on a acoustic cloaking design consisting of 120 small cylinders has been investigated using numerical methods. From a direct comparison of the acoustic domain pressure, losses seem to have some influence on the solution, as seen in Figure 2. But these differences do not translate into any major change in the characteristics of the averaged visibility, plotted in Figure 3. Simulations including the cloak design are performed on a two dimensional domain not taking into account the dissipative effect of the actual waveguide walls. Through a very simple study of the empty waveguide, Figure 5, the walls are expected to contribute with approximately 2.5 % attenuation of the acoustic wave, in the region of the visibility measurements. These simulations also show that the chosen height of the waveguide can have great influence on the amount of attenuation. The pressure amplitude decreases about 5 - 7 % due to viscothermal losses in the cylinders forming the cloak, while another 2.5 % is due to dissipation in the waveguide itself. These values are smaller than the 15 % of losses reported in the work by Garcia-Chocano

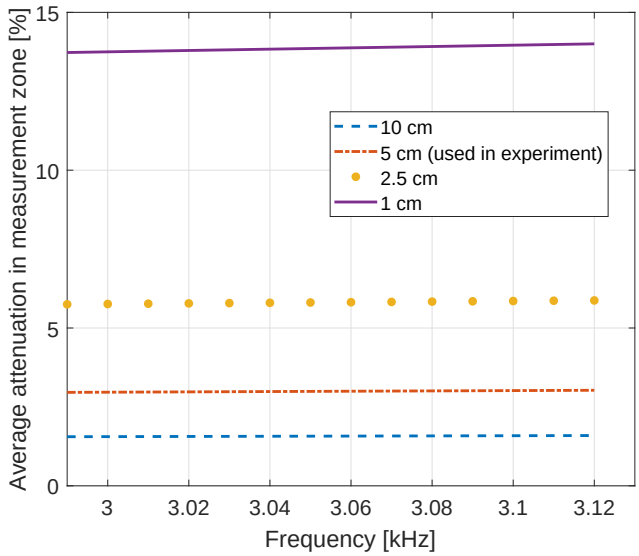

Figure 5: FEM simulations of the average attenuation in the measurement region of Figure 4, for different waveguide heights: (blue dashed) 10 cm, (red dot dash) 5 cm, (yellow dotted) 2.5 cm and (blue dashed) 1 cm.

[4]. So, it can be concluded that the additional losses measured in the experiment might be due to the setup employed. Future studies could cover full three-dimensional simulations including the wall effects, or the wall attenuation could simply be included in the incident wave to investigate its impact on the averaged visibility.

ACKNOWLEDGMENTS

J. Sánchez-Dehesa acknowledges the support by the Spanish Ministerio de Economía y Competitividad, and the European Union Fondo Europeo de Desarrollo Regional (FEDER) through Project No. TEC2014-53088-C3-1-R.

REFERENCES

[1] V. Cutanda Henríquez, V. M. García-Chocano, and J. Sánchez-Dehesa. Viscothermal losses in double-negative acoustic metamaterial. *Physical Review Applied*, 8(1):014029, 2017.

[2] V. Cutanda Henríquez, P. Risby Andersen, J. S. Jensen, P. M. Juhl, and J. Sánchez-Dehesa. A numerical model of an acoustic metamaterial using the Boundary Element Method including viscous and thermal losses. *Journal of Computational Acoustics*, 25(4):1750006, 2017.

[3] R. E. Christensen and O. Sigmund. Experimental validation of systematically designed acoustc hyperbolic meta material slab exhibiting negative refraction. *Applied Physics Letters*, 109(10):101905, 2016.

[4] V. M. García-Chocano, Sanchis L., A Díaz-Rubio, J. Martínez-Pastor, F. Cervena, R. Llopis-Pontiveros, and J. Sánchez-Dehesa. Acoustic cloak for airborne sound by inverse design. *Applied Physics Letters*, 99(7):074102, 2011.

[5] L. Sanchis, A. Håkansson, F. Cervera, and J. Sánchez-Dehesa. Acoustic interferometers based on two-dimensional arrays of ridgid cylinders in air. *Physical Review B*, 67(3):35422, 2003.

[6] J. Andkjær and O. Sigmund. Topology optimized for airborne sound. *ASME J. Vib. Acoust.*, 135:041011, 2013.

[7] J. Andkjær and O. Sigmund. Topology optimized low-contrast all-dielectric optical cloak. *Applied Physics Letters.*, 98:021112, 2011.

[8] M. D. Guild, A. Alú, and M. R. Habermann. Cancellation of acoustic scattering from an elastic sphere. *J. Acoust. Soc. Am.*, 129:1355, 2011.

[9] P. M. Morse and K. U. Ingard. *Theoretical acoustics*. McGraw-Hill, Inc, 1968.

[10] V. Cutanda Henríquez and P. M. Juhl. An axisymmetric boundary element formulation of sound wave propagation in fluids including viscous and thermal losses. *Journal of the Acoustical Society of America*, 134(5):3409, 2013.

[11] V. Cutanda Henríquez and P. M. Juhl. Implementaion of an acoustic 3D BEM with viscothermal losses. *Inter-noise, 15-18 sept, Insbruck (Austria)*, 2013.

[12] V. Cutanda Henríquez and P. M. Juhl. OpenBEM - an open source Boundary Element Method software in acoustics,. *Proceedings of the 39th International Congress on Noise Control Engineering, Inter-noise, Lisbon (Portugal)*, 2010.

[13] P. Risby Andersen, V. Cutanda Henríquez, N. Aage, and S. Marburg. Numerical acoustic models including viscous and thermal losses: Review of exsisting and new methods. *DAGA, 6-9 March, Kiel (Germany)*, 2017.

[14] M. Malinen, M. Lyly, P. Raback, A. Karkainen, and L. Karkkainen. A Finite Element Method for the modeling of thermo-viscous effects in acoustics. *Proceedings of the 4th European Congress on Computational Methods in Applied and Engineering ECCOMAS, Jyvaskyla (Finland)*, 2004.

[15] W. R. Kampinga. Viscothermal acoustics using Finite Elements. Analysis tool for engineers. *PhD thesis, University of Twente, Enchede*, 2010.

Paper C

A two dimensional acoustic tangential derivative boundary element method including viscous and thermal losses

Journal of Theoretical and Computational Acoustics
Vol. 26, No. 3 (2018) 1850036 (15 pages)

DOI: 10.1142/S2591728518500366

INTERNATIONAL ASSOCIATION
FOR MATHEMATICS AND
COMPUTERS IN SIMULATION

A Two-Dimensional Acoustic Tangential Derivative Boundary Element Method Including Viscous and Thermal Losses

P. Risby Andersen*, V. Cutanda Henríquez† and N. Aage‡

Centre for Acoustic-Mechanical Micro Systems
Technical University of Denmark, Ørsteds Plads 352
DK-2800 Kgs. Lyngby, Denmark
**prand@elektro.dtu.dk*
†*vcuhe@elektro.dtu.dk*
‡*naage@mek.dtu.dk*

S. Marburg

Institute of Vibroacoustics of Vehicles and Machines
Faculty of Mechanical Engineering, Technical University of Munich
Boltzmannstr. 15, 85748 Garching bei München, Germany
steffen.marburg@tum.de

Received 29 December 2017
Accepted 26 April 2018
Published 5 September 2018

In recent years, the boundary element method has shown to be an interesting alternative to the finite element method for modeling of viscous and thermal acoustic losses. Current implementations rely on finite-difference tangential pressure derivatives for the coupling of the fundamental equations, which can be a shortcoming of the method. This finite-difference coupling method is removed here and replaced by an extra set of tangential derivative boundary element equations. Increased stability and error reduction is demonstrated by numerical experiments.

Keywords: Boundary element method; viscous and thermal losses; acoustics.

1. Introduction

The isentropic acoustic wave equation is appropriate for modeling a vast variety of applications, but fails to give accurate solutions, especially if the acoustic domain is small and contains narrow gaps. In such situations, the effects of viscous and thermal dissipations must be considered. Two numerical approaches can be used for modeling of viscous and thermal acoustic dissipations, namely the finite element method (FEM) and the boundary

*Corresponding author.

element method (BEM). FEM implementations for arbitrary geometries rely on a direct evaluation of the full linearized Navier–Stokes equations. This was initially proposed by Bossart *et al.*,[1] realized by Malinen *et al.*[2] and later presented in different variations by Cheng *et al.*,[3] Joly *et al.*[4] and Kampinga *et al.*[5] FEM can be computationally demanding, since the loss mechanisms require proper meshing of the associated boundary layers. Further, temperature and velocity are added as extra degrees of freedom. A numerically less costly method was recently proposed by Kampinga named the sequential linearized Navier–Stokes.[6] It is realized by removing some contributions, deemed negligible after an order of magnitude analysis and thus making it possible to separately solve uncoupled scalar viscous and thermal fields. While being more cost-efficient, it is an approximation and also requires careful meshing of the viscous and thermal boundary layers.

As opposed to modeling viscous and thermal losses with FEM, BEM is an interesting alternative, avoiding cumbersome meshing of boundary layers. Early BEM implementations relied on the work by Bruneau *et al.*,[7] turned into BEM by Dokumaci[8,9] and Karra and Ben Tahar.[10] Their contributions were either having some restrictions or completely neglecting viscosity. Later, Cutanda Henríquez extended the ideas of Karra and Ben Tahar,[10] relying on the Kirchhoff's decomposition of the Navier–Stokes equations to include the effects of viscosity.[11] This approach was further developed into more general axisymmetric and three-dimensional formulations.[12–14] While recent publications have shown the capabilities of this method, tackling large complicated problems,[15,16] the method might still have some shortcomings. Especially, the coupling of the Kirchhoff's decomposition equations is troublesome. In the current formulation of Cutanda Henríquez the coupling is handled through first- and second-order tangential derivatives evaluated with the use of finite differences. While this approach works for a large range of problems, it may be problematic for interior problems at low frequency, where the acoustic pressure is nearly uniform, potentially making finite differences inaccurate. The low-frequency implications were discussed in a recent conference paper by the authors, where a combined FEM and BEM approach was presented.[17]

In the following, a new two-dimensional BEM approach is developed avoiding the use of first- and second-order finite-difference schemes in the coupling of the fundamental equations. This is shown possible by using an extra set of BEM tangential derivative equations for a more natural coupling of the equations. Finally, the new formulation will be evaluated through two simple academic test cases comparing it to the original finite-difference formulation.

2. Two-Dimensional Dissipative Boundary Element Formulation

Previous BEM implementations including the effects of viscous and thermal dissipations were based on the Kirchhoff's decomposition of the Navier–Stokes equations to achieve a form suitable for BEM discretization. The same approach is adopted in the following derivations. A large part of the present work relies on the formulation found in Ref. 12 and this work uses the same notation. In Refs. 12 and 7, the parameters (τ_a, τ_h, ϕ_a, k_a, k_h and k_v) of the Kirchhoff's decomposition are discussed in more detail.

2.1. *Kirchhoff's decomposition and boundary conditions*

The final form of the decomposed Navier–Stokes equations is given in Eqs. (1)–(3), resulting in three equations of the Helmholtz form, where p_a and p_h are the so-called acoustic and thermal pressures, respectively.[18,19] Their sum $p = p_a + p_h$ represents the total pressure. The vector $\vec{v}_n$ is the rotational part of the velocity, also known as viscous velocity. In this paper, magnitudes written with an arrow vector on top are vectorial fields, while bold letters indicate matrices. While p_a resembles an actual acoustic pressure wave, the equations containing p_h and $\vec{v}_v$ can be considered as heavily damped wave equations. k_a, k_h and k_v denote the acoustic, thermal and viscous wavenumbers, respectively:

$$\Delta p_a + k_a^2 p_a = 0, \tag{1}$$

$$\Delta p_h + k_h^2 p_h = 0, \tag{2}$$

$$\Delta \vec{v}_v + k_v^2 \vec{v}_v = 0 \quad \text{with } \nabla \cdot \vec{v}_v = 0. \tag{3}$$

Equations (1)–(3) are coupled at the boundary through boundary conditions. It is reasonable to assume isothermal boundary conditions. The heat capacity is very much higher at the boundary than in the fluid that temperature variations at the boundary can be neglected. An isothermal boundary condition can be expressed in terms of the acoustic and thermal pressures and two frequency-dependent terms τ_a and τ_h relating the acoustic and thermal pressures to the temperature fluctuations T. This results in a frequency-dependent thermal boundary layer forming at the boundary, with a thickness ranging from micrometers to millimeters in the audible frequency range. Isolating p_h in the isothermal boundary condition, Eq. (4), is discretized as,

$$T = \tau_a p_a + \tau_h p_h = 0, \tag{4}$$

which will be used as the first condition to couple the equations of Kirchhoff's decomposition. A second boundary condition states that the fluid will tend to stick to the boundaries (no-slip condition). A viscous boundary layer will form, having similar thickness as the thermal boundary layer. This boundary condition is expressed as

$$\vec{v}_b = \phi_a \nabla p_a + \phi_h \nabla p_h + \vec{v}_v, \tag{5}$$

where $\vec{v}_b$ is the boundary velocity and ϕ_a and ϕ_h are constants depending on physical parameters and frequency. For the further development, it is convenient to describe the no-slip conditions in a local boundary coordinate system:

$$v_{b,n} = \phi_a \frac{\partial p_a}{\partial n} + \phi_h \frac{\partial p_h}{\partial n} + v_{v,n}, \tag{6}$$

$$v_{b,t} = \phi_a \frac{\partial p_a}{\partial t} + \phi_h \frac{\partial p_h}{\partial t} + v_{v,t}, \tag{7}$$

with the subscripts n and t denoting the normal and tangential components to the boundary.

2.2. *Boundary element discretization*

The boundary element implementation for regular isentropic acoustic problems starts with the integral form of the harmonic Helmholtz equation:

$$C(P)p(P) = \int_\Gamma \frac{\partial G(R)}{\partial n(Q)} p(Q) d\Gamma(Q) - \int_\Gamma G(R) \frac{\partial p(Q)}{\partial n(Q)} d\Gamma(Q), \tag{8}$$

where $C(P)$ is the integral-free term. The first term on the right-hand side is the double-layer potential and the second term is the single-layer potential. P is a calculation point, Q is an integration point on the generator, $R = |Q - P|$ is the distance between calculation and integration points and $G(R)$ is the fundamental solution in free space. An $e^{i\omega t}$ time convention is assumed. It should be noted that inclusion of a source term is omitted for simplicity, but could be added as an extra term. Meshing and collocation of the Helmholtz integral equation in matrix form is given by

$$\mathbf{Cp} = \mathbf{Hp} - \mathbf{B}\frac{\partial \mathbf{p}}{\partial n}, \tag{9}$$

where $\mathbf{C}$ is a diagonal matrix containing the integral-free term, $\mathbf{H}$ and $\mathbf{B}$ are the discretized double- and single-layer potential matrices, respectively, and $\mathbf{p}$ and $\frac{\partial \mathbf{p}}{\partial n}$ are vectors. A more compact notation with $\mathbf{A} = \mathbf{H} - \mathbf{C}$ will be used in the following development. Since the Kirchhoff's decomposition produces equations formally equivalent to the Helmholtz wave equation, it is straightforward to apply BEM to Eqs. (1)–(3) using collocation and replacing the isentropic wavenumber k with k_a, k_h and k_v:

$$\mathbf{A}_a\mathbf{p}_a - \mathbf{B}_a\frac{\partial \mathbf{p}_a}{\partial n} = \mathbf{0}, \tag{10}$$

$$\mathbf{A}_h\mathbf{p}_h - \mathbf{B}_h\frac{\partial \mathbf{p}_h}{\partial n} = \mathbf{0}, \tag{11}$$

$$\mathbf{A}_v\mathbf{v}_{v,x} - \mathbf{B}_v\frac{\partial \mathbf{v}_{v,x}}{\partial n} = \mathbf{0}, \tag{12}$$

$$\mathbf{A}_v\mathbf{v}_{v,y} - \mathbf{B}_v\frac{\partial \mathbf{v}_{v,y}}{\partial n} = \mathbf{0}, \tag{13}$$

where Eq. (3) is split into its Cartesian components forming Eqs. (12) and (13). Note that we here and in the following limit the formulation to two dimensions (x, y) for simplicity. In two dimensions, the fundamental solution is given by $G(R) = \frac{1}{2\pi}K_0(ikR)$ where $K_j(ikR)$ is the modified Bessel function of the second kind of order j. The argument of the fundamental solution is the imaginary unit i and the wavenumber k can be either acoustic, thermal or viscous.

2.3. *Coupling of equations*

The previous boundary element implementations with losses make use of finite differences to couple the fundamental equation set. The new approach presented here utilizes the boundary element itself to estimate tangential derivatives. Taking the tangential derivative

of Eq. (8) with respect to the collocation point yields

$$C(P)\frac{\partial p(P)}{\partial t(P)} = \int_\Gamma \frac{\partial^2 G(R)}{\partial t(P)\partial n(Q)} p(Q) d\Gamma(Q) - \int_\Gamma \frac{\partial G(R)}{\partial t(P)} \frac{\partial p(Q)}{\partial n(Q)} d\Gamma(Q), \tag{14}$$

thus allowing for the evaluation of the tangential derivative of the pressure on the collocation points from boundary pressures $p(Q)$ and their normal derivatives $\frac{\partial p(Q)}{\partial n}$. Equation (14) contains second derivatives of the fundamental solution. A similar situation arises when dealing with irregular frequencies for exterior problems using the Burton–Miller formulation, which contains double normal derivative kernels that are said to be hypersingular and require special treatment.[20] However, the integrals arising from the tangential derivative equations are Cauchy principal value (CPV) integrals. The kernel description can for example be found in the work by Gallego and Martínez-Castro.[21] The viscothermal implementation presented here relies on an adaptive integration scheme for the evaluation of near-singular integrals arising in the case of narrow gaps,[22] but also for the evaluation of the CPV integrals. Initial convergence studies have shown that this approach is feasible for the evaluation of the tangential kernels.

A second set of discretized equations can now be formed containing the tangential derivative kernels:

$$\mathbf{C}\frac{\partial \mathbf{p}_a}{\partial t} = \mathbf{A}_{a,t}\mathbf{p}_a - \mathbf{B}_{a,t}\frac{\partial \mathbf{p}_a}{\partial n}, \tag{15}$$

$$\mathbf{C}\frac{\partial \mathbf{p}_h}{\partial t} = \mathbf{A}_{h,t}\mathbf{p}_h - \mathbf{B}_{h,t}\frac{\partial \mathbf{p}_h}{\partial n}, \tag{16}$$

$$\mathbf{C}\frac{\partial \mathbf{v}_{v,x}}{\partial t} = \mathbf{A}_{v,t}\mathbf{v}_{v,x} - \mathbf{B}_{v,t}\frac{\partial \mathbf{v}_{v,x}}{\partial n}, \tag{17}$$

$$\mathbf{C}\frac{\partial \mathbf{v}_{v,y}}{\partial t} = \mathbf{A}_{v,t}\mathbf{v}_{v,y} - \mathbf{B}_{v,t}\frac{\partial \mathbf{v}_{v,y}}{\partial n}. \tag{18}$$

It is possible to describe the no-slip condition in terms of the discretized equations by isolating $\frac{\partial \mathbf{p}_a}{\partial n}$,$\frac{\partial \mathbf{p}_h}{\partial n}$, $\frac{\partial \mathbf{p}_a}{\partial t}$ and $\frac{\partial \mathbf{p}_h}{\partial t}$ in Eqs. (10), (11), (15) and (16), respectively. The boundary condition equations, i.e. Eqs. (6) and (7), can then be described by

$$\mathbf{v}_{b,n} = \phi_a(\mathbf{B}_a^{-1}\mathbf{A}_a)\mathbf{p}_a + \phi_h(\mathbf{B}_h^{-1}\mathbf{A}_h)\mathbf{p}_h + \mathbf{v}_{v,n}, \tag{19}$$

$$\mathbf{v}_{b,t} = \phi_a\mathbf{C}^{-1}(\mathbf{A}_{a,t}\mathbf{p}_a - \mathbf{B}_{a,t}((\mathbf{B}_a^{-1}\mathbf{A}_a)\mathbf{p}_a)) + \phi_h\mathbf{C}^{-1}(\mathbf{A}_{h,t}\mathbf{p}_h - \mathbf{B}_{h,t}((\mathbf{B}_h^{-1}\mathbf{A}_h)\mathbf{p}_h)) + \mathbf{v}_{v,t}. \tag{20}$$

Isolating p_h in the isothermal boundary condition (4),

$$\mathbf{p}_h = -\frac{\tau_a}{\tau_h}\mathbf{p}_a, \tag{21}$$

the thermal pressure can be eliminated from Eqs. (19) and (20). Finally, the boundary conditions of the discretized equations can be stated as

$$\mathbf{v}_{b,n} = \mathbf{E}_n\mathbf{p}_a + \mathbf{v}_{v,n}, \tag{22}$$

$$\mathbf{v}_{b,t} = \mathbf{E}_t\mathbf{p}_a + \mathbf{v}_{v,t}, \tag{23}$$

where

$$\mathbf{E}_n = \phi_a(\mathbf{B}_a^{-1}\mathbf{A}_a) - \phi_h\frac{\tau_a}{\tau_h}(\mathbf{B}_h^{-1}\mathbf{A}_h), \tag{24}$$

$$\mathbf{E}_t = \phi_a[\mathbf{C}^{-1}(\mathbf{A}_{a,t} - \mathbf{B}_{a,t}(\mathbf{B}_a^{-1}\mathbf{A}_a))] - \phi_h\frac{\tau_a}{\tau_h}[\mathbf{C}^{-1}(\mathbf{A}_{h,t} - \mathbf{B}_{h,t}(\mathbf{B}_h^{-1}\mathbf{A}_h))]. \tag{25}$$

2.4. *Null-divergence of the viscous velocity*

The viscous velocity forms a rotational vector field, meaning that $\nabla \cdot \vec{v}_v = 0$ must be fulfilled. This is ensured through the null-divergence in a normal and tangential coordinate system (note that the tangential direction only has a single component in a 2D problem):

$$\frac{\partial \mathbf{v}_{v,n}}{\partial n} + \frac{\partial \mathbf{v}_{v,t}}{\partial t} = 0, \tag{26}$$

which will require a relation between local and global quantities on the boundary, achieved in an all-geometry approach for the individual discrete nodes by

$$\mathbf{v}_{v,n} = \mathbf{n}_x \circ \mathbf{v}_{v,x} + \mathbf{n}_y \circ \mathbf{v}_{v,y}, \tag{27}$$

$$\mathbf{v}_{v,t} = \mathbf{t}_x \circ \mathbf{v}_{v,x} + \mathbf{t}_y \circ \mathbf{v}_{v,y}, \tag{28}$$

where $\circ$ is the element-wise Hadamard product (see Appendix A) and $\mathbf{n}_x$, $\mathbf{n}_y$, $\mathbf{t}_x$ and $\mathbf{t}_y$ are the Cartesian components of the normal and tangential vectors at each node. The transform of the viscous velocity back to the Cartesian coordinates is

$$\mathbf{v}_{v,x} = \mathbf{n}_x \circ \mathbf{v}_{v,n} + \mathbf{t}_x \circ \mathbf{v}_{v,t}, \tag{29}$$

$$\mathbf{v}_{v,y} = \mathbf{n}_y \circ \mathbf{v}_{v,n} + \mathbf{t}_y \circ \mathbf{v}_{v,t}. \tag{30}$$

The goal is now to establish an expression for each of the terms in Eq. (26) using the discretized equations, containing only local normal and tangential components of the viscous velocity. This requires taking the derivative of Eqs. (27) and (28) with respect to the normal and tangential components, respectively. Doing so yields

$$\frac{\partial \mathbf{v}_{v,n}}{\partial n} = \mathbf{n}_x \circ \frac{\partial \mathbf{v}_{v,x}}{\partial n} + \mathbf{n}_x \circ \frac{\partial \mathbf{v}_{v,y}}{\partial n}, \tag{31}$$

$$\frac{\partial \mathbf{v}_{v,t}}{\partial t} = \mathbf{t}_x \circ \frac{\partial \mathbf{v}_{v,x}}{\partial t} + \mathbf{t}_y \circ \frac{\partial \mathbf{v}_{v,y}}{\partial t}. \tag{32}$$

By isolating $\frac{\partial \mathbf{v}_{v,x}}{\partial n}$ and $\frac{\partial \mathbf{v}_{v,y}}{\partial n}$ in Eqs. (12) and (13) and substituting into Eq. (31), we obtain

$$\frac{\partial \mathbf{v}_{v,n}}{\partial n} = \mathbf{n}_x \circ (\mathbf{B}_v^{-1}\mathbf{A}_v\mathbf{v}_{v,x}) + \mathbf{n}_y \circ (\mathbf{B}_v^{-1}\mathbf{A}_v\mathbf{v}_{v,y}). \tag{33}$$

Using Eqs. (29) and (30) to describe the viscous velocity in terms of the normal and tangential components, Eq. (33) becomes

$$\frac{\partial \mathbf{v}_{v,n}}{\partial n} = \mathbf{n}_x \circ (\mathbf{B}_v^{-1}\mathbf{A}_v(\mathbf{n}_x \circ \mathbf{v}_{v,n} + \mathbf{t}_x \circ \mathbf{v}_{v,t})) + \mathbf{n}_y \circ (\mathbf{B}_v^{-1}\mathbf{A}_v(\mathbf{n}_y \circ \mathbf{v}_{v,n} + \mathbf{t}_y \circ \mathbf{v}_{v,t})). \tag{34}$$

Applying the properties of the Hadamard product for diagonal terms, the terms in Eq. (34) can be rearranged so that

$$\frac{\partial \mathbf{v}_{v,n}}{\partial n} = \mathbf{N}_1 \circ (\mathbf{B}_v^{-1}\mathbf{A}_v)\mathbf{v}_{v,n} + \mathbf{N}_2 \circ (\mathbf{B}_v^{-1}\mathbf{A}_v)\mathbf{v}_{v,t}, \tag{35}$$

where

$$\mathbf{N}_1 = \mathbf{n}_x\mathbf{n}_x^T + \mathbf{n}_y\mathbf{n}_y^T, \tag{36}$$

$$\mathbf{N}_2 = \mathbf{n}_x\mathbf{t}_x^T + \mathbf{n}_y\mathbf{t}_y^T. \tag{37}$$

The result of Eq. (35) will be used later to ensure that the null-divergence condition is fulfilled. Proceeding with the second term in Eq. (26), a connection between the discretized equations and $\frac{\partial \mathbf{v}_{v,t}}{\partial t}$ is established. By isolating $\frac{\partial \mathbf{v}_{v,x}}{\partial t}$ and $\frac{\partial \mathbf{v}_{v,y}}{\partial t}$ in Eqs. (17) and (18) and substituting the result into Eq. (28), an expression for the tangential derivative of the tangential viscous velocity is found:

$$\frac{\partial \mathbf{v}_{v,t}}{\partial t} = \mathbf{t}_x \circ \left(\mathbf{C}^{-1}\left(\mathbf{A}_{v,t}\mathbf{v}_{v,x} - \mathbf{B}_{v,t}\frac{\partial \mathbf{v}_{v,x}}{\partial n}\right)\right) + \mathbf{t}_y \circ \left(\mathbf{C}^{-1}\left(\mathbf{A}_{v,t}\mathbf{v}_{v,y} - \mathbf{B}_{v,t}\frac{\partial \mathbf{v}_{v,y}}{\partial n}\right)\right). \tag{38}$$

The Cartesian viscous quantities can be transformed into the local form by combining Eqs. (29), (30), (12) and (13) into

$$\begin{aligned}\frac{\partial \mathbf{v}_{v,t}}{\partial t} = {} & \mathbf{t}_x \circ (\mathbf{C}^{-1}(\mathbf{A}_{v,t}(\mathbf{n}_x \circ \mathbf{v}_{v,n} + \mathbf{t}_x \circ \mathbf{v}_{v,t}) - \mathbf{B}_{v,t}(\mathbf{B}_v^{-1}\mathbf{A}_v)(\mathbf{n}_x \circ \mathbf{v}_{v,n} + \mathbf{t}_x \circ \mathbf{v}_{v,t}))) \\ & + \mathbf{t}_y \circ (\mathbf{C}^{-1}(\mathbf{A}_{v,t}(\mathbf{n}_y \circ \mathbf{v}_{v,n} + \mathbf{t}_y \circ \mathbf{v}_{v,t}) - \mathbf{B}_{v,t}(\mathbf{B}_v^{-1}\mathbf{A}_v)(\mathbf{n}_y \circ \mathbf{v}_{v,n} + \mathbf{t}_y \circ \mathbf{v}_{v,t}))).\end{aligned} \tag{39}$$

Rearranging the terms and using the Hadamard product properties, the following equation is obtained:

$$\frac{\partial \mathbf{v}_{v,t}}{\partial t} = \mathbf{N}_3 \circ (\mathbf{C}^{-1}(\mathbf{A}_{v,t} - \mathbf{B}_{v,t}(\mathbf{B}_v^{-1}\mathbf{A}_v)))\mathbf{v}_{v,n} + \mathbf{N}_4 \circ (\mathbf{C}^{-1}(\mathbf{A}_{vt} - \mathbf{B}_{vt}(\mathbf{B}_v^{-1}\mathbf{A}_v)))\mathbf{v}_{v,t}, \tag{40}$$

where

$$\mathbf{N}_3 = \mathbf{t}_x\mathbf{n}_x^T + \mathbf{t}_y\mathbf{n}_y^T, \tag{41}$$

$$\mathbf{N}_4 = \mathbf{t}_x\mathbf{t}_x^T + \mathbf{t}_y\mathbf{t}_y^T. \tag{42}$$

The result of the normal and tangential derivatives of the local viscous velocity components, Eqs. (35) and (40), is substituted into the local form of the null-divergence, Eq. (26), forming

$$(\mathbf{N}_1 \circ \mathbf{V})\mathbf{v}_{v,n} + (\mathbf{N}_2 \circ \mathbf{V})\mathbf{v}_{v,t} + (\mathbf{N}_3 \circ \mathbf{T})\mathbf{v}_{v,n} + (\mathbf{N}_4 \circ \mathbf{T})\mathbf{v}_{v,t} = 0, \tag{43}$$

where $\mathbf{V}$ and $\mathbf{T}$ are defined as

$$\mathbf{V} = \mathbf{B}_v^{-1}\mathbf{A}_v, \tag{44}$$

$$\mathbf{T} = \mathbf{C}^{-1}(\mathbf{A}_{v,t} - \mathbf{B}_{v,t}\mathbf{V}). \tag{45}$$

The result of Eq. (43) will be used in the following to ensure that the viscous velocity has null-divergence.

2.5. *System of equations and boundary quantities*

It is now possible to establish a system of equations containing boundary normal and tangential velocities and the acoustic pressure. Isolating $\mathbf{v}_{v,n}$ and $\mathbf{v}_{v,t}$ in Eqs. (43) and (23), respectively, and substituting them into Eq. (22) yields the final system of equations:

$$\begin{aligned}&[[(\mathbf{N}_1 \circ \mathbf{V}) + (\mathbf{N}_3 \circ \mathbf{T})]\mathbf{E}_n + [(\mathbf{N}_2 \circ \mathbf{V}) + (\mathbf{N}_4 \circ \mathbf{T})]\mathbf{E}_t]\mathbf{p}_a \\ &\quad = [(\mathbf{N}_1 \circ \mathbf{V}) + (\mathbf{N}_3 \circ \mathbf{T})]\mathbf{v}_{b,n} + [(\mathbf{N}_2 \circ \mathbf{V}) + (\mathbf{N}_4 \circ \mathbf{T})]\mathbf{v}_{b,t}, \end{aligned} \tag{46}$$

which allows for applying boundary velocity conditions and solving for the nodal acoustic pressures $\mathbf{p}_a$. The total pressure can be described as the sum of the acoustic and thermal pressures, by assuming isothermal boundary conditions:

$$\mathbf{p} = \mathbf{p}_a + \mathbf{p}_h = \mathbf{p}_a - \frac{\tau_a}{\tau_h}\mathbf{p}_a. \tag{47}$$

The normal and tangential viscous velocities can be found by rearranging Eqs. (22) and (23), so that

$$\mathbf{v}_{v,n} = \mathbf{E}_n\mathbf{p}_a - \mathbf{v}_{b,n}, \tag{48}$$

$$\mathbf{v}_{v,t} = \mathbf{E}_t\mathbf{p}_a - \mathbf{v}_{b,t}. \tag{49}$$

The evaluation of field points can be done by following the approach in Ref. 12. The expression using the finite-difference approach originally developed by Cutanda Henríquez, is reproduced here for comparison:

$$\begin{aligned}&\left[\phi_a\mathbf{B}_a^{-1}\mathbf{A}_a - \phi_h\mathbf{B}_h^{-1}\mathbf{A}_h\frac{\tau_a}{\tau_h} + \left(\phi_a - \frac{\tau_a}{\tau_h}\phi_h\right) \times (\mathbf{N}_1 \circ (\mathbf{B}_v^{-1}\mathbf{A}_v))^{-1}\right. \\ &\qquad \left. \times (\mathbf{N}_2 \circ (\mathbf{B}_v^{-1}\mathbf{A}_v\mathbf{D}\mathbf{T}_1) + \mathbf{D}\mathbf{T}_2)\right]\mathbf{p}_a \\ &\quad = \mathbf{v}_{b,n} + [\mathbf{N}_1 \circ (\mathbf{B}_v^{-1}\mathbf{A}_v)]^{-1} \times [\mathbf{N}_2 \circ (\mathbf{B}_v^{-1}\mathbf{A}_v) + \mathbf{D}\mathbf{T}_1]\mathbf{v}_{b,t}, \end{aligned} \tag{50}$$

where $\mathbf{DT}_1$ and $\mathbf{DT}_2$ denote the first and second tangential surface finite-difference matrices, respectively. Equation (50) is developed by taking the tangential derivative of the boundary condition, Eq. (7), whereas the new approach presented in this paper achieves this goal through a set of tangential boundary element matrices, Eq. (38). As a consequence, the use of finite difference but also the evaluation of second tangential pressure derivatives are avoided.

3. Test Cases

Only few analytical solutions are available for testing of acoustic viscothermal implementations. In the first example, the implementation will be compared with an analytical solution

for an oscillating cylinder.[23] This example considers only viscosity, but this is not an important limitation since it is the implementation of viscosity that poses a challenge in BEM with losses. Thermal losses are easily removed from the formulation by neglecting the terms containing thermal quantities in $\mathbf{E}_n$ and $\mathbf{E}_t$. The second example is a narrow duct. This example highlights a problematic behavior that might be present in the finite-difference implementation for some cases.

3.1. *Discretization*

One requirement when dealing with the tangential derivative integration kernels is the need for C^1 continuity at the collocation points. This can be achieved by using discontinuous elements. Discontinuous elements are also known to perform well for boundary element implementations.[24] In order to evaluate the effect of the new tangential derivative formulation on equal footing, the finite-difference formulation and the new formulation will use the same boundary element matrices created using discontinuous quadratic elements. In the second example, however, the finite-difference implementation uses the full approach found in Ref. 12, with regular continuous quadratic Lagrangian elements.

3.2. *Oscillating infinite cylinder*

The infinite cylinder geometry is shown in Fig. 1. The radius R is set to 1 m and the amplitude of oscillation is 1 m/s. A relative error measure will be defined as,

$$\epsilon_p = \sum_{j=1}^{N_n} \frac{|p_j - p_{j,\text{ref}}|}{|p_{j,\text{ref}}|}, \tag{51}$$

with the index j denoting the individual nodal solutions, N_n is the total number of nodes and $p_{j,\text{ref}}$ is the corresponding reference solution. Figure 2 shows the convergence of the pressure

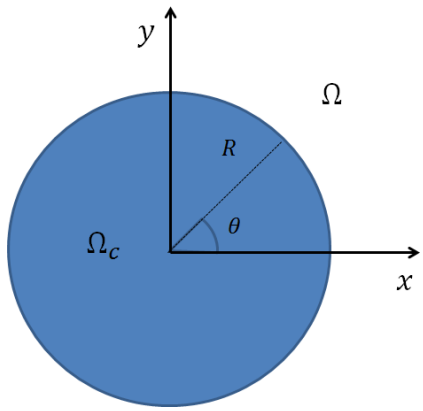

Fig. 1. Geometry of the infinite cylinder.

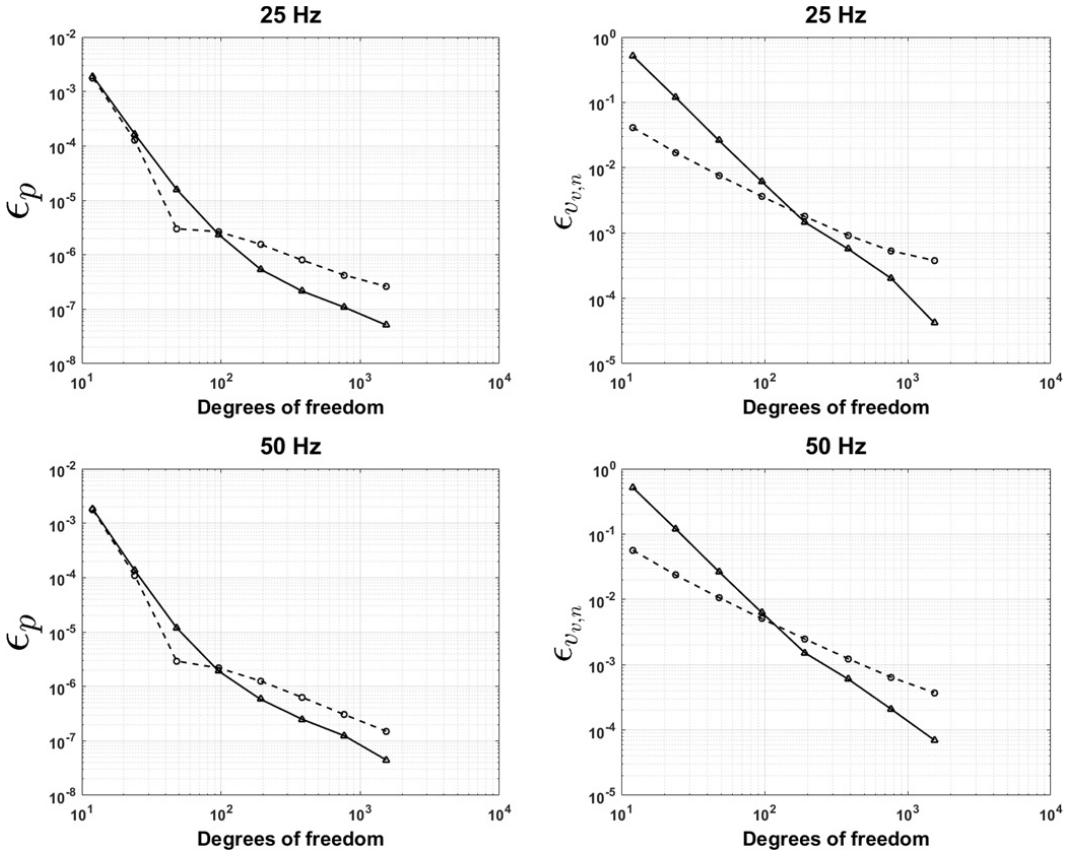

Fig. 2. Convergence plots at 25 Hz and 50 Hz of the new and existing BEM formulations with losses for the case of an infinite oscillating cylinder. Both pressure and normal viscous velocity errors are plotted for TD-BEM (solid) and FDD-BEM (dashed).

and the normal viscous velocity, comparing the new tangential derivative boundary element method (TD-BEM) and the finite-difference derivative boundary element method (FDD-BEM) implementations at 25 Hz and 50 Hz. These frequencies where chosen to avoid any influence from irregular frequencies. Higher frequency solutions could be obtained by using for example the combined Helmholtz integral equation formulation,[25] but this is considered beyond the scope of the paper. The normal viscous velocity is usually much smaller than the corresponding tangential component and more difficult to compute accurately. The error in pressure is similar for the two implementations above approximately 100 degrees of freedom, but higher mesh densities seem to favor TD-BEM. The convergence situation is slightly different in the case of the normal viscous velocity. In this case, TD-BEM experiences a larger error for low degrees of freedom, as compared to FDD-BEM, but for higher mesh densities TD-BEM is again a better choice. It is not fully understood why TD-BEM experiences a

higher error at low mesh densities. A plausible explanation could be related to the use of BEM to estimate the tangential derivatives of the viscous velocity, which might require more elements to be captured appropriately.

3.3. *Traveling wave in narrow duct*

As a second test case, a traveling wave in a narrow duct is considered. Approximate analytical solutions for this case exist, that are applicable in the extreme case of very narrow or wide tubes. To highlight a problematic behavior of FDD-BEM, the case of slightly overlapping boundary layer is studied, therefore an FEM solution with a very fine mesh is chosen as a reference. The geometry is shown in Fig. 3. The left end of the duct is excited with a normal boundary velocity with an amplitude of $1/(\rho c)$, where ρ is the density and c is the speed of sound for air. The other end of the duct is fitted with an impedance of value ρc. For isentropic acoustic problems this would resemble a fully absorbing boundary, but this is not necessarily true when the duct is narrow and the boundary layers fill up most of the domain. The reference FEM solution is implemented in COMSOL Multiphysics with the same boundary conditions and approximately 300,000 degrees of freedom, using an equally spaced structured quadrilateral mesh. The boundary layers are covered with about 50 elements in the direction perpendicular to the boundary. To ensure similar conditions in the Kirchhoff's decomposition and the COMSOL implementation, simulations were carried out assuming an ideal gas and no flow. The length of the duct, L, will be five times the viscous boundary layer thickness, δ_v, which for air is $2.21/\sqrt{f}$ (mm),[18] with f being the frequency of the oscillation. The pressure magnitudes are plotted in Fig. 4 along the boundary in the x-direction for three different duct heights, h. The heights are half, equal and two times the viscous boundary layer thickness. Simulations were carried out at 2 kHz, meaning that the wavelength is much larger than the computational domain, resulting in a relatively uniform pressure. It is seen how FDD-BEM fails to give accurate solutions, especially when the height is equal to the viscous boundary layer thickness. This result is invoked by using slightly smaller elements on the top and bottom parts of the duct compared to the sides (30 elements on the top and bottom parts and five elements on the sides). To further investigate this behavior, the worst case with $h = \delta_v$ is tested with different numbers of elements. The sides of the duct are fixed to five elements on each boundary, and the top and bottom boundaries keep the same element count, but with varying size. The error measure of

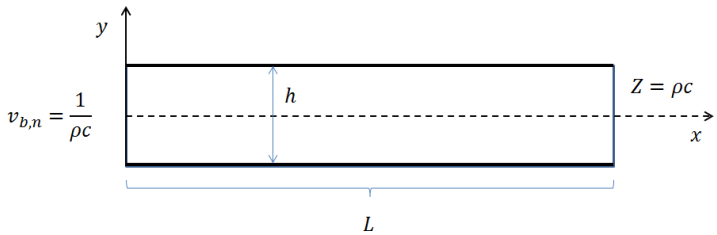

Fig. 3. Narrow duct geometry and boundary conditions.

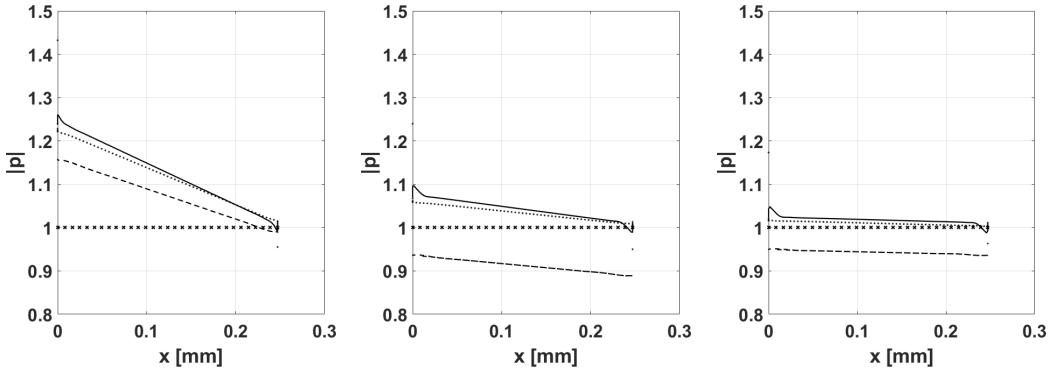

(a) (b) (c)

Fig. 4. Numerical solution at 2 kHz for narrow duct test case. The pressure magnitudes are plotted as a function of the x-coordinate of the boundary for FDD-BEM (dashed), viscothermal FEM (dotted), isentropic BEM (crosses) and TD-BEM (solid) simulations. The boundary element formulations use a mesh consisting of five elements on the side and 30 elements on the top and bottom of the duct, while the reference FEM result is calculated in the FEM software COMSOL Multiphysics using 300,000 degrees of freedom. The plots correspond to (a) $h = \delta_v/2$, (b) $h = \delta_v$ and (c) $h = 2\delta_v$.

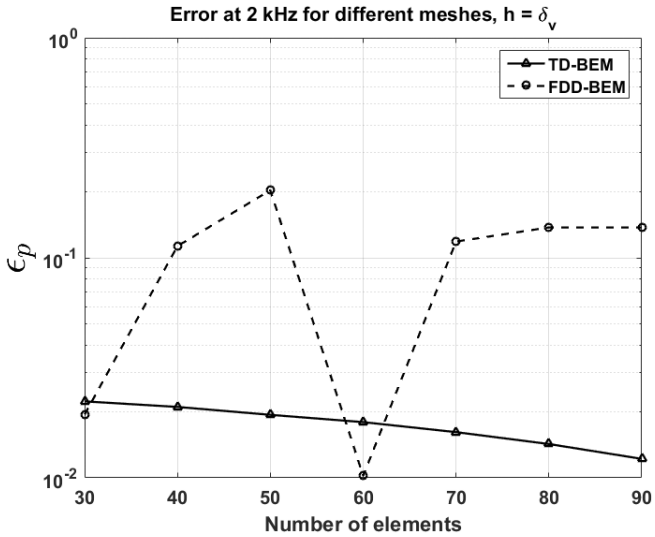

Fig. 5. Comparison of TD-BEM and FDD-BEM in terms of pressure errors in the narrow duct for different mesh configurations. Simulations are conducted at 2 kHz and the height of the duct is equal to the length of one viscous boundary layer.

Eq. (51) is used, but with the FEM solution as a reference. The results are shown in Fig. 5, where the total number of elements in the geometry is ranging from 30 to 90. Surprisingly, FDD-BEM shows an initial low error but a rapid error increase followed by a low error at 60 elements, recovering the high error at higher element counts. In the 60-element geometry,

all elements, including those on the lid, are of equal size. This means that FDD-FEM is more likely to behave with low errors, for a controlled environment with elements of equal size. This is also the case for the oscillating infinite cylinder. It appears that FDD-BEM might result in instability problems if the element sizes are dissimilar and the pressure is nearly uniform, as seen in the example. On the other hand, the new TD-BEM shows a much more stable error response to the change in element size.

4. Conclusions

A new approach to the numerical implementation of the coupling of the Kirchhoff's decomposition describing the propagation of sound waves with viscous and thermal losses is shown possible through development of an extra set of tangential boundary element equations. The new formulation completely removes finite differences as a coupling method. This leads to an improvement over the previous BEM implementation with losses. The method is compared to an earlier implementation through a simple convergence study of an infinite cylinder, showing that for higher element counts the new method can be expected to give slightly lower errors. Coarser meshes might lead to a larger error in the viscous velocity computation. In the second example, a narrow duct, the original finite-difference implementation presents some instability issues, leading to an unwanted behavior when element sizes are different. On the other hand, the presented new approach shows a much more stable error behavior. There exists a hope that the new coupling concept can be extended to three dimensions, where the use of tangential finite-difference derivatives is more cumbersome.

References

1. R. Bossart, N. Joly and M. Bruneau, Methods for numerical modeling of acoustic fields in a thermoviscous fluid, in *Proc. 6th French Congr. Acoustics* (2002), pp. 411–414.
2. M. Malinen, M. Lyly, P. Raback, A. Karkkainen and L. Karkkainen, A finite element method for the modeling of thermo-viscous effects in acoustics, in *Proc. 4th European Congr. Computational Methods in Applied and Engineering* (2004), pp. 1–12.
3. L. Cheng, R. D. White and K. Grosh, Three-dimensional viscous finite element formulation for acoustic fluid-structure interaction, *Comput. Methods Appl. Mech. Eng.* **197** (2008) 4160–4172.
4. N. Joly, M. Bruneau and R. Bossart, Coupled equations for particle velocity and temperature variation as the fundamental formulation of linear acoustics in thermo-viscous fluids at rest, *Acta Acust. United With Acust.* **92** (2006) 202–209.
5. W. R. Kampinga, Y. H. Wijnant and A. de Boer, Performance of several viscothermal acoustic finite elements, *Acta Acust. United With Acust.* **96** (2010) 115–124.
6. W. R. Kampinga, Viscothermal acoustics using finite elements: Analysis tool for engineers, PhD thesis, University of Twente, Enschede (2010).
7. M. Bruneau, Ph. Herzog, J. Kergomard and J. D. Polak, General formulation of the dispersion equation in bounded visco-thermal fluid, and application to some simple geometries, *Wave Motion* **11** (1988) 441–451.
8. E. Dokumaci, An integral equation formulation for boundary element analysis of acoustic radiation problems in viscous fluids, *J. Sound Vib.* **147** (1991) 335–348.
9. E. Dokumaci, Prediction of the effects of entropy fluctuations on sound radiation from vibrating bodies using an integral equation approach, *J. Sound Vib.* **186** (1995) 805–819.

10. C. Karra and M. Ben Tahar, An integral equation formulation for boundary element analysis of propagation in viscothermal fluids, *J. Acoust. Soc. Am.* **102** (1997) 1311–1318.
11. V. Cutanda Henríquez, Numerical transducer modeling, PhD thesis, Technical University of Denmark, Lyngby (2002).
12. V. Cutanda Henríquez and P. M. Juhl, An axisymmetric boundary element formulation of sound wave propagation in fluids including viscous and thermal losses, *J. Acoust. Soc. Am.* **134** (2013) 3409–3418.
13. V. Cutanda Henríquez and P. M. Juhl, Implementation of an acoustic 3D BEM with visco-thermal losses, in *Proc. Internoise 2013*: *Noise Control for Quality of Life* (2013).
14. V. Cutanda Henríquez and P. M. Juhl, Verification of an acoustic 3D BEM with visco-thermal losses, in *Proc. Internoise 2013*: *Noise Control for Quality of Life* (2013).
15. V. Cutanda Henríquez, P. R. Andersen, J. S. Jensen, P. M. Juhl and J. Sánchez-Dehesa, A numerical model of an acoustic metamaterial using the boundary element method including viscous and thermal losses, *J. Comput. Acoust.* **25** (2017) 1750006.
16. V. Cutanda Henríquez, V. M. Garca-Chocano and J. Sánchez-Dehesa, Viscothermal losses in double-negative acoustic metamaterials, *Phys. Rev. Appl.* **8** (2017) 014029.
17. P. R. Andersen, V. Cutanda Henríquez, N. Aage and S. Marburg, Numerical acoustic models including viscous and thermal losses: Review of existing and new methods, in *Proc. DAGA* (2017).
18. P. M. Morse and K. U. Ingard, *Theoretical Acoustics* (McGraw-Hill, 1968).
19. A. D. Pierce, *Acoustics*: *An Introduction to Its Physical Principles and Applications* (McGraw-Hill, New York, 1981).
20. A. J. Burton and G. F. Miller, The application of integral equation methods to the numerical solution of some exterior boundary-value problems, *Proc. R. Soc. Lond. A* **323** (1971) 201–210.
21. R. Gallego and A. E. Martínez-Castro, Boundary integral equation for tangential derivative of flux in Laplace and Helmholtz equations, *Int. J. Numer. Methods Eng.* **66** (2006) 343–363.
22. V. Cutanda Henríquez, P. M. Juhl and F. Jacobsen, On the modeling of narrow gaps using the standard boundary element method, *J. Acoust. Soc. Am.* **109** (2001) 1296–1303.
23. L. P. Blinova and V. N. Kozhin, Radiation of a cylinder oscillating in a viscous medium, *Izv. Akad. Nauk SSSR, Mekh. Zirdk. Gaza* **5**(1) (1970) 121–126 [*Fluid Dyn.* **5**(1) (1970) 107–111].
24. S. Marburg and S. Schneider, Influence of element types on numerical error for acoustic boundary elements, *J. Comput. Acoust.* **11**(3) (2003) 363–386.
25. H. A. Schenck, Improved integral formulation for acoustic radiation problems, *J. Acoust. Soc. Am.* **44** (1971) 41–58.
26. R. A. Beezer, in *A First Course in Linear Algebra* (Congruent Press, 2010), pp. 900–901.

Appendix A. The Hadamard Product

The Hadamard product (defined by $\circ$) is used extensively in the paper. This Appendix briefly discusses its definition and properties for diagonal matrices. The Hadamard product is defined as the entry-wise product of two equally sized matrices. If $\mathbf{A}$ and $\mathbf{B}$ are two $m \times n$ matrices, the Hadamard product is given by

$$[\mathbf{A} \circ \mathbf{B}]_{i,j} = [\mathbf{A}]_{i,j}[\mathbf{B}]_{i,j}, \tag{A.1}$$

where i and j are the row and column indices, respectively. If $\mathbf{D}$ and $\mathbf{E}$ are diagonal matrices, having sizes $m \times m$ and $n \times n$, respectively, then one of the properties of the Hadamard

product is[26]

$$\mathbf{D}(\mathbf{A} \circ \mathbf{B})\mathbf{E} = (\mathbf{DAE}) \circ \mathbf{B} = (\mathbf{DA}) \circ (\mathbf{BE}), \tag{A.2}$$

from which it can be deduced that

$$\mathbf{D}_1\mathbf{F}\mathbf{D}_2 = (\mathbf{d}_1\mathbf{d}_2^T) \circ \mathbf{F}, \tag{A.3}$$

where $\mathbf{D}_1$ and $\mathbf{D}_2$ are diagonal matrices of size $m \times m$ and $\mathbf{F}$ is a matrix of the same size. In Eq. (A.3), $\mathbf{d}_1$ and $\mathbf{d}_2$ are m-sized column vectors, created from the diagonals of $\mathbf{D}_1$ and $\mathbf{D}_2$, respectively. The relation (A.3) is used several times in the paper.

Paper D

A three-dimensional acoustic Boundary Element Method formulation with viscous and thermal losses based on shape function derivatives

Journal of Theoretical and Computational Acoustics
Vol. 26, No. 3 (2018) 1850039 (15 pages)

DOI: 10.1142/S2591728518500391

INTERNATIONAL ASSOCIATION
FOR MATHEMATICS AND
COMPUTERS IN SIMULATION

A Three-Dimensional Acoustic Boundary Element Method Formulation with Viscous and Thermal Losses Based on Shape Function Derivatives

V. Cutanda Henríquez* and P. Risby Andersen†
Centre for Acoustic-Mechanical Micro Systems
Technical University of Denmark, Ørsteds Plads
Building 352, DK-2800, Kgs. Lyngby, Denmark
*vcuhe@elektro.dtu.dk
†prand@elektro.dtu.dk

Received 8 January 2018
Accepted 26 April 2018
Published 5 September 2018

Sound waves in fluids are subject to viscous and thermal losses, which are particularly relevant in the so-called viscous and thermal boundary layers at the boundaries, with thicknesses in the micrometer range at audible frequencies. Small devices such as acoustic transducers or hearing aids must then be modeled with numerical methods that include losses. In recent years, versions of both the Finite Element Method (FEM) and the Boundary Element Method (BEM) including viscous and thermal losses have been developed. This paper deals with an improved formulation in three dimensions of the BEM with losses which avoids the calculation of tangential derivatives on the surface by finite differences used in a previous BEM implementation. Instead, the tangential derivatives are obtained from the element shape functions. The improved implementation is demonstrated using an oscillating sphere, where an analytical solution exists, and a condenser microphone as test cases.

Keywords: Boundary element method; viscous and thermal acoustic losses.

1. Introduction

The effect of viscous and thermal losses in sound waves has been described long ago and is part of the general theory of physical acoustics.[1–3] In free-field propagation in the audio range, such effects are only important over long distances such as in large auditoria, or outdoor sound propagation. However, they become very relevant at very close distance to the domain boundaries because (i) air molecules cannot slide over the boundary so that particle velocity must match boundary velocity in the normal and tangential directions, and (ii) boundaries usually have such higher thermal conductivity than the fluid, that temperature variation is negligible at the boundary. The viscous and thermal *boundary layers* are generated by these effects, and are usually accounted for as boundary acoustic impedance. In the case of small setups with dimensions comparable to the boundary layer thicknesses, which vary from a fraction of a millimeter to a few micrometers, such

approximation is not possible, and some other analytical or numerical model is necessary. Devices of this kind are acoustic transducers, couplers, hearing aids and small-scale acoustic metamaterials.[4–6]

For intricate and highly coupled devices, approximate solutions taking limiting hypothesis may not be sufficient for appropriate modeling. They must be tested or even replaced by full numerical models of the sound field with viscous and thermal losses. On the one hand, the Finite Element Method (FEM) can be employed for solving the no-flow linearized Navier–Stokes equations with no further hypotheses.[7–10] The FEM implementation with losses is included in some commercial FEM software packages.[11]

On the other hand, an equally full implementation with losses uses the Boundary Element Method (BEM).[12,13] The BEM is applied to the so-called viscous, thermal and acoustic modes resulting from the Kirchhoff decomposition of the Navier–Stokes equations.[2,3,14] These three *modes* are coupled at the boundary with extended boundary conditions. The particle velocity boundary condition in the existing BEM with losses includes first and second tangential derivatives of the pressure at the boundary, which use finite differences and, as will be shown in this paper, can trigger numerical errors. The tangential derivative scheme is particularly cumbersome in the three-dimensional BEM implementation with losses.[13]

It is therefore desirable that the BEM with losses can be reformulated in a way that avoids finite difference intermediate calculations. One possibility is based on setting the tangential derivative as an initial variable to be solved for and reformulating the integral equations.[15] In this paper, another alternative is presented, which preserves the integral equations but replaces the finite differences by derivatives of the element shape functions. The modified implementation is developed for three-dimensional domains and two examples are used to test its performance.

After this introduction, Sec. 2 outlines the theoretical foundation on which the existing BEM for acoustics with viscous and thermal losses is based. Section 3 explains the new method for imposing the particle velocity boundary conditions. As a verification, Sec. 4 presents an oscillating sphere test case where the new formulation is compared with the previous three-dimensional BEM implementation with losses and an analytical solution. Section 5 examines the performance of the new and existing formulations with a model of a condenser microphone. A discussion section comments the results of the tests, followed by a final section with conclusions and future work.

2. BEM Formulation with Losses

The previously published three-dimensional BEM implementation with losses is described in detail in Ref. 13. In this section, a short account of it is given with special focus on the issues that motivate this paper. The physical framework is characterized by:

$$(\Delta + k_a^2)p_a = 0, \tag{1}$$

$$(\Delta + k_h^2)p_h = 0, \tag{2}$$

$$(\Delta + k_v^2)\vec{v}_v = \vec{0} \quad \text{with } \nabla \cdot \vec{v}_v = 0. \tag{3}$$

Equations (1)–(3) represent the three *modes* of the Kirchhoff decomposition of the Navier–Stokes equations on which the BEM implementation is based.[2,14] Harmonic time dependence $e^{i\omega t}$ is omitted. The indexes (a, h, v) indicate the so-called acoustic, thermal and viscous *modes*, respectively, which can be treated independently in the acoustic domain and linked through the boundary conditions. The total pressure can be obtained as the sum $p = p_a + p_h$ of the acoustic and thermal components (there is not a viscous p_v), while the particle velocity has contributions from the three *modes* as $\vec{v} = \vec{v}_a + \vec{v}_h + \vec{v}_v$. In this paper, magnitudes written with an arrow vector on top are vectorial fields, while bold letters indicate matrices. The three wavenumbers k_a, k_h and k_v are function of the lossless wavenumber k and the physical properties of the fluid: viscosity, bulk viscosity and thermal conductivity coefficients, air density, and specific heats.[14] Equation (1) is a wave equation, while Eqs. (2) and (3) are diffusion equations. There are five equations and five unknowns because the viscous velocity $\vec{v}_v$ is a three-component vector and therefore Eq. (3) is split into three components. The boundary conditions are:

$$T = T_a + T_h = \tau_a p_a + \tau_h p_h = 0, \tag{4}$$

$$\vec{v}_{\text{boundary}} = \vec{v}_a + \vec{v}_h + \vec{v}_v = \phi_a \nabla p_a + \phi_h \nabla p_h + \vec{v}_v. \tag{5}$$

Equation (4) states that the temperature T, the sum of its acoustic and thermal components T_a and T_h, remains constant at the boundary, leading to a condition that links the thermal and acoustic pressures p_a and p_h. Equation (5) ensures that the total particle velocity, expressed as the sum of acoustic, thermal and viscous contributions, matches the boundary velocity in any direction. The parameters τ_a, τ_h, ϕ_a and ϕ_h depend, like the wavenumbers in Eqs. (1)–(3), on physical constants and the frequency. The velocity equation (5) is a vector equation, which can be split for convenience into normal and tangential components:

$$\vec{v}_{\text{boundary},n} = \phi_a \frac{\partial p_a}{\partial n} + \phi_h \frac{\partial p_h}{\partial n} + \vec{v}_{v,n}, \tag{6}$$

$$\vec{v}_{\text{boundary},t} = \phi_a \nabla_t p_a + \phi_h \nabla_t p_h + \vec{v}_{v,t}. \tag{7}$$

Note that Eqs. (1)–(3) are of the same form as the lossless harmonic Helmholtz equation. The BEM implementation with losses starts by discretizing these three equations independently, using the same procedure as in the lossless BEM, that is, converting the Helmholtz equation into its integral form[16,17]

$$C(P)p(P) = \int_S \left[\frac{\partial G(Q)}{\partial n} p(Q) - \frac{\partial p(Q)}{\partial n} G(Q) \right] dS + p^I(P), \tag{8}$$

where p is the sound pressure, G is the Green's function and P and Q are points in the domain and on the surface, respectively. $C(P)$ is a geometrical constant and $p^I(P)$ is the incident pressure, if present. The boundary is then divided into surface elements and Eq. (8) is discretized as

$$\mathbf{A}\mathbf{p} - \mathbf{B}\frac{\partial \mathbf{p}}{\partial n} + \mathbf{p}^I = 0. \tag{9}$$

Equation (9) is defined over the boundary. Given a set of boundary conditions, it can be solved for obtaining the boundary pressure and normal particle velocity. The acoustic magnitudes in the domain are obtained from the surface solution by re-applying the discretized Helmholtz Integral Equation.

The harmonic Eqs. (1)–(3) of the Kirchhoff decomposition can be discretized as

$$\mathbf{A}_a\mathbf{p}_a - \mathbf{B}_a\frac{\partial \mathbf{p}_a}{\partial n} + \mathbf{p}^I = 0, \tag{10}$$

$$\mathbf{A}_h\mathbf{p}_h - \mathbf{B}_h\frac{\partial \mathbf{p}_h}{\partial n} = 0, \tag{11}$$

$$\mathbf{A}_v\vec{\mathbf{v}}_v - \mathbf{B}_v\frac{\partial \vec{\mathbf{v}}_v}{\partial n} = \vec{0} \quad \text{with } \nabla\cdot\vec{\mathbf{v}}_v = 0. \tag{12}$$

The development in Ref. 13 makes use of coordinate transformations between the node-based local reference system (normal and tangential vectors n, t_1 and t_2) and the global Cartesian reference (x, y, z) to combine Eqs. (10)–(12). The coupling conditions in Eqs. (4) and (5) and the null divergence of the viscous velocity in Eq. (12) are employed. The resulting system of equations for obtaining the acoustic component of the pressure on the boundary is

$$\begin{aligned}
&\left[\phi_a\mathbf{B}_a^{-1}\mathbf{A}_a - \phi_h\mathbf{B}_h^{-1}\mathbf{A}_h\frac{\tau_a}{\tau_h} + [\mathbf{N}_{11}\circ(\mathbf{B}_v^{-1}\mathbf{A}_v)]^{-1}\left(\phi_a - \frac{\tau_a}{\tau_h}\phi_h\right)\right.\\
&\qquad\left.\times\left([\mathbf{N}_{12}\circ(\mathbf{B}_v^{-1}\mathbf{A}_v)]\frac{\partial}{\partial t_1} + [\mathbf{N}_{13}\circ(\mathbf{B}_v^{-1}\mathbf{A}_v)]\frac{\partial}{\partial t_2} + \Delta_t\right)\right]\mathbf{p}_a\\
&\quad= \vec{\mathbf{v}}_{\text{boundary},n} + [\mathbf{N}_{11}\circ(\mathbf{B}_v^{-1}\mathbf{A}_v)]^{-1}\left[[\mathbf{N}_{12}\circ(\mathbf{B}_v^{-1}\mathbf{A}_v)] + \frac{\partial}{\partial t_1}\right]\vec{\mathbf{v}}_{\text{boundary},t_1}\\
&\qquad+ [\mathbf{N}_{11}\circ(\mathbf{B}_v^{-1}\mathbf{A}_v)]^{-1}\left[[\mathbf{N}_{13}\circ(\mathbf{B}_v^{-1}\mathbf{A}_v)] + \frac{\partial}{\partial t_2}\right]\vec{\mathbf{v}}_{\text{boundary},t_2} - \phi_a\mathbf{B}_a^{-1}\mathbf{p}^I.
\end{aligned} \tag{13}$$

The "$\circ$" operator in Eq. (13) is the Hadamard matrix product and the constant matrices $\mathbf{N}_{11}$, $\mathbf{N}_{12}$ and $\mathbf{N}_{13}$ are obtained as

$$\begin{aligned}
\mathbf{N}_{11} &= \mathbf{n}_x\mathbf{n}_x^T + \mathbf{n}_y\mathbf{n}_y^T + \mathbf{n}_z\mathbf{n}_z^T,\\
\mathbf{N}_{12} &= \mathbf{n}_x\mathbf{t}_{1,x}^T + \mathbf{n}_y\mathbf{t}_{1,y}^T + \mathbf{n}_z\mathbf{t}_{1,z}^T,\\
\mathbf{N}_{13} &= \mathbf{n}_x\mathbf{t}_{2,x}^T + \mathbf{n}_y\mathbf{t}_{2,y}^T + \mathbf{n}_z\mathbf{t}_{2,z}^T,
\end{aligned} \tag{14}$$

where the right-hand sides contain products of the (x, y, z) components of the node-based normal and tangential vectors n, t_1 and t_2.

Equation (13) relates the prescribed normal and tangential velocities on the boundary ($\vec{\mathbf{v}}_{\text{boundary},n}$, $\vec{\mathbf{v}}_{\text{boundary},t_1}$ and $\vec{\mathbf{v}}_{\text{boundary},t_2}$) and the incident pressure $\mathbf{p}^I$ with the boundary pressures associated with the acoustic mode $\mathbf{p}_a$. After solving this system, it is possible to derive the remaining magnitudes on the boundary ($\mathbf{p}_h, \vec{\mathbf{v}}_v$), and on the domain, as described in Ref. 13.

The $\frac{\partial}{\partial t_1}$, $\frac{\partial}{\partial t_2}$ and Δ_t operators in Eq. (13) are tangential derivatives and tangential laplacian, respectively. They are implemented in Ref. 13 as matrices with a finite difference scheme based on Voronoi cells over nonregular meshes.[18,19] This method implies that the finite difference step size is equivalent to the element dimensions of the boundary mesh. The implementation described in this section will be termed *Finite Difference Derivative BEM* (FDD-BEM).

3. BEM Implementation with Losses Using Shape Function Derivatives

It has been found that the finite difference scheme just described in the previous section can be detrimental for the performance of the BEM with viscous and thermal losses, as will be shown in the test case calculations further in this paper. In this section, we propose a modified implementation that does not include finite differences. It is based on the same set of equations and coupling conditions in the previous section, but in this case, the tangential derivatives are adapted from the analytical derivatives of the element shape functions.

In this paper, a direct collocation implementation of the BEM is used.[20] The boundary surface is meshed with isoparametric quadratic triangular elements. Other elements could be used, providing they are second-order (quadratic) or higher. This ensures that the tangential derivative approximation is at least first-order (linear).

By using the chain rule derivation, the derivatives of the shape functions with respect to the local element coordinates can be converted into derivatives with respect to the global coordinates as[21]

$$\begin{Bmatrix} \frac{\partial N_i}{\partial x} \\ \frac{\partial N_i}{\partial y} \\ \frac{\partial N_i}{\partial z} \end{Bmatrix} = \begin{bmatrix} \frac{\partial x}{\partial \xi_1} & \frac{\partial y}{\partial \xi_1} & \frac{\partial z}{\partial \xi_1} \\ \frac{\partial x}{\partial \xi_2} & \frac{\partial y}{\partial \xi_2} & \frac{\partial z}{\partial \xi_2} \\ \frac{\partial x}{\partial \xi_3} & \frac{\partial y}{\partial \xi_3} & \frac{\partial z}{\partial \xi_3} \end{bmatrix}^{-1} \begin{Bmatrix} \frac{\partial N_i}{\partial \xi_1} \\ \frac{\partial N_i}{\partial \xi_2} \\ \frac{\partial N_i}{\partial \xi_3} \end{Bmatrix}, \tag{15}$$

where the inverted matrix in the right-hand side is the Jacobian and N_i is a shape function. The derivatives $(\frac{\partial N_i}{\partial \xi_1}, \frac{\partial N_i}{\partial \xi_2}, \frac{\partial N_i}{\partial \xi_3})$ are obtained analytically. Equation (15) is written for three-dimensional elements, but it is possible to rewrite it for surface elements in three-dimensional domains. Surface elements have only two independent local coordinates (ξ_1, ξ_2), so the last row of the Jacobian matrix is obtained as the vector product of the first two rows.[22] In our case, the tangential derivatives $(\frac{\partial}{\partial t_1}, \frac{\partial}{\partial t_2})$ at the nodal positions are needed. The global (x, y, z) coordinate system is therefore replaced by the node-related local coordinate system (n, t_1, t_2) using a linear coordinate change. This procedure is repeated for all shape functions on every node. We calculate the two tangential derivatives of the viscous velocity vector as

$$\frac{\partial \mathbf{v}_{v,x}}{\partial t_1} = \sum_i \left(\frac{\partial N_i}{\partial t_1} v_{v,x,i} \right), \quad \frac{\partial \mathbf{v}_{v,y}}{\partial t_1} = \sum_i \left(\frac{\partial N_i}{\partial t_1} v_{v,y,i} \right), \quad \frac{\partial \mathbf{v}_{v,z}}{\partial t_1} = \sum_i \left(\frac{\partial N_i}{\partial t_1} v_{v,z,i} \right),$$

$$\frac{\partial \mathbf{v}_{v,x}}{\partial t_2} = \sum_i \left(\frac{\partial N_i}{\partial t_2} v_{v,x,i} \right), \quad \frac{\partial \mathbf{v}_{v,y}}{\partial t_2} = \sum_i \left(\frac{\partial N_i}{\partial t_2} v_{v,y,i} \right), \quad \frac{\partial \mathbf{v}_{v,z}}{\partial t_2} = \sum_i \left(\frac{\partial N_i}{\partial t_2} v_{v,z,i} \right), \tag{16}$$

where $v_{v,x}$, $v_{v,y}$ and $v_{v,z}$ are the Cartesian components of the viscous velocity vector. Their tangential derivatives are expressed as a function of the nodal values $v_{v,x,i}$, $v_{v,y,i}$ and $v_{v,z,i}$. Note that if the elements are continuous, nodes can be shared by several elements. In this case, the contributions to the tangential derivatives from all elements the node belongs to are averaged. The tangential derivatives of the acoustic pressure are obtained in the same way,

$$\frac{\partial p_a}{\partial t_1} = \sum_i \left(\frac{\partial N_i}{\partial t_1} p_{a,i} \right), \quad \frac{\partial p_a}{\partial t_2} = \sum_i \left(\frac{\partial N_i}{\partial t_2} p_{a,i} \right). \tag{17}$$

The viscous velocity is a rotational vector field; its divergence is zero ($\frac{\partial \mathbf{v}_{v,n}}{\partial n} + \frac{\partial \mathbf{v}_{v,t_1}}{\partial t_1} + \frac{\partial \mathbf{v}_{v,t_2}}{\partial t_2} = 0$). The three terms of this divergence can be expressed as

$$\frac{\partial \mathbf{v}_{v,n}}{\partial n} = \mathbf{n}_x \circ (\mathbf{B}_v^{-1} \mathbf{A}_v \mathbf{v}_{v,x}) + \mathbf{n}_y \circ (\mathbf{B}_v^{-1} \mathbf{A}_v \mathbf{v}_{v,y}) + \mathbf{n}_z \circ (\mathbf{B}_v^{-1} \mathbf{A}_v \mathbf{v}_{v,z}), \tag{18}$$

$$\frac{\partial \mathbf{v}_{v,t_1}}{\partial t_1} = \mathbf{t}_{1,x} \circ \sum_i \left(\frac{\partial N_i}{\partial t_1} v_{v,x,i} \right) + \mathbf{t}_{1,y} \circ \sum_i \left(\frac{\partial N_i}{\partial t_1} v_{v,y,i} \right) + \mathbf{t}_{1,z} \circ \sum_i \left(\frac{\partial N_i}{\partial t_1} v_{v,z,i} \right), \tag{19}$$

$$\frac{\partial \mathbf{v}_{v,t_2}}{\partial t_2} = \mathbf{t}_{2,x} \circ \sum_i \left(\frac{\partial N_i}{\partial t_2} v_{v,x,i} \right) + \mathbf{t}_{2,y} \circ \sum_i \left(\frac{\partial N_i}{\partial t_2} v_{v,y,i} \right) + \mathbf{t}_{2,z} \circ \sum_i \left(\frac{\partial N_i}{\partial t_2} v_{v,z,i} \right). \tag{20}$$

Equation (18) is obtained by taking the normal derivative of the coordinate change $\mathbf{v}_{v,n} = \mathbf{n}_x \circ \mathbf{v}_{v,x} + \mathbf{n}_y \circ \mathbf{v}_{v,y} + \mathbf{n}_z \circ \mathbf{v}_{v,z}$ and replacing the three Cartesian components of Eq. (12). Equations. (19) and (20) are the result of replacing the relations of Eq. (16) in the tangential derivatives of the remaining coordinate change equations $\mathbf{v}_{v,t_1} = \mathbf{t}_{1,x} \circ \mathbf{v}_{v,x} + \mathbf{t}_{1,y} \circ \mathbf{v}_{v,y} + \mathbf{t}_{1,z} \circ \mathbf{v}_{v,z}$ and $\mathbf{v}_{v,t_2} = \mathbf{t}_{2,x} \circ \mathbf{v}_{v,x} + \mathbf{t}_{2,y} \circ \mathbf{v}_{v,y} + \mathbf{t}_{2,z} \circ \mathbf{v}_{v,z}$.

Using the properties of the Hadamard operator "$\circ$", Eqs. (18)–(20) can be rearranged as

$$\frac{\partial \mathbf{v}_{v,n}}{\partial n} = [(\mathbf{n}_x \mathbf{I}) \circ (\mathbf{B}_v^{-1} \mathbf{A}_v)] \mathbf{v}_{v,x} + [(\mathbf{n}_y \mathbf{I}) \circ (\mathbf{B}_v^{-1} \mathbf{A}_v)] \mathbf{v}_{v,y} + [(\mathbf{n}_z \mathbf{I}) \circ (\mathbf{B}_v^{-1} \mathbf{A}_v)] \mathbf{v}_{v,z}, \tag{21}$$

$$\frac{\partial \mathbf{v}_{v,t_1}}{\partial t_1} = [(\mathbf{t}_{1,x} \mathbf{I}) \circ \mathbf{D}_{t_1}] \mathbf{v}_{v,x} + [(\mathbf{t}_{1,y} \mathbf{I}) \circ \mathbf{D}_{t_1}] \mathbf{v}_{v,y} + [(\mathbf{t}_{1,z} \mathbf{I}) \circ \mathbf{D}_{t_1}] \mathbf{v}_{v,z}, \tag{22}$$

$$\frac{\partial \mathbf{v}_{v,t_2}}{\partial t_2} = [(\mathbf{t}_{2,x} \mathbf{I}) \circ \mathbf{D}_{t_2}] \mathbf{v}_{v,x} + [(\mathbf{t}_{2,y} \mathbf{I}) \circ \mathbf{D}_{t_2}] \mathbf{v}_{v,y} + [(\mathbf{t}_{2,z} \mathbf{I}) \circ \mathbf{D}_{t_2}] \mathbf{v}_{v,z}, \tag{23}$$

where $\mathbf{D}_{t_1}$ and $\mathbf{D}_{t_2}$ are matrices implementing the tangential derivatives and $\mathbf{I}$ is the identity matrix. We may also impose the no-slip condition Eq. (7) by using Eq. (17). After some

manipulation, it becomes

$$\vec{\mathbf{v}}_{\text{boundary},t_1} = \left[\left(\phi_a - \frac{\tau_a}{\tau_h}\phi_h\right)\mathbf{D}_{t_1}\right]\mathbf{p}_a + (\mathbf{t}_{1,x}\mathbf{I})\mathbf{v}_{v,x} + (\mathbf{t}_{1,y}\mathbf{I})\mathbf{v}_{v,y} + (\mathbf{t}_{1,z}\mathbf{I})\mathbf{v}_{v,z}, \quad (24)$$

$$\vec{\mathbf{v}}_{\text{boundary},t_2} = \left[\left(\phi_a - \frac{\tau_a}{\tau_h}\phi_h\right)\mathbf{D}_{t_2}\right]\mathbf{p}_a + (\mathbf{t}_{2,x}\mathbf{I})\mathbf{v}_{v,x} + (\mathbf{t}_{2,y}\mathbf{I})\mathbf{v}_{v,y} + (\mathbf{t}_{2,z}\mathbf{I})\mathbf{v}_{v,z}. \quad (25)$$

Finally, the normal velocity coupling condition Eq. (6) can be arranged as

$$\vec{\mathbf{v}}_{\text{boundary},n} = \left[\phi_a\mathbf{B}_a^{-1}\mathbf{A}_a - \phi_h\mathbf{B}_h^{-1}\mathbf{A}_h\frac{\tau_a}{\tau_h}\right]\mathbf{p}_a + (\mathbf{n}_x\mathbf{I})\mathbf{v}_{v,x} + (\mathbf{n}_y\mathbf{I})\mathbf{v}_{v,y} + (\mathbf{n}_z\mathbf{I})\mathbf{v}_{v,z} + \phi_a\mathbf{B}_a^{-1}\mathbf{p}^I. \quad (26)$$

The preceding equations are combined into a system of equations of the form

$$\begin{bmatrix} \text{Normal velocity coupling, Eq. (26)} \\ \text{Null divergence of } \vec{\mathbf{v}}_v\text{, Eqs. (21)–(23)} \\ \text{No-slip condition } t_1\text{, Eq. (24)} \\ \text{No-slip condition } t_2\text{, Eq. (25)} \end{bmatrix} \begin{Bmatrix} \mathbf{p}_a \\ \mathbf{v}_{v,x} \\ \mathbf{v}_{v,y} \\ \mathbf{v}_{v,z} \end{Bmatrix} = \begin{Bmatrix} \vec{\mathbf{v}}_{\text{boundary},n} - \phi_a\mathbf{B}_a^{-1}\mathbf{p}^I \\ 0 \\ \vec{\mathbf{v}}_{\text{boundary},t_1} \\ \vec{\mathbf{v}}_{\text{boundary},t_2} \end{Bmatrix}. \quad (27)$$

Note that the system in Eq. (27) has four sets of unknowns, $\mathbf{p}_a$, $\mathbf{v}_{v,x}$, $\mathbf{v}_{v,y}$ and $\mathbf{v}_{v,z}$, while the original system in Eq. (13) is solved for $\mathbf{p}_a$ alone. This means that a coefficient matrix that is 4×4 times larger avoids the need of a second-order tangential derivative. The system is solved, as for FDD-BEM, using the MATLAB backslash operator. The expanded coefficient matrix is not fully populated: in the sphere test case, only about 1/3 of the matrix coefficients in Eq. (27) are nonzero. The solving could be made more efficient by making use of sparsity, e.g. by using dedicated solvers.

From the solution of Eq. (27), it is possible to obtain all other magnitudes on the boundary and the domain using the procedure described in Ref. 13. This new version of the BEM with losses will be called *Shape Function Derivative BEM* (SFD-BEM).

In order to evaluate independently the effect of using shape function derivatives and the expanded system of equations of Eq. (27), a combined version of the two methods is also employed. It is named FDD2-BEM, and it uses the finite difference tangential derivatives from Sec. 2 into Eq. (27).

4. Oscillating Sphere Test Case

The performance of the SFD-BEM against the FDD-BEM is studied using a test case containing losses: a sphere with a radius of 1 m that radiates sound by oscillating as a whole with a velocity of 10^{-2} m/sec along the z-axis. Only the results at the boundary are calculated; domain results are possible, but less suitable for the purpose of this study. This test case has an analytical solution and has been previously used for testing the axisymmetrical

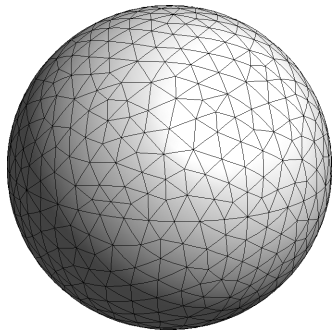

Fig. 1. BEM mesh of the sphere employed in the test case with 2406 nodes and 1202 elements.

version of the BEM with losses.[12,23] Note that the analytical solution does not consider thermal losses. This is not however a problem since the main difficulties of all formulations with losses lie in the viscous mode, which is largely dominant in this test case.

The boundary mesh is generated using the software package Gmsh.[24] It contains 2406 nodes and 1202 quadratic 6-node triangular elements and is shown in Fig. 1. The Gmsh initial surface element size is specified as 1/7 times the sphere radius.

The oscillating sphere is centered on the origin, and generates a viscous mode velocity on its surface, which is larger and tangential to the boundary at its equator ($z = 0$). The tangential component of this viscous velocity must cancel the acoustic and thermal tangential velocities so as to fulfill the no-slip condition. The normal component of the viscous velocity is much smaller than its normal component, and it has its magnitude maxima at the poles ($z = \pm 1$). Four frequencies have been calculated: 200 Hz, 500 Hz, 800 Hz and 1000 Hz. For these frequencies and the mesh in Fig. 1, the approximate numbers of nodes per wavelength are 22, 8.8, 5.4 and 4.4, respectively, so that the last two are below the six nodes per wavelength rule of thumb. The frequencies are chosen away from internal eigenfrequencies of the sphere so as to avoid the nonuniqueness problem of the BEM.[22]

Figure 2 shows the results on the surface of the acoustic mode pressure and the normal and tangential components of the viscous mode velocity at 1 kHz. The FDD-BEM fails to calculate the relatively small normal component of the viscous velocity, as can be seen in the mid-left plot. The combined version FDD2-BEM using finite differences in the expanded system of equations in Eq. (27) brings some improvement, as shown in the central plot. Only the SFD-BEM, in the left column graphs, calculates all three magnitudes satisfactorily. Comparison of FDD-BEM and FDD2-BEM allows estimating the effect of expanding the system of equations from Eq. (13) to Eq. (27), while the comparison of FDD2-BEM and SFD-BEM shows the effect of using shape function tangential derivatives over finite differences. Similar results are obtained at the remaining calculated frequencies, leading to the same conclusions. The difficulty in the calculation of the normal component of the viscous velocity may be a consequence of its relatively small amplitude, making it more seriously affected by machine errors.

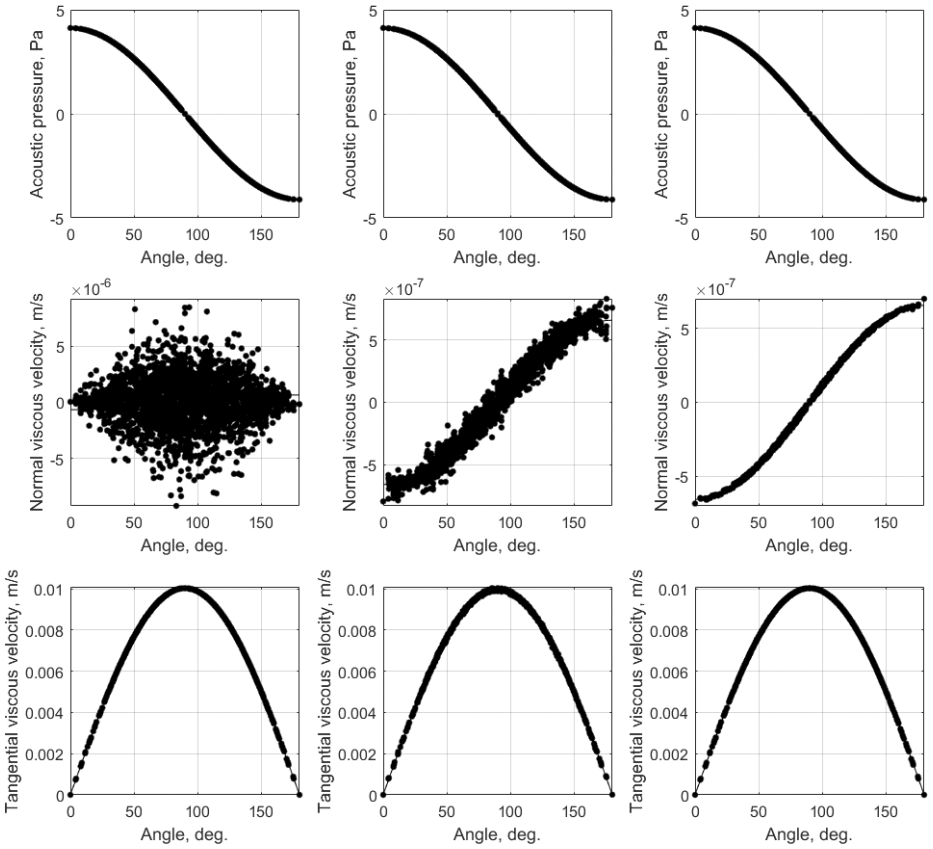

Fig. 2. Solution on the surface over an arc from pole to pole (from $z = 1$ to $z = -1$) of an oscillating sphere, at 1 kHz. The plots on the left column are calculated using the existing FDD-BEM, the plots in the central column use the FDD2-BEM (finite differences combined with Eq. (27)), and the plots on the right column come from the new SFD-BEM. The values are all real parts of the indicated magnitudes. The underlying solid line is the analytical solution, and the dots are BEM results on the mesh nodes. Note the different scales on the normal viscous velocity plots.

Figure 3 examines the relative error for the three formulations (FDD-BEM, SFD-BEM and the combined FDD2-BEM) at four different frequencies. In order to avoid difficulties when the solution is close to zero, the error measure is made relative to the maximum absolute value of the analytical solution over the geometry as

$$\text{Error} = \sum_i \frac{|\text{Analytical}_i - \text{Calculated}_i|}{|\max(\text{Analytical})|}. \tag{28}$$

The ideal expected behavior of the errors would be a steady increase as the frequency grows and the mesh is kept constant.

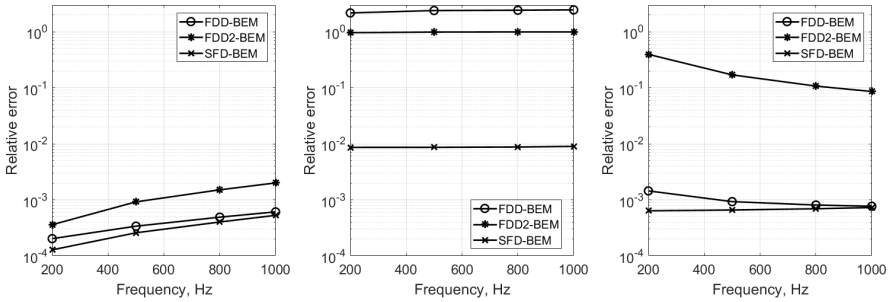

Fig. 3. Relative error at different frequencies of the BEM boundary solution for an oscillating sphere of 1 m radius with the mesh in Fig. 1. The circles correspond to the FDD-BEM, the crosses are obtained with the SFD-BEM and the asterisks are the combined formulation FDD2-BEM. The left-side plot is the acoustic pressure error, the central plot is the normal viscous velocity error and the right-side plot is the tangential viscous velocity error.

5. Microphone Test Case

In many cases, the SFD-BEM performance is similar to the original FDD-BEM formulation, for example, a metamaterial model.[6] However, the SFD-BEM shows its benefits in cases where the calculation is affected by several sources of instability. In this section, we use a three-dimensional BEM model of a condenser microphone as a test case. Such a model has to cope with (i) a very narrow gap behind the membrane with a thickness that is comparable to the thicknesses of the viscous and thermal boundary layers at the membrane resonance frequency, (ii) the coupling of an FEM model of the membrane and a BEM model with losses of the interior, (iii) the intrinsic instability of the BEM for closed cavities.[25]

We revisit here the model of a measurement condenser microphone Brüel & Kjær type 4938 that was used as an example in Ref. 13. This is a $\frac{1}{4}$ inch pressure-field microphone with a gap thickness of 20 μm and a resonance frequency of the membrane of 60 kHz. The

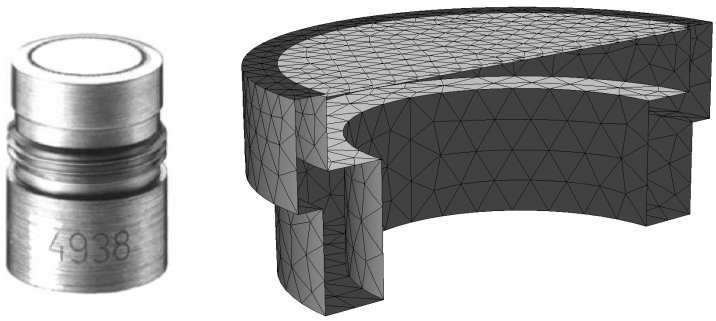

Fig. 4. Photograph (left) and BEM mesh (right) of a Brüel & Kjær microphone type 4938, as in Ref. 13. The mesh has 6322 nodes and 3160 quadratic triangular elements. The membrane is modeled with a two-dimensional FEM and coupled to the interior. The mesh has been cut in half to show the interior with the narrow gap, the back plate electrode and the ring-shaped back cavity.

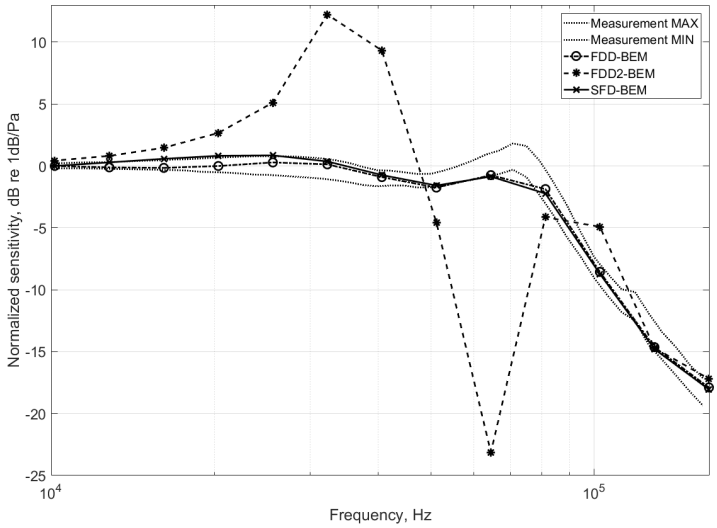

Fig. 5. Normalized sensitivity response with actuator excitation of a Brüel & Kjær microphone type 4938. The dotted lines represent the upper and lower bounds of the measured sensitivities of 183 microphone units. The circles correspond to the FDD-BEM, the crosses are obtained with the SFD-BEM and the asterisks are the combined formulation FDD2-BEM.

microphone and the corresponding BEM mesh are represented in Fig. 4. The interior of the microphone is modeled using BEM with losses, and coupled to a membrane, which is modeled with a two-dimensional FEM, also written for this purpose. The excitation is made to resemble an electrostatic actuator measurement of the microphone sensitivity response by setting a uniform sound pressure over the membrane. In Ref. 13, a node in the back cavity (*vent node*) was given a finite impedance to stabilize the calculation. We have removed the vent node and recalculated this microphone using SFD-BEM, FDD-BEM and FDD2-BEM in the frequency range around the membrane resonance. The result is shown in Fig. 5. Note that it is not possible to match the model with particular measurement results, given the uncertainties in the model input parameters.

6. Discussion

The three formulations analyzed in this paper, the existing FDD-BEM, the new SFD-BEM and the combined FDD2-BEM are studied through two test cases, an oscillating sphere where an analytical solution exists and a measurement condenser microphone.

6.1. *Oscillating sphere test case*

In view of the results in Figs. 2 and 3, we can make the following observations:

(1) The SFD-BEM consistently produces smaller errors than the other two formulations for the three magnitudes examined, as shown in Fig. 3.

(2) As expected from the observation of Fig. 2, the errors in the calculation of the normal component of the viscous velocity are greater in the case of FDD-BEM, followed by FDD2-BEM and SFD-BEM.
(3) Again in Fig. 3 (right-side plot), the FDD-BEM and FDD2-BEM have errors of the tangential component of the viscous velocity that actually decrease as frequency increases, the reason probably being that finite differences have larger numerical errors as the wavelength grows and the difference is closer to the machine precision, counterbalancing the error reduction due to a better discretization.
(4) In the calculation of the tangential component of the viscous velocity and the pressure, FDD-BEM shows smaller errors than FDD2-BEM, indicating that the use of the expanded system of equations in Eq. (27) comes with some cost.
(5) The SFD-BEM has a larger error (yet below 1%) for the normal component of the viscous velocity than for the other two magnitudes. As pointed out in Sec. 4, its relatively lower amplitude may be an explanation, together with the fact that the shape function derivatives follow a linear approximation rather than quadratic.

The error behavior of the three shown magnitudes is different as a result of the involved calculation process. Only the acoustic pressure, which is the first obtained result in all formulations, has an error that grows with the frequency. All in all, the results shown in Figs. 2 and 3 indicate that the expansion of the system of equations (Eq. (27)) and the new strategy using shape functions for the tangential derivatives are advantageous over the other strategies when combined into the SFD-BEM.

6.2. *Condenser microphone test case*

Condenser microphones rely on the viscous and thermal losses in the gap between membrane and back electrode for the correct damping of the membrane resonance: a model with losses is necessary. As mentioned in Sec. 5, the BEM, unlike FEM, becomes unstable for closed interior domains, particularly at mid-low frequencies where the interior pressure tends to be uniform.[25] This problem affects the BEM with or without losses. We have experienced this issue as a source of instability in all closed microphone models, and we have dealt with it in previous publications by adding a finite impedance to one of the nodes in the back cavity, resembling the vent all condenser measurement microphones have. We are working on more fundamental solutions to this flaw of the BEM, since the vent node just forces the pressure to vary in the back cavity without addressing the intrinsic instability of the BEM.

The model should be able to run without a vent node, but the fact is that its removal makes the BEM calculation more prone to instability, as the results presented here confirm. The formulations that are based on finite differences have difficulties to overcome the instability, and this manifests as a system of equations that is close to being singular. In the case of the FDD-BEM, the MATLAB solver is just able to cope with the solution, however issuing warnings on the unreliability of the solution. The expanded system, Eq. (27), in the FDD2-BEM adds some extra difficulty that makes the solver fail; this is compatible with

the observation made in item (4) in Sec. 6.1, about the oscillating sphere results. The solver has no difficulty with the new SFD-BEM, which shows to be more stable and succeeds in providing a solution despite using the expanded system of equations in Eq. (27).

7. Conclusions and Future Work

A modified implementation of the BEM for acoustic waves with viscous and thermal losses is presented in this paper. The technique based in two-dimensional finite differences employed in the previous version[13] of BEM with losses is replaced by analytical derivatives of the element shape functions, thus simplifying the implementation and making it less prone to errors. This is demonstrated through two test cases: an oscillating sphere, which shows a clear improvement for the same mesh density, and a condenser microphone model, where the intrinsic instability of the setup threatens the solution when finite difference tangential derivatives are used. The new shape function tangential derivatives perform well in both test cases.

The benefits of the technique come with some drawbacks. The coefficient matrix of the system of equations is 4×4 times larger, since it must be expanded from one to four sets of unknowns. However, obtaining the six coefficient matrices for the three visco-thermal modes in Eqs. (10)–(12) takes most of the calculation effort and this is the same for both formulations. Another issue is the need for the order of the elements to be sufficient for a good representation of the tangential derivatives, which are one order lower than the shape functions. The quadratic elements employed lead to a linear representation of the derived magnitudes.

The formulation presented here is defined in three dimensions. BEM formulations with losses, based on finite differences, also exist for two-dimensional and axisymmetric problems.[12,26] The shape function derivative technique has not been thoroughly tested in these cases. However, considering that the one-dimensional finite difference scheme employed in two-dimensional and axisymmetric implementations is much more straightforward and precise in these cases, less benefit is expected.

A possible future refinement of the technique is the use of discontinuous elements, where element nodes are not shared.[27–29] The shape function derivative formulation takes an average of the contributions to normal vectors and tangential derivatives from all the elements a node belongs to; this would be avoided by using discontinuous elements, and may lead to even better performance. Another possible improvement is the use of elements of higher orders than quadratic, which would improve the representation of the tangential derivative.

References

1. J. W. S. Rayleigh, *The Theory of Sound*, 2nd edn. (Dover, New York, 1945).
2. A. D. Pierce, *Acoustics*: *An Introduction to its Physical Principles and Applications*, Chap. 10 (McGraw-Hill, New York, 1981).
3. P. M. Morse and K. U. Ingard, *Theoretical Acoustics* (McGraw-Hill, Princeton, 1968).

4. V. Cutanda Henríquez and P. M. Juhl, Modeling measurement microphones using BEM with visco-thermal losses, in *Proc. Joint Baltic-Nordic Acoustics Meeting* (Nordic Acoustic Association, Odense, Denmark, 2012), pp. 18–20.
5. V. Cutanda Henríquez, S. Barrera-Figueroa, A. Torras Rosell and P. M. Juhl, Study of the acoustical properties of a condenser microphone under an obliquely incident plane wave using a fully coupled three-dimensional numerical model, in *Internoise 2015* (Institute of Noise Control Engineering, San Francisco, USA, 2015), pp. 9–120.
6. V. Cutanda Henríquez, P. R. Andersen, J. S. Jensen, P. M. Juhl and J. Sánchez-Dehesa, A numerical model of an acoustic metamaterial using the Boundary Element Method including viscous and thermal losses, *J. Comput. Acoust.* **25**(4) (2016) 1750006-1–11.
7. R. Bossart, N. Joly and M. Bruneau, Methodes de modelisation numerique des champs acoustiques en fluide thermovisqueux, in *Actes du 6^e Congrès Franais d'Acoustique* (Société Française d'Acoustique, Lille, France, 2002), pp. 411–414.
8. M. Malinen, M. Lyly, P. Råback, A. Kärkkäinen and L. Kärkkäinen, A finite element method for the modeling of thermo-viscous effects in acoustics, in *Proc. 4th European Congress Computational Methods in Applied Sciences and Engineering ECCOMAS* (University of Jyväskylä, Department of Mathematical Information Technology, Jyväskylä, Finland, 2004), pp. 1–12.
9. N. Joly, Coupled equations for particle velocity and temperature variation as the fundamental formulation of linear acoustics in thermo-viscous fluids at rest, *Acta Acust. United Acust.* **92** (2006) 202–209.
10. R. Kampinga, Performance of several viscothermal acoustic finite elements, *Acta Acust. United Acust.* **96** (2010) 115–124.
11. COMSOL Multiphysics Reference Manual, Version 5.2 (2015).
12. V. Cutanda Henríquez and P. M. Juhl, An axisymmetric boundary element formulation of sound wave propagation in fluids including viscous and thermal losses, *J. Acoust. United Soc. Am.* **134**(5) (2013) 3409–3418.
13. V. Cutanda Henríquez and P. M. Juhl, Implementation of an acoustic 3D BEM with visco-thermal losses, in *Internoise 2013* (Institute of Noise Control Engineering, Innsbruck, Austria, 2013), pp. 15–18.
14. M. Bruneau, P. Herzog, J. Kergomard and J. D. Polack, General formulation of the dispersion equation in bounded visco-thermal fluid, and application to some simple geometries, *Wave Motion* **11** (1989) 441–451.
15. P. R. Andersen, V. Cutanda Henríquez, N. Aage and S. Marburg, An acoustic hypersingular boundary element formulation including viscous and thermal losses, in *13th Int. Conf. Theoretical and Computational Acoustics*, 30th July–3rd August 2017 (Institute of Mechanics and Mechatronics, Faculty of Mechanical and Industrial Engineering and Institute of Building Construction and Technology, Faculty of Civil Engineering TU Wien, Vienna, Austria, 2017), p. 107.
16. T. W. Wu (ed.), *Boundary Element Acoustics* (WIT Press, UK, 2000).
17. P. M. Juhl, The boundary element method for sound field calculations, PhD thesis, Report No. 55, Technical University of Denmark (1993).
18. N. Sukumar and J. E. Bolander, Numerical computation of discrete differential operators on non-uniform grids, *Comput. Model. Eng. Sci.* **4**(6) (2003) 691–705.
19. C. Grossmann and H. G. Roos, *Numerical Treatment of Partial Differential Equations* (Springer, Berlin, 2007).
20. V. Cutanda Henríquez and P. M. Juhl, OpenBEM — An open source boundary element method software in Acoustics, in *Internoise 2010*, Vol. 7, 13–16 June 2010 (Sociedade Portuguesa de Acustica (SPA), Lisbon, Portugal, 2010), pp. 5796–5805.
21. O. C. Zienkiewic and R. L. Taylor, *The Finite Element Method* (Butterworth-Heinemann, UK, 2000).

22. N. Atalla and F. Sgard, *Finite Element and Boundary Methods in Structural Acoustics and Vibration* (CRC Press, Boca Raton, 2015).
23. S. Temkin, *Elements of Acoustics* (Wiley, New York, 1981).
24. C. Geuzaine and J.-F. Remacle, Gmsh: A three-dimensional finite element mesh generator with built-in pre- and post-processing facilities, *Int. J. Numer. Methods Eng.* **79**(11) (2009) 1309–1331.
25. S. Sorokin and S. T. Christensen, Low-frequency breakdown of boundary element formulation for closed cavities in excitation conditions with a 'breathing'-type component, *Commun. Numer. Methods Eng.* **16** (2000) 325–334.
26. P. R. Andersen, V. Cutanda Henríquez, N. Aage and S. Marburg, Numerical acoustic models including viscous and thermal losses: Review of existing and new methods, in *Proc. DAGA 2017* (Deutsche Gesellschaft fr Akustik e.V, Germany, 2017), pp. 1–4.
27. S. Marburg and S. Schneider, Influence of element types on numerical error for acoustic boundary elements, *J. Comput. Acoust.* **11**(3) (2003) 363–386.
28. L. Chen, H. Chen, C. Zheng and S. Marburg, Structural-acoustic sensitivity analysis of radiated sound power using a finite element/discontinuous fast multipole boundary element scheme, *Int. J. Numer. Methods Fluids* **82**(12) (2016) 858–878.
29. L. Chen, S. Marburg, H. Chen, H. Zhang and H. Gao, An adjoint operator approach for sensitivity analysis of radiated sound power in fully coupled structural-acoustic systems, *J. Comput. Acoust.* **25**(1) (2017) 1750003.

Paper E

Shape optimization of micro-acoustic devices including viscous and thermal losses

Shape optimization of micro-acoustic devices including viscous and thermal losses

Peter Risby Andersen[a,b,*], Vicente Cutanda Henríquez[a,b], Niels Aage[a,c]

[a] *Centre for Acoustic-Mechanical Micro Systems, Technical University of Denmark Ørsteds Plads, Building 352, DK-2800, Kgs. Lyngby, Denmark*
[b] *Department of Electrical Engineering*
[c] *Department of Mechanical Engineering*

Abstract

Since the late 1980s, numerical acoustic shape optimization has been applied successfully to improve the design and development of novel acoustic devices. Most often, viscous and thermal dissipation effects are neglected in the optimization process, as this is an acceptable assumption in e.g. room acoustics, etc. However, in many acoustic devices, ranging from hearing aids to metamaterials, dissipation can significantly influence the acoustic wave behavior. In this paper, we propose a numerical acoustic shape optimization technique and we demonstrate it using two-dimensional quarter-wave and Helmholtz resonators including accurate modelling of viscous and thermal dissipation. By combining a dissipative boundary element method with shape optimization, the sound absorption capability of the resonators located at an impedance tube termination is maximized. Numerical experiments demonstrate the importance of viscothermal dissipation and its impact on the optimization outcome. The resulting resonator shapes, optimized using a lossy assumption, yield significantly better performance compared to their lossless counterpart, with near perfect absorption at the desired optimization frequencies.

Keywords: acoustics, shape optimization, viscothermal losses, boundary element method

*Corresponding author
Email addresses: prand@elektro.dtu.dk (Peter Risby Andersen), vcuhe@elektro.dtu.dk (Vicente Cutanda Henríquez), naage@mek.dtu.dk (Niels Aage)

1. Introduction

Accurate modelling of acoustic devices with small dimensions requires the inclusion of viscous and thermal dissipative effects. The dissipative effects are especially dominant near boundaries, within the viscous and thermal boundary layers, which are in the order of 550-15 μm for air in the audible range. Therefore, as the size of the acoustic domain decreases, the portion of the domain covered by the boundary layers increases, leading to changes in acoustic wave propagation. This situation is very common in small acoustic devices, such as hearing aids, acoustic MEMS devices and condenser microphones, where the dimensions are comparable to the thickness of the boundary layers. In such cases, correct modelling of acoustic dissipation is necessary, making the assumption of isentropic wave propagation insufficient[1, 2, 3, 4, 5]. The same phenomena is also observed in acoustic transducers such as compression drivers where the response is influenced by dissipation, due to narrow channels and chambers [6, 7, 8].

Even within the field of room acoustics, micro structures have found their everyday use. For example, the performance of absorbing panels, realized using micro-perforated plates, quarter-wave or Helmholtz resonators, is often very dependent on viscothermal dissipative effects[9, 10].

Another research field that has received attention in recent years is acoustic metamaterials, where unusual bulk behavior and extraordinary wave propagation effects can be achieved[11, 12]. Recent research has shown that ignoring losses in the design of metamaterials may lead to a degraded behaviour[13, 14]. Other publications propose metamaterial designs which take advantage of viscothermal dissipation[15, 16].

Numerical shape and topology optimization have proven to be valuable tools in the discovery of new and better acoustic designs. In the literature, several numerical acoustic optimization approaches exist, making use of either the Finite Element Method (FEM) or the Boundary Element Method (BEM). Es-

pecially, optimization of acoustic horns is well studied [17, 18, 19]. Most of these acoustic optimization procedures are based on an isentropic assumption. However, if the influence of viscous and thermal losses is significant, such optimizations might lead to poorly performing designs. In a recent publication, Christensen [20] proposed a method for acoustic FEM topology optimization including viscothermal losses. By applying the so-called low reduced frequency approximation, the author shows how to optimize the cross section of tubes and slits. While topology optimization has certain advantages compared to, e.g., shape optimization, sometimes yielding non-intuitive designs, viscothermal topology optimization requires a mesh that can resolve the boundary layers in the entire design region. This significantly increases the computational load and as a consequence heavily limits the application to full 3D models.

Efficient and reliable optimization tools that include viscothermal losses can be very beneficial in the design of acoustic devices where losses are relevant, such as those mentioned earlier in the introduction. In this work, we propose a shape optimization technique based on BEM and demonstrate it by designing an anechoic termination of a two-dimensional wave-guide by using quarter-wave and Helmholtz resonators. The absorbing properties of the resonators are optimized, showing how viscous and thermal dissipation alters the final layout of the design. Shape optimization is conducted using a BEM implementation incorporating both viscous and thermal dissipation without any simplification other than linearity and absence of flow. BEM with losses only requires discretization of the boundaries, thus avoiding the adaptation of the domain mesh and boundary layer meshing, making it very suitable for shape optimization. The proposed method has no restrictions to the geometry and can be applied to any viscothermal acoustic problem. The paper is organized as follows; firstly, BEM with losses and the optimization approach are introduced. This is followed by a series of simulations investigating shape optimization of quarter-wave and Helmholtz resonators. Finally, the possibilities and limitations of the proposed methodology are discussed.

2. Boundary Element Method with losses

Numerical modelling of acoustic losses using e.g. FEM, the Finite Difference Method or the Finite Volume Method, is usually realized by discretization of the linearized time-harmonic Navier-Stokes equations [21]. BEM with losses requires a further reformulation of linearized Navier-Stokes equations using the Kirchhoff decomposition[1, 2], resulting in an equation-set given by [22]

$$\Delta p_a + k_a^2 p_a = 0 \tag{1}$$

$$\Delta p_h + k_h^2 p_h = 0 \tag{2}$$

$$\Delta \vec{v}_v + k_v^2 \vec{v}_v = \vec{0} \quad \text{with} \quad \nabla \cdot \vec{v}_v = 0 \tag{3}$$

which consists of three separate equations with the unknown variables being the acoustic pressure p_a, the thermal pressure p_h and the viscous velocity $\vec{v}_v$. Similarly, k_a, k_h and k_v are the acoustic, thermal and viscous complex wavenumbers, respectively. Eqs. (1-3) are formally equal to the Helmholtz equation. The Kirchoff decomposition is convenient because each of the equations can easily be transformed into integral from, so that

$$C(P)p_a(P) = \int_\Gamma \frac{\partial G(R)}{\partial n(Q)} p_a(Q) d\Gamma - \int_\Gamma G(R) \frac{\partial p_a(Q)}{\partial n(Q)} d\Gamma \tag{4}$$

$$C(P)p_h(P) = \int_\Gamma \frac{\partial G(R)}{\partial n(Q)} p_h(Q) d\Gamma - \int_\Gamma G(R) \frac{\partial p_h(Q)}{\partial n(Q)} d\Gamma \tag{5}$$

$$C(P)v_{v,x}(P) = \int_\Gamma \frac{\partial G(R)}{\partial n(Q)} v_{v,x}(Q) d\Gamma - \int_\Gamma G(R) \frac{\partial v_{v,x}(Q)}{\partial n(Q)} d\Gamma \tag{6}$$

$$C(P)v_{v,y}(P) = \int_\Gamma \frac{\partial G(R)}{\partial n(Q)} v_{v,y}(Q) d\Gamma - \int_\Gamma G(R) \frac{\partial v_{v,y}(Q)}{\partial n(Q)} d\Gamma \tag{7}$$

with $C(P)$ being the integral-free term, P is the collocation point, Q is an integration point on the generator, $R = |Q - P|$ is the distance between P and Q and G is the fundamental solution in two dimensions. In this case we assume two-dimensional domain, and the viscous velocity $\vec{v}_v$ is split into its two Cartesian components $v_{v,x}$ and $v_{v,y}$. Eqs. (4)-(7) can then be discretized and coupled at the boundary by applying a no-slip and an isothermal boundary

condition[23]

$$\vec{v}_b = \phi_a \nabla p_a + \phi_h \nabla p_h + \vec{v}_v \tag{8}$$

$$T = \tau_a p_a + \tau_h p_h \simeq 0 \tag{9}$$

where ϕ_a, ϕ_h, τ_a and τ_h are complex constants, derived from the physical quantities: the static density, the speed of sound, the ratio of specific heats at constant pressure, the thermal conductivity, the coefficient of viscosity, the bulk viscosity and the frequency. T is the temperature perturbation at the boundary and $\vec{v}_b$ is the boundary velocity. The total pressure perturbation is the sum of the acoustic and thermal pressures. After coupling and discretization, the final linear system has the form

$$\mathbf{S} \begin{bmatrix} \mathbf{p}_a \\ \mathbf{v}_{v,x} \\ \mathbf{v}_{v,y} \end{bmatrix} = \begin{bmatrix} \mathbf{v}_{b,n} \\ 0 \\ \mathbf{v}_{b,t} \end{bmatrix}. \tag{10}$$

The small bold letters represent the discretized variables and the subindices n and t indicate the boundary normal and tangential components. The matrix $\mathbf{S}$ is the system matrix assembled according to the method found in Ref. [24], with the assumption of two dimensions. Note that p_h has been eliminated from the final system by a Schur complement operation.

Because the optimization approach introduced in the following sections requires repeated function evaluations, code efficiency is important. Therefore, assembly of the BEM matrix is carried out using a compiled MATLAB® MEX/C++ framework, inspired by the BEM software OpenBEM [25]. The C++ implementation has proven to be an order of magnitude faster as compared to the pure MATLAB® OpenBEM code, thus improving the efficiency and usability of the proposed optimization approach.

Additionally, it is possible to take advantage of the sparse nature of the viscous and thermal matrices (the matrices assembled by discretization of Eqs. (5)-(7)). An increase of the computational speed is gained by only performing integration when the distance between P and Q is less than twenty times the boundary layer thickness, or if P and Q are located on the same element. This

threshold is considered sufficient, but could probably be further reduced. By using this simple approach an additional order of magnitude in computational speed is achieved when creating the viscous and thermal matrices.

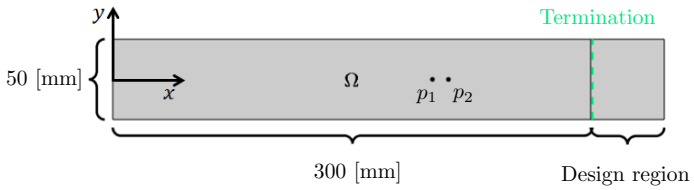

Figure 1: The two-dimensional computational domain Ω including the design region. The two acoustic pressures at p_1 and p_2 are used to calculate the absorption coefficient of the impedance tube termination.

3. Geometry and parametrization

In acoustics, characterization of absorbing materials is often realized using the impedance tube method [26]. Fig. 1 depicts the two-dimensional computational domain Ω, which can be regarded as conceptually equivalent to a three-dimensional tube. It will be referred to as an impedance tube in the following. At the left-hand boundary, the impedance tube is excited by a normal velocity condition with $v_{b,n} = 1\, mm/s$, arbitrarily chosen. The impedance tube is terminated at the right end by a design zone that is occupied by four resonators of either the quarter-wave or Helmholtz types. The resonators are parametrized independently using the same symmetric cubic spline description. Therefore, all resonators have the same shape. The initial parametrized shape and the locations of the cubic spline control points forming the quarter-wave and Helmholtz resonators are seen in Fig. 2a and Fig. 2b, respectively. The shape of the resonators is controlled by changing the positions of the control points (illustrated by blue dots in Fig. 2). Four additional design parameters are used to allow the resonators to scale up to 10% in length individually.

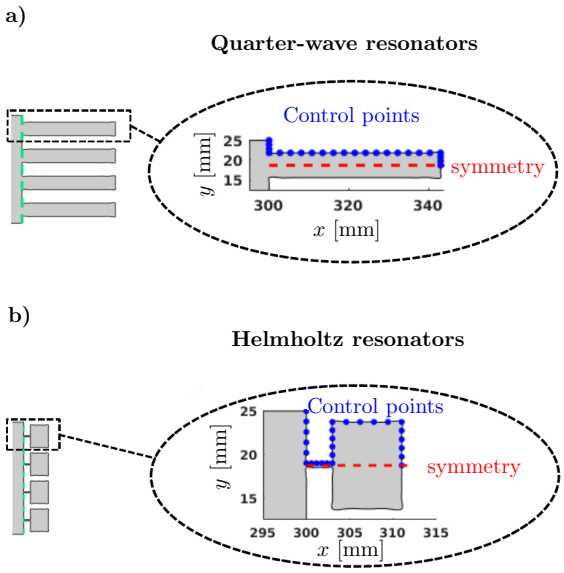

Figure 2: The initial parametrization of the impedance tube termination. The two resonator types used are a) quarter-wave resonators and b) Helmholtz resonators. At the left-hand side of a) and b), the full design is shown. The parametrization of a single resonator is magnified, showing the initial locations of the control points (blue dots) that determine the shape of the resonators.

In shape optimization, choosing an appropriate parametrization method is often difficult. The cubic spline parametrization proposed in this work provides a degree of boundary regularization, at the cost of restricting the possible boundary shapes. This means, e.g., that the resonators cannot form sharp edges and corners. To ensure maximum design freedom, the control points are allowed to move freely in any direction, with the constraints that boundaries are not allowed to intersect and the maximum curvature is limited. The boundary is discretized using approximately 1400 continuous quadratic isoparametric Lagrange boundary elements. Quadratic elements will help maintain boundary

smoothness when distorted. The cubic spline parametrization consists of 23 or 26 control points describing the shape of the quarter-wave or the Helmholtz resonators, respectively.

4. Optimization approach

The shape optimization is performed using the gradient-based sequential quadratic programming approach found in MATLAB®'s *"fmincon"* function[27]. The optimization problem is given by

$$\begin{aligned} \max_{\mathbf{v}}: \quad & \phi(\mathbf{v}) = 1 - \left| \frac{\mathrm{e}^{-\mathrm{i}k_{\mathrm{LL}}\mathrm{d}} - \frac{p_2(\mathbf{v})}{p_1(\mathbf{v})}}{\frac{p_2(\mathbf{v})}{p_1(\mathbf{v})} - \mathrm{e}^{\mathrm{i}k_{\mathrm{LL}}\mathrm{d}}} \right|^2 \\ \text{s. t.} \quad & \boldsymbol{\kappa}(\mathbf{v}) - \kappa_{max} \leq 0 \\ & D_{min} - \beta \mathbf{D}(\mathbf{v}) \leq 0. \\ & \text{Eq. (10)} \end{aligned} \tag{11}$$

where $\mathbf{v}$ are the design variables and $\phi(\mathbf{v})$ is the objective function. The goal is to maximize the absorption coefficient, ranging from 0 (no absorption) to 1 (perfect absorption). The objective function represents therefore the absorption coefficient, obtained using the transfer function method [26]. This method only requires the evaluation of the complex pressure at two positions p_1 and p_2, located at $x = 200\,\mathrm{mm}$ and $x = 210\,\mathrm{mm}$, respectively. The location of p_1 and p_2 is depicted in Fig. 1. Furthermore, $d = 10\,\mathrm{mm}$ is the distance between p_1 and p_2 and k_{LL} is the lossless wavenumber. The domain pressures p_1 and p_2 are obtained via field point calculations of the corresponding acoustic and thermal pressures, using

$$C(P_j)p_a(P_j) = \int_\Gamma \frac{\partial G(R)}{\partial n(Q)} p_a(Q) d\Gamma - \int_\Gamma G(R) \frac{\partial p_a(Q)}{\partial n(Q)} d\Gamma \tag{12}$$

and

$$C(P_j)p_h(P_j) = \int_\Gamma \frac{\partial G(R)}{\partial n(Q)} p_h(Q) d\Gamma - \int_\Gamma G(R) \frac{\partial p_h(Q)}{\partial n(Q)} d\Gamma \tag{13}$$

where P_j represents the location of either p_1 or p_2 and $R = |P_j - Q|$. The total pressure on the two positions is found using that $p = p_a + p_h$. Note that the state

problem is fullfilled at every cycle, i.e., following the so-called nested formulation [28]. The absorption coefficient is a function of the boundary parametrization $\mathbf{v}$, which is a vector containing the coordinates of the control points as well as the scaling factor for the resonator length.

To avoid non-physical boundary behavior, the parametrized boundary is constrained using the curvature magnitude $\boldsymbol{\kappa}$ located at the control points and the distance between control points $\mathbf{D}$. Additionally, we introduce the parameter β which equals -1 if the parametrized boundary self-intersects or 1 otherwise. In this way, too sharp boundaries and self-intersection are avoided. The maximum allowed curvature at the control points is $\kappa_{max} = 6.3\,\mathrm{mm}^{-1}$ and the minimum distance between the individual control points is $D_{min} = 1\,\mu\mathrm{m}$, cf. the dimensions given in Fig 1. Because the boundary is parametrized using C^2 continuous cubic splines, the curvature at a control point is easily obtained in a two-dimensional Cartesian coordinate system as

$$\kappa = \frac{|x'(t)y''(t) - y(t)'x(t)''|}{\left(x'(t)^2 + y'(t)^2\right)^{3/2}} \tag{14}$$

where x and y are the coordinates of a control point as a function of the cubic spline parameter $t \in [0, 1]$, with the primes denoting the derivative with respect to t. The constraints require additional distance calculations between control points, detection of boundary intersections and curvature calculations, making optimization more computationally demanding. Constraints could be avoided by selecting a more restricted parametrization, that enforces a physical behaviour. This would however limit the possible shapes and design freedom. As a benefit, the constraints can also be used to specify and include manufacturing tolerances in the design process.

Gradient information is obtained using a simple forward finite difference (FD) scheme

$$\frac{\partial \phi}{\partial v_i} = \frac{\phi(\mathbf{v} + \Delta v_i \cdot \mathbf{e}_i) - \phi(\mathbf{v})}{\Delta v_i} \tag{15}$$

where v_i is a single design variable, $\mathbf{e}_i$ is a unit vector for the i-th variable

and Δv_i is the step length determined internally by *fmincon*. Efficient adjoint methods can be found in the literature for lossless acoustic BEM shape optimization [29, 17]. However, equivalent adjoint methods for lossy BEM are currently not available. To improve the speed of the FD gradient evaluation *fmincon*'s *UseParallel* option is enabled, allowing the FD gradients to be calculated in parallel. Optimization is performed on a desktop PC with six cores. The FD gradient estimation used is computationally reasonable for the presented case. However, performing optimization of larger problems including more design variables would require an adjoint approach. This is, however, deemed outside the scope of the presented work.

5. Results

In the following, we investigate how viscous and thermal damping affect the design obtained by shape optimization for the impedance tube example. In Section 5.1, quarter-wave resonators are optimized using lossless and lossy BEM formulations, including single- and multi-frequency optimization. As an additional test, the quarter-wave resonators are optimized using a simple bulk loss model. In the second example in Section 5.2, the impedance termination is initialized as Helmholtz resonators which are then further optimized.

5.1. Quarter-wave resonators

Fig. 3 shows the result of a single frequency shape optimization for the quarter-wave resonators problem. The resonators are optimized for maximum absorption at 2 kHz. The optimization was conducted using both lossless and lossy BEM formulations, with ϕ_{LL} and ϕ_{VT} denoting the objective function of the final design, calculated either using a lossless or lossy assumption, respectively. This makes it possible to analyze how the viscothermal losses will impact the final resonator shape. As seen in Fig 3, the two designs deviate in shape depending on whether losses are considered in the design (right side plots) or not (left side plots). The lossless design forms narrower resonators and has

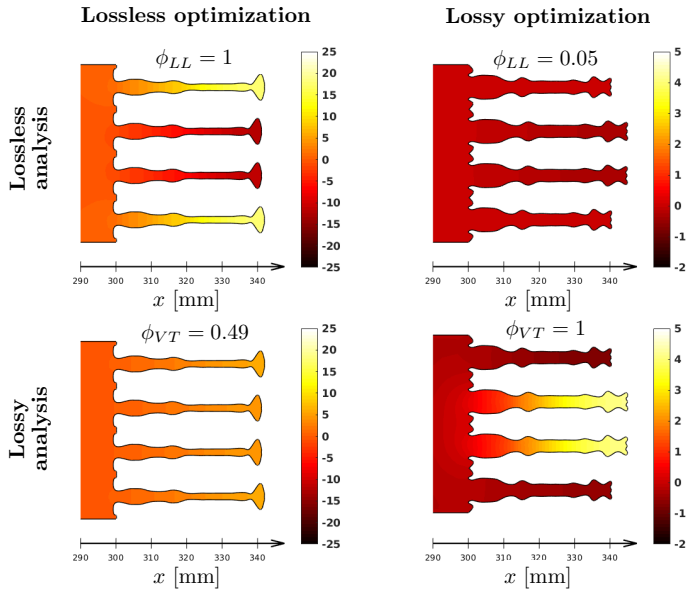

Figure 3: Comparison (crosscheck) of the lossless and lossy optimized designs of the impedance tube termination. Here, ϕ_{LL} and ϕ_{VT} are the lossless and lossy objective functions calculated for the two designs. The initial design consists, of simple quarter wave resonators controlled using a cubic spline representation of the boundary as depicted in Fig. 2a. The plotted field variable is the real part of the pressure in Pascal.

different features compared to that of the lossy design. This is an interesting result because narrow domain parts should contribute to increased absorption, and here, the narrowest design is achieved assuming no losses. It is worth noting that both designs perform perfectly under the settings for which they are optimized, i.e. $\phi_{LL} = 1$ for the lossless design and $\phi_{VT} = 1$ for the lossy design. The performance of the lossless model is a particularly surprising result, as the lossless design is not expected to include any dissipation. Hence, it should not be capable of absorbing any sound. The reason for this surprising result is due

to a peculiarity of numerical BEM: interior BEM problems are prone to numerical damping as reported in [30, 31, 32]. This is most often not a problem when only performing standard analysis of acoustic devices. When optimization is applied using lossless BEM, the optimizer makes use of numerical damping. The design is therefore stable, but unphysical. Had the optimization been performed using a standard FEM model for the analysis, this would no have been the case. Lossless FEM does not introduce any additional phase with respect to the excitation, which translates into a purely imaginary complex pressure. However, in BEM the complex pressure has a real part indicating an additional phase shift due to numerical damping. The real part of the pressure is therefore plotted in Fig 3 as a demonstration. Finally, it is worth noting that while the lossless design does in fact have an absorption coefficient of 0.49 when analysed using the lossy model, the lossy design has almost no absorption capabilities when modelled using the lossless model. This makes it interesting to investigate the influence of the damping mechanism on the optimized designs and also, how much can be achieved using the simple "lossless" BEM model.

First, we examine how the numerical damping performs as compared to the true physical viscothermal model. We start by noting that for the lossless BEM design, convergence can only be achieved when the tubes are allowed to scale in length individually. This allows the quarter-wave resonators to become slightly de-tuned, making it possible for the acoustic energy to be exchanged between the resonators rather than being reflected. This effect is often used in recent publications on metamaterial absorbing surfaces, such as [33, 34]. The resonators in the example form two de-tuned pairs, upper and lower, with the same properties. Combining the phenomena of de-tuned resonators with the inherent numerical damping, consequently gives a lossless design that appears to be a perfect absorber.

On the other hand, the lossy design perfectly absorbs sound at the optimization frequency. Here, the thickness of the resonators is larger compared to the lossless design and the entrance of the resonators has a rippled funnel-shape. The entrance presumably acts as an impedance match, so the acoustic wave can

propagate easier into the narrow region where losses are more significant. At the end of the quarter wave resonators, the boundary is slightly expanded, a possible attempt to maximize boundary length in the region where the pressure magnitude is larger, contributing with additional losses. The lengths of the resonators are organized in a similar pattern as the lossless design, seemingly taking advantage of the de-tuned resonator phenomena. However, the length difference between the de-tuned resonators is slightly larger, and the pressure in the tubes is significantly reduced as compared to that of the lossless design.

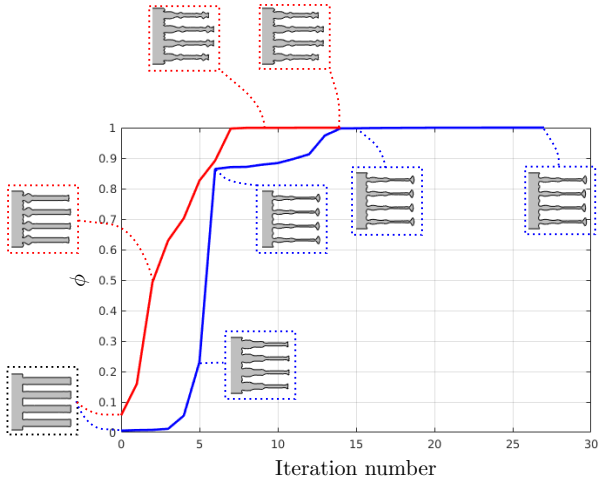

Figure 4: The evolution of the objective function for lossless (blue curve) and lossy (red curve) quarter-wave resonator shape optimization. Selected design shapes obtained at specific iterations are included.

Fig. 4 shows the evolution of the objective function during the optimization process for both lossless and lossy models, with blue and red curves corresponding to ϕ_{LL} or ϕ_{VT}, respectively. In this example, optimization with losses requires less iterations to achieve perfect absorption as compared to lossless optimization. In the lossless case, there is a large change in the objective function between iteration 5 and 6, which is most likely due to the unstable nature of

resonances. Such behaviour is not observed when losses are included. Viscothermal losses stabilize and reduce high-pressure amplitudes near resonance. The total optimization time is 194 min for the lossless design and 135 min for the lossy design. More importantly, we note that the chosen optimizer solves the chosen problem in Eqs. (11) to stationarity, i.e., to an actual KKT point. This is clearly seen in Fig. 4 where the change in objective, as well as the change in layout, is negligible after reaching half of the used iterations. Hence, from an engineering perspective, one could with confidence apply a stopping criteria based on the objective function and the change in layout, and thus save 50% of the computational time.

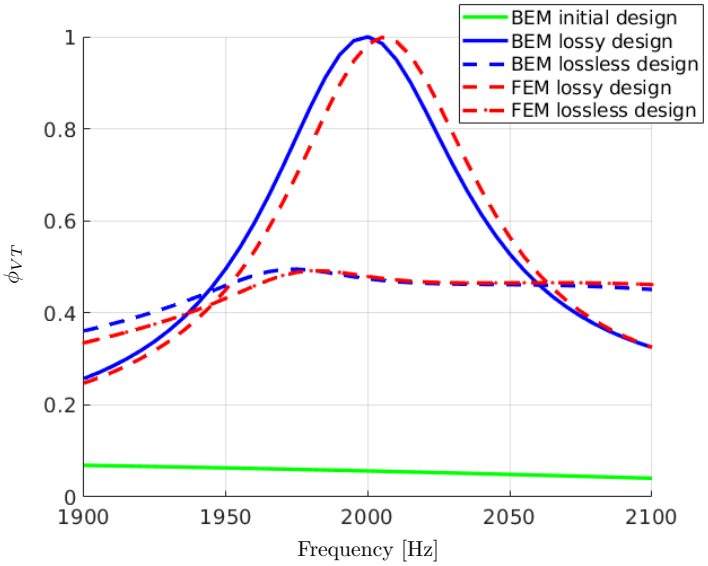

Figure 5: Absorption coefficients, calculated including losses, as a function of frequency for the initial, lossless and lossy designs. The solutions for the lossless and lossy designs are compared with corresponding lossy FEM simulations.

The absorption coefficient as a function of frequency, calculated including losses, is plotted in Fig. 5 for both initial, lossless, and lossy design. As expected,

the lossy design outperforms the lossless design, yielding perfect absorption at the optimization frequency. However, it is worth noting that the lossless design provides an improvement as compared to the initial design. For comparison, Fig 5 includes lossy FEM calculations (red curves) of the corresponding lossless and lossy design. BEM and FEM simulations show almost the same frequency absorption response; however, a 5 Hz frequency shift is observed between the two methods. It is not uncommon to register differences between BEM and FEM models near resonances [35, 36, 37]. Additionally, the FEM geometry might be slightly altered when compared to that of the BEM. The FEM simulations were performed in COMSOL Multiphysics® [38], with a geometry made up of very fine polygons, obtained from an interpolation that uses the BEM shape functions to create additional points along the boundary. This strategy destroys the quadratic geometry discretization in the FEM simulations and most likely contributes to some discrepancies. On the other hand, the FEM simulations were discretized using significantly more elements (approximately 8 million degrees of freedom).

5.1.1. Multi-frequency optimization of quarter-wave resonators

Single frequency optimization limits absorption of the quarter-wave resonators to a narrow band, and in acoustic applications broadband absorption is often desired. A broader absorption response is obtained by including additional optimization frequencies as a part of the objective function. The multi-frequency objective function is defined as the sum of individual objective functions calculated at different frequencies,

$$\phi = \sum_i \tilde{\phi}_i \tag{16}$$

where index i denotes the specific optimization frequency and $\tilde{\phi}$ is the objective function evaluated at a single frequency. Fig. 6 presents multi-frequency optimization results of the quarter-wave resonators. In this case, the setup is optimized at 1950 Hz, 2000 Hz, and 2050 Hz. The additional optimization frequencies increase the frequency range at which sound waves are absorbed, with

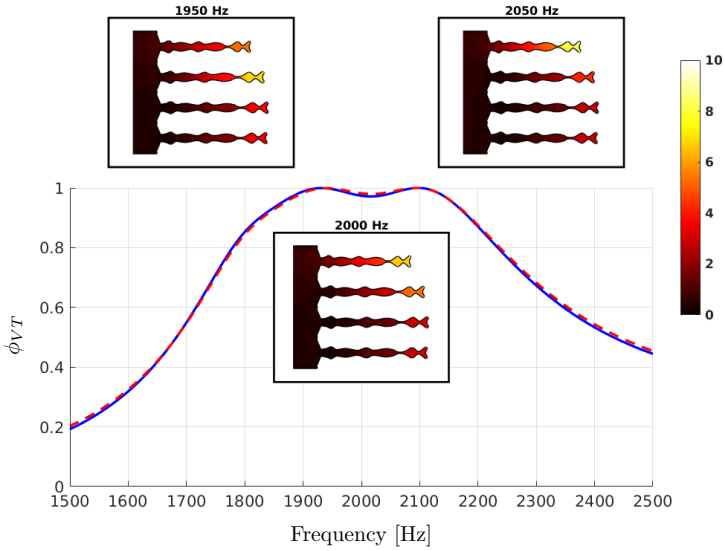

Figure 6: Multi-frequency optimization results, using the sum of the objective functions at 1950, 2000 and 2050 Hz. Field pressure magnitudes are plotted for each optimization frequency. The solid blue and dashed red lines are BEM and FEM simulations, respectively. Both BEM and FEM simulations are calculated including viscothermal losses.

almost full absorption from 1900 to 2100 Hz. The figure also includes insets with the optimized design and the corresponding pressure field magnitudes at the three optimization frequencies. Compared to the previous single frequency designs, the resonators have slightly narrower passages and increased variation along the quarter-wave resonator boundaries. Note also, that the behaviour of the individual quarter-wave resonators changes with frequency. At 2050 Hz, the highest pressure magnitude is observed in the shortest resonator, whereas lower frequencies tend to excite the longer resonators. The length of the quarter-wave resonators is seen to be the primary factor that determines the operational frequency. By having different quarter-wave resonator lengths, the frequency span with high absorption is therefore increased.

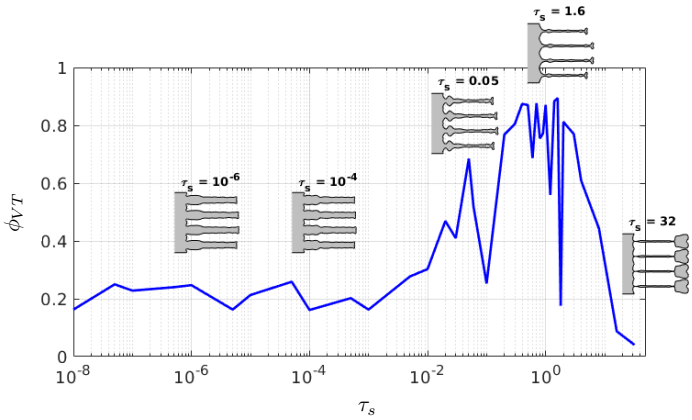

Figure 7: A series of shape optimization results of quarter-wave resonators at 2 kHz with the acoustic losses modeled using a complex wavenumber with a tunable imaginary part. Here, τ_s is the value of the imaginary part of a complex wavenumber and α is the absorption coefficient calculated including viscothermal losses for a given design. The figure includes selected designs obtained with τ_s equal to 10^{-6}, 10^{-4}, 0.05, 1.6 and 32.

5.1.2. Bulk loss description

A common practice when comparing experimental work with lossless simulations is to correct the simulations with an added bulk loss, e.g., using a complex wavenumber with a controllable imaginary part. However, no general procedure exists to estimate the magnitude of the imaginary part, and it is typically problem dependent [39]. It is therefore interesting to investigate how varying the imaginary part of the wavenumber affects the optimization of the quarter-wave resonators. This is accomplished by defining the complex wavenumber as $k_B = k_{LL} - i\tau_s$, where τ_s is the tunable parameter. In Fig. 7, optimized designs are presented using different values of τ_s and compared to the actual absorption coefficient, calculated including viscothermal losses. It is seen how certain values of τ_s result in high absorption coefficients above 80 %. However, none of the used values for τ_s results in a design with perfect absorption. It should also be noted that only a limited amount of simulations with different

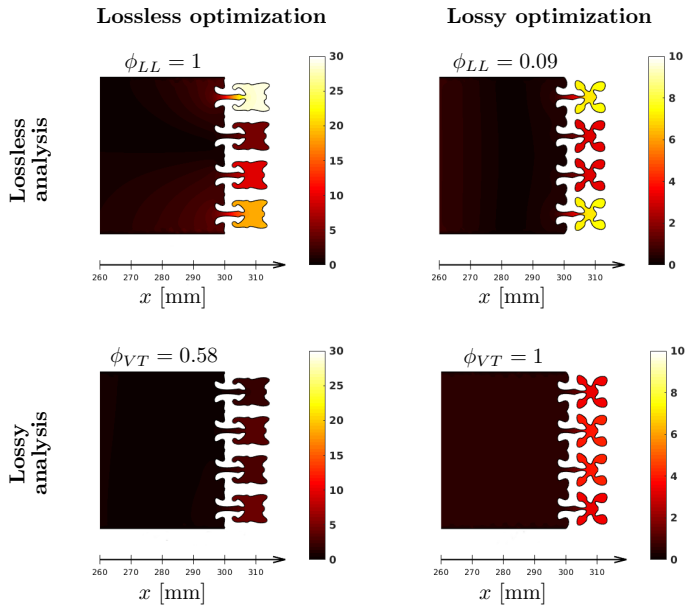

Figure 8: Optimization results of Helmholtz resonators located at the impedance tube termination. The designs are based on either a lossless or a lossy assumption. The field variables are the pressure magnitudes in Pascal

values of τ_s were performed and that there might exist values of τ_s resulting in higher absorption coefficients. In the range $\tau_s \in \{0.01, 3\}$, the absorption coefficients are very sensitive to the choice of τ_s, making it difficult to choose an appropriate value for this particular example. Fig. 7 also depicts inserts with selected designs. It is noteworthy to highlight the design corresponding to $\tau_s = 0.05$ because it is very similar to the single frequency lossy quarter-wave resonator design, although its performance is inferior.

5.2. Helmholtz resonators

In this section, the impedance tube termination is initially parametrized forming four equally sized Helmholtz resonators as described in Fig 2b. The neck and cavity dimensions of the initial shape of the resonators yields an operational frequency near 2 kHz. The Helmholtz resonators are, as in the case of the quarter-wave resonators, optimized under both lossless and lossy conditions. The optimization is carried out at 2 kHz. Fig. 8 contains the resulting lossless and lossy designs which are overlaid with acoustic pressure magnitude field calculations of both the lossless and lossy solutions. Similar to the quarter-wave optimization results, the performance of the lossless design is degraded when introducing losses. When calculated without losses, the lossless design contains varying high pressure amplitudes between the individual cavities of the Helmholtz resonators, which are de-tuned in a similar way to the quarter-wave resonators. However, the pressure differences and de-tuning disappears when calculated with losses.

In the case of optimization including losses, the design outcome deviates far from the classical Helmholtz resonator shape, with the cavity best described as a four-leaf clover. Usually, the neck of Helmholtz resonators is the primary source of viscothermal dissipation. In this case, however, it is believed that the clover shape contributes to increased damping, with closer boundaries. Whether the lossy design can still be considered a Helmholtz resonator is unclear, but it does include a neck and a slightly unconventionally shaped cavity. While the overall shape between the lossless and lossy design deviates, the neck shape at the entrance of the Helmholtz resonators is very similar.

The absorption coefficient as a function of frequency is plotted in Fig. 9. Interestingly, optimized designs based on a lossless assumption produce poorer designs when compared to the initial guess, indicating that numerical damping alone is not sufficient in this case. On the other hand, including viscothermal losses during optimization results in an improved design, with perfect absorption at the optimization frequency. The figure includes viscothermal FEM calculations, with conclusions similar to those in Section 5.1.

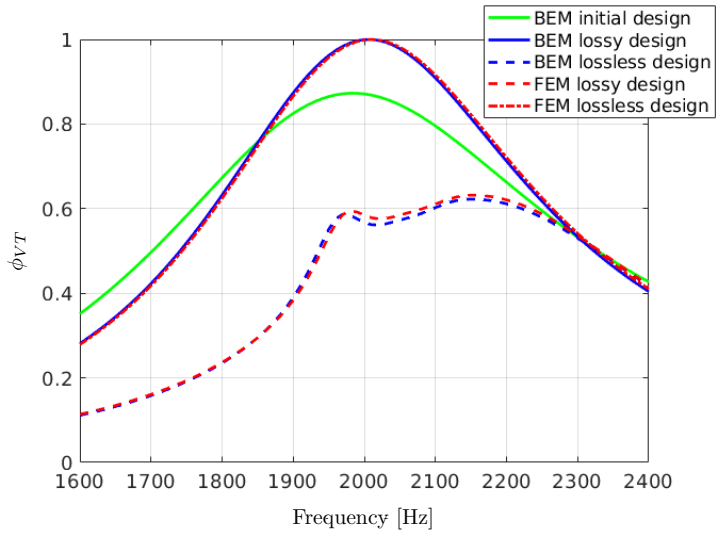

Figure 9: The absorption coefficient as a function of frequency for the Helmholtz resonators, shape optimized under lossless and lossy conditions. Both BEM and FEM simulations are calculated including viscothermal losses.

Another relevant performance criterion besides the absorption coefficient is the impedance at the termination. For a perfect absorber, with an absorption coefficient equal to 1, an impedance close to the characteristic impedance is expected. Calculations of the average impedance magnitude and phase across the terminations are given in Table 1 and compared to the characteristic impedance corresponding to the ambient conditions assumed in the simulations. While the lossy design matches the average characteristic impedance very well, it should, however, be noted that the impedance across the termination varies slightly across the cross-section. For the lossless design, it is obvious that the impedance criterion is not fulfilled. Since the aim of this paper is on viscothermal losses, we do not investigate the impedance mismatch in the lossless setting further.

	Lossless design	**Lossy design**	**Characteristic impedance**
$\lvert Z_{avg}\rvert$ $\left[\frac{\mathbf{Pa \cdot s}}{\mathbf{m}}\right]$	261.66	412.86	413.09
$\angle Z_{avg}$ $[\boldsymbol{rad}]$	0.59	-0.02	0

Table 1: The average impedance and phase near the impedance tube termination compared with the characteristic impedance.

6. Discussion

This paper presents an acoustic BEM shape optimization technique including viscous and thermal dissipation. It is successfully applied to maximize the absorption coefficient of two classical two-dimensional acoustic resonators located at an impedance tube termination. The potential problems when neglecting acoustic dissipation during optimization are investigated. In both the case of quarter-wave and Helmholtz resonator simulations, the designs yield significantly better performance if optimized upon a lossy assumption. In all lossy designs, the final resonators yield perfect absorption at the desired frequencies. On the other hand, lossless optimization has proven to develop poorly performing resonators. However, the outcome depends on the resonator type. The quarter-wave resonators, optimized on a lossless assumption, deliver an improved design over the initial starting guess. This is mainly due to the existence of numerical damping in BEM. In the case of the Helmholtz resonators, optimization without viscothermal losses creates a poorer design when compared to the initial resonator shape. Additionally, it is examined whether a simplified bulk loss description of losses can be used to improve the optimization result. It turns out to be difficult to estimate an appropriate value of the loss parameter τ_s. Moreover, none of the studied values of τ_s has resulted in perfect absorption when analysed using the viscothermal model.

The combination of viscothermal BEM and shape optimization is a promising tool and can be applied to the development of a range of acoustic applications where viscothermal losses are relevant. The current implementation is however limited to computationally light problems, due to the utilization of an

inefficient FD sensitivity estimation. Future work should therefore investigate methods for obtaining more accurate and efficient sensitivities, i.e., development and implementation of an adjoint method. This would allow for the study of three-dimensional test cases suitable for experimental validation. In general, experimental realization of optimized acoustic designs will require the inclusion of manufacturing constraints and robustness measures. The proposed technique includes constraints that might be applicable, but not necessarily sufficient for this purpose, i.e., the curvature and distance constraints. Additionally, the proposed shape optimization technique can be extended to account for mechanical coupling which often plays an important role in small micro-acoustic devices. Finally, it would be interesting to pursue alternative objectives or multi-objectives such as impedance and total energy loss.

References

[1] P. M. Morse, Theoretical Acoustics, McGraw-Hill, Princeton, 1968.

[2] A. D. Pierce, Acoustics. An introduction to its principles and applications (Ch. 10), McGraw Hill, New York, 1981.

[3] R. Kampinga, Viscothermal acoustics using finite elements analysis tools for engineers, Ph.D. thesis, University of Twente, Enschede (2010).

[4] R. Christensen, Acoustic modeling of hearing aid components, Ph.D. thesis, University of Southern Denmark (2010).

[5] D. Homentcovschi, R. N. Miles, P. Loeppert, A. J. Zuckerwar, A microacoustic analysis including viscosity and thermal conductivity to model the effect of the protective cap on the acoustic response of mems microphone, Microsyst Technol. 20 (2) (2014) 265–275. doi:10.1007/s00542-013-1800-5.

[6] R. Christensen, U. Skov, Compression driver simulation incl. vibroacoustic, viscothermal & porous acoustics, in: Proceedings from the COMSOL conference in Stuttgart (Germany), 2011.

[7] R. Christensen, U. Skov, Simulation of a 4" compression driver using a fully coupled vibroacoustic finite element analysis including viscous and thermal losses, in: Audio Engineering Society Convention 132, 2012.
URL http://www.aes.org/e-lib/browse.cfm?elib=16310

[8] M. Berggren, A. Bernland, D. Noreland, Acoustic boundary layers as boundary conditions, Journal of Computational Physics 371 (2018) 633–650. doi:10.1016/j.jcp.2018.06.005.

[9] J. Carbajo, J. Ramis, Godinho, J. Amado-Mendes, P., J. Alba, A finite element model of perforated panel absorber including viscothermal effects, Journal of Applied Acoustics 90 (2014) 1–8. doi:10.1016/j.apacoust.2014.10.013.

[10] A. I. Komkin, M. A. Mirov, A. I. Bykov, Sound absorption by a helmholtz resonator, Acoustical Physics 63 (4) (2017) 385–392. doi:10.1134/S1063771017030071.

[11] S. A. Cummer, J. Christensen, A. Alù, Controlling sound with acoustic metamaterials, Nature reviews materials 1 (2016) 1–13. doi:doi:10.1038/natrevmats.2016.1.

[12] R. E. Christensen, O. Sigmund, Exprimental validation of systematically designed acoustic hyperbolic meta material slab exibiting refraction, Appl. Phys. Lett. 109 (2016) 101905. doi:10.1063/1.4962441.

[13] V. C. Henríquez, V. García-Chocano, J. Sánchez-Dehesa, Viscothermal losses in double-negative acoustic metamaterial, Physical Review Applied 8 (12) (2017) 014029. doi:10.1103/PhysRevApplied.8.014029.

[14] V. C. Henríquez, P. Andersen, J. S. Jensen, P. M. Juhl, J. Sánchez-Dehesa, A numerical model of an acoustic metamaterial using the Boundary Element Method including viscous and thermal losses, Journal of Computational Acoustics 25 (4) (2017) 1750006. doi:10.1142/S0218396X17500060.

[15] M. Molerón, M. Serra-Garcia, C. Daraio, Visco-thermal effects in acoustic metamaterials: from total transmission to total reflection and high absorption, New J. Phys. 18 (2016) 033003. doi:10.1088/1367-2630/18/3/033003.

[16] N. Jiménez, V. Romero-García, P. Pagneux, J. Groby, Rainbow-trapping absorbers: Broadband, perfect and asymmetric sound absorption by subwavelength panels for transmission problems, Scientific Reports 7 (1) (2017) 13595. doi:10.1038/s41598-017-13706-4.

[17] R. Udawalpola, E. Wasbro, M. Berggren, Optimization of a variable mouth horn, Int. J. Numer. Meth. Engng 85 (2010) 591–606. doi:10.1002/nme.2982.

[18] E. Wadbro, M. Berggren, Topology optimization of an acoustic horn, Comput. Methods Appl. Mech. Engrg. 196 (2006) 420–436. doi:10.1016/j.cma.2006.05.005.

[19] R. Udawalpola, E. Wasbro, M. Berggren, Optimization of an acoustic horn with respect to efficientcy and directivity, Int. J. Numer. Meth. Engng 73 (2007) 1571–1606. doi:10.1002/nme.2132.

[20] R. Christensen, Topology optimization of thermoviscous acoustics in tubes and slits with hearing aid applications, Proceedings of the COMSOL Conference in Rotterdam.

[21] M. Malinen, M. Lyly, P. Raback, A. Karkainen, L. Karkkainen, A Finite Element Method for the modeling of thermo-viscous effects in acoustics, Proceedings of the 4th European Congress on Computational Methods in Applied and Engineering ECCOMAS, Jyvaskyla (Finland).

[22] M. Bruneau, P. Herzog, J. Kergomard, J. D. Polack, General formulation of the dispersion equation in bounded visco-thermal fluid, and application to some simple geometries, Wave Motion 11 (1989) 441451doi:10.1016/0165-2125(89)90018-8.

[23] V. Cutanda Henríquez, P. M. Juhl, An axisymmetric boundary element formulation of sound wave propagation in fluids including viscous and thermal losses, Journal of the Acoustical Society of America 134 (5) (2013) 3409. doi:10.1121/1.4823840.

[24] V. Cutanda Henríquez, P. Risby Andersen, A three-dimensional acoustic boundary element method formulation with viscous and thermal losses based on shape function derivatives, Journal of Computational and Theoretical Acoustics (Accepted 2018).

[25] V. Cutanda Henríquez, P. M. Juhl, OpenBEM - an open source Boundary Element Method software in acoustics,, Proceedings of the 39th International Congress on Noise Control Engineering, Inter-noise, Lisbon (Portugal).

[26] ISO 10534-2:1998, Acoustics – Determination of sound absorption coefficient and impedance in impedance tubes – Part 2: Transfer-function method, Standard, International Organization for Standardization (1998).

[27] MATLAB optimization toolbox, the MathWorks, Natick, MA, USA (2017b).

[28] Topology Optimization Theory, Methods, and Applications, author = Bendœ, M. P. and Sigmund, O., YEAR = 2004, PUBLISHER = Springer,.

[29] L. Chen, L. Liu, W. Zhao, H. Chen, 2D acoustic design sensitivity analysis based on adjoint variable method using different types of boundary elements, Acoust. Aust. 44 (2016) 343–357. doi:10.1007/s40857-016-0065-4.

[30] J. Fahnline, Numerical difficulties with boundary element solutions of interior acoustic problems, Journal of Sound and Vibration 319 (2008) 1083–1096. doi:10.1016/j.jsv.2008.06.040.

[31] S. Marburg, Numerical damping in the acoustic boundary element method, Acta Acustica United with Acustica 102 (2018) 1550016. doi:10.3813/AAA.918958.

[32] S. Marburg, A pollution effect in the boundary element mmethod for acoustic problems, Journal of Computaional Acoustics 26 (18) (2018) 1850018. doi:10.1142/S0218396X18500182.

[33] H. Ryoo, W. Jeon, Dual-frequency sound-absorbing metasurface based on viscothermal effects with frequency dependence, Journal of Applied Physics 123 (2018) 115110. doi:10.1063/1.5017540.

[34] J. Li, W. Wang, Y. Xie, B. Popa, S. A. Cummer, A sound absorbing metasurface with coupled resonators, Appl. Phys. Lett. 109 (2016) 091908. doi:10.1063/1.4961671.

[35] N. Aage, V. Egede Johansen, Topology optimization of microwave waveguide filters, International Journal for Numerical Methods in Engineering 112 (3) (2017) 283–300. doi:10.1002/nme.5551.

[36] N. Aage, Mortensen, N. A., O. Sigmund, Topology optimization of metallic devices for microwave applications, International Journal for Numerical Methods in Engineering 83 (2) (2010) 228–248. doi:10.1002/nme.2837.

[37] A. R. Diaz, O. Sigmund, A topology optimization method for design of negative permeability metamaterials, International Journal for Numerical Methods in Engineering 41 (2) (2010) 163–177. doi:10.1007/s00158-009-0416-y.

[38] COMSOL Multiphysics Reference Manual, version 5.2, COMSOL, Inc, www.comsol.com.

[39] R. E. Christensen, E. Fernandez-Grande, Experimental validation of a topology optimized acoustic cavity, J. Acoust. Soc. Am. 138 (2015) 3470–3474. doi:10.1121/1.4936905.

DTU Electrical Engineering
Department of Electrical Engineering
Technical University of Denmark

Ørsteds Pl. 352
2800 Kgs. Lyngby

www.elektro.dtu.dk